Factors Influencing the Critical Product in Electromigration

Von der Fakultät Chemie der Universität Stuttgart zur
Erlangung der Würde eines Doktors der Naturwissenschaften
(Dr.rer.nat) genehmigte Abhandlung

vorgelegt von
Alexander Straub
geboren in Wiesensteig

Hauptberichter: Prof.Dr.phil. E. Arzt
Mitberichter: Prof.Dr.rer.nat M. Rühle
Tag der mündlichen Prüfung:31.07.2000

Max-Planck-Institut für Metallforschung und
Institut für Metallkunde der Universität Stuttgart

2000

Abstract

Electromigration is the electric current-induced transport of atoms, which can cause failure in the small interconnect lines of intergrated circuits through the formation of voids and hillocks. It has been found that the formation of electromigration-induced damage is suppressed if the product of current density and interconnect length is smaller than a certain critical value. This effect has been attributed to the generation of mechanical stress gradients which balance the electromigration force until a certain "threshold stress" is reached and the material begins to deform plastically. However, an in-depth understanding of the atomic mechanisms that lead to a threshold stress for deformation has not yet been achieved.

In this work the electromigration threshold stress was compared with the flow stress of the films, as determined by wafer curvature. It was found that there are significant differences between these two stresses which are attributed to the fact that the flow stress of the film represents an average over a large number of grains while the electromigration threshold stress is associated with deformation of non-(111) grains which make up only a small fraction of the film. Further investigations have shown that hillocks grow preferentially in non-(111) grains by the addition of material at the bottom of the grain which is often accompanied by grain growth. Finally, a model is proposed for electromigration-induced hillock growth which may account for the measured threshold stress.

Zusammenfassung

Als Elektromigration bezeichnet man den durch einen elektrischen Strom induzierten Materialtransport, der durch die Bildung von Poren und Hügeln zum Ausfall von elektrischen Leiterbahnen in integrierten Schaltkreisen führen kann. Es hat sich herausgestellt, daß die Schädigung durch Elektromigration unterdrückt werden kann, wenn das Produkt aus Stromdichte und Leiterbahnlänge einen bestimmten Wert nicht überschreitet. Dieser Effekt wurde dem Aufbau eines mechanischen Spannungsgradienten zugeschrieben, der dem elektromigrationsinduzierten Materialtransport solange entgegenwirken kann, bis eine bestimmte kritischen Spannung erreicht wird, ab der sich das Material plastisch verformt.

In dieser Arbeit wurde die kritische Spannung mit der Fließspannung der Schicht verglichen, die mit Hilfe der Substratkrümmungsmethode bestimmt wurde. Hierbei hat sich gezeigt, daß es signifikante Unterschiede zwischen diesen beiden Spannungen gibt, die darauf zurückgeführt wurden, daß die Fließspannung einen Mittelwert über eine große Anzahl von Körnern repräsentiert, während die kritische Spannung mit der Deformation von nicht-(111) Körnern verknüpft ist, die nur einen geringen Bruchteil der gesamten Schicht ausmachen. Weitere Untersuchungen haben gezeigt, daß die Bildung von Hügeln bevorzugt in nicht-(111) Körnern durch den Materialeinbau in die Schicht/Substrat Grenzfläche erfolgt und gewöhnlich mit Kornwachstum verbunden ist. Schließlich wurde ein Modell für elektromigrationsinduziertes Hügelwachstum vorgeschlagen, das die Existenz einer kritischen Spannung erklären kann.

Vorwort

Diese Arbeit wurde in der Zeit von Januar 1997 bis Juni 2000 am Institut für Metallkunde der Universität Stuttgart und am Max-Planck-Institut für Metallforschung in Stuttgart angefertigt.

Zahlreiche Mitarbeiter des Instituts haben mich bei meiner Arbeit in vielfacher Hinsicht unterstützt, wofür ich mich bedanken möchte.

Insbesondere bedanke ich mich bei:

Herrn Prof. Dr. E. Arzt für die Möglichkeit unter seiner Anleitung zu promovieren, für seine Diskussionsbereitschaft, für die vielen Anregungen und für die Übernahme des Hauptberichts.

Frau Dr. C. A. Volkert für das Korrekturlesen, für die stetige Diskussionsbereitschaft, für das wissenschaftliche Interesse an meiner Arbeit und für die Messung der mechanischen Eigenschaften der zur Verfügung gestellten Schichten.

Herrn Prof. Dr. M. Rühle für die Übernahme des Mitberichts.

L. Morris für die Messungen zur Überprüfung der Konstanz des kritischen Produktes.

Meinen Eltern für die langjährige Unterstützung und Zuversicht.

Contents

Chapter 1

Introduction

The technical development in the last two decades of the 20th century is mainly characterized by the revolution in the information and communication technologies. This development was enabled by the enormous progress in microelectronics and semiconductor technology due to the miniaturization of integrated circuits (IC). Reducing the circuit dimensions reduces the transmission distances and increases the achievable speed of operation. The performance of computer chips can thereby be enhanced dramatically. A microelectronic integrated circuit contains typically more than a million components such as transistors, resistors and capacitors packed into an area the size of a thumbnail on a silicon chip and connected by small wires (simply referred to as interconnects) of less than 0.5 μm width. In the near future, this number is expected to increase to more than a billion components connected by conductor lines narrower than 0.1 μm. An SEM picture of such an interconnect structure in an intergrated circuit is shown in Fig. 1.1.

To achieve this high density of silicon devices, several levels of metal wiring are used as shown in Fig. 1.1. The different metallization levels are connected through interlevel contacts or "vias" which are generally composed of tungsten. Since the lifetime of a chip is in the worst case determined by the failure of a single device or interconnect, the reliability of each component and interconnect must be extremely high. Beside oxide reliability, stress voiding, solder reliability and others, electromigration has become a major reliability concern, especially due to the further decrease in interconnect linewidth and increase in overall length of

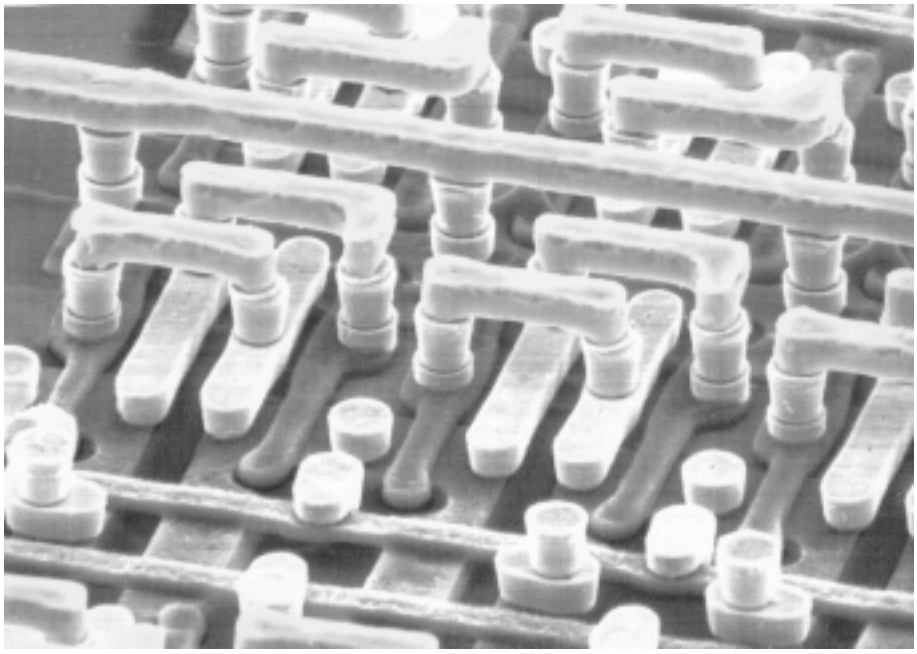

Figure 1.1: SEM picture of an interconnect structure of an SRAM (IBM).

interconnects in a device.

Electromigration is electric-current biased atomic diffusion, caused by the momentum transfer from the electrons to the atoms of a conductor. At flux divergence sites, due to changes in microstructure or material properties (e.g. between the AlCu interconnects and the tungsten vias) this mass transport can lead to open circuits in form of voids and short circuits through so-called hillocks. Because of this severe effect on the functionality of the interconnects, electromigration has been studied extensively over the last thirty years.

One of the pioneers in the electromigration field was Ilan Blech. He made the important observation that for a given current density, Al segments which fall below a critical length do not show any electromigration damage at all. Further investigations showed that the product of current density and this critical length is constant, the so called critical product (often referred to as threshold product or simply electromigration threshold). The existence and knowledge of the critical product can be quite useful for chip design rules, because for a given current density interconnects shorter than the critical length should not fail and, similarly,

interconnects of a given length should not fail below the critical current density.

Blech related the observed critical product to the existence of a mechanical stress-driven backflux which originates from the development of a stress gradient between the ends of the segment. The material transport along the segment due to electromigration leads to a compressive stress state at the anode end of the segment and a tensile or near zero stress state at the cathode end [1]. The mechanical stress gradient, which is determined by the stress difference between the segment ends divided by the segment length, causes a backflux which counteracts the electromigration flux. However, the stress-driven backflux is limited because the stress in the segment can only grow until it reaches a certain threshold stress and the material starts to deform plastically. Therefore, the stress gradient necessary to counterbalance the electromigration mass flux can only be achieved in lines that are short enough that the steady-state stress is below the threshold stress for material deformation.

Both the generation of mechanical stress gradients and backfluxes have been experimentally verified in [1]-[4], but a fundamental understanding of the mechanisms responsible for the existence of a threshold stress has not been achieved yet. It has been suggested that the threshold stress is determined by yielding of the Al [5]-[6] or by a diffusional creep threshold [7]. Further suggestions such as a threshold stress for void nucleation or cracking of the native oxide have also been proposed.

The goal of this work is to improve the current understanding of the threshold stress and identify the underlying physical mechanisms. Therefore, investigations of the damage formation process such as hillock growth and the influence of film thickness, temperature and annealing treatment on the critical product are performed and conclusions concerning the mechanism responsible for the threshold stress are drawn.

[1]Throughout the thesis the following convention is used: The cathode end is where the electrons enter the segment and the anode end where they leave the segment

Chapter 2

State of the Literature

In this chapter a brief introduction to electromigration will be given and the most important parameters influencing the critical product (and therefore the threshold stress) will be reported. Subsequently, the various proposals for the origin of the threshold stress will be summarized and critically discussed.

2.1 Electromigration Fundamentals

2.1.1 The Electromigration Flux

Electromigration is a mass transport process which can be observed in metal conductors at high current densities. This mass transport is caused by the sum of two diametrical forces acting on a metal atom: The force due to the Coulomb interaction of the positive metal ions with the electric field in the conductor and the so-called wind force which results from the momentum transfer between the electrons and the metal ions. Depending on which of the forces is stronger, the atoms move towards the cathode or anode end of the conductor. In the case of Al the wind force is stronger than the Coulomb force and the atoms move to the anode end of the conductor. The resulting force F_{EM} due to electromigration is conventionally expressed as the product of the electric field E and the effective charge Z^*e [8],

$$F = EZ^*e \ , \tag{2.1}$$

where Z^* is the effective valence number of the metal atom [1] and e the fundamental charge.

The atomic flux J_{EM} due to the electromigration driving force F_{EM} can be written as [8],

$$J_{EM} = NmF_{EM} \ , \tag{2.2}$$

where m is the mobility of the atoms and N the atomic concentration. The mobility m of the atoms is given by the Einstein equation

$$m = D/kT \ , \tag{2.3}$$

where D is the diffusivity, k Boltzmann‘s constant and T the absolute temperature. Therefore, the atomic flux due to electromigration can be expressed as

$$J_{EM} = N\frac{D}{kT}Z^*e \ E = N\frac{D}{kT}Z^* \ e \ \rho \ j \ , \tag{2.4}$$

where j is the current density and ρ the resistivity of the metal.

D in equation 2.4 represents an effective diffusivity along the interconnect because the electromigration mass transport can occur by different diffusion mechanisms such as lattice diffusion, interface diffusion (Al/TiN, Al/Al_2O_3), pipe diffusion and grain boundary diffusion. However, for polycrystalline Al segments at moderate temperatures (e.g. 225 °C) the dominant diffusion path is generally accepted to be along grain boundaries [11].

2.1.2 The Generation of Mechanical Stresses

Electromigration behavior can be investigated using edge displacement experiments which were first introduced by Blech [5], [12], [13], [1]. A schematic illustration of a typical test sample (usually referred to as a Blech structure) for this experiment is shown in Fig. 2.1. Short Al segments of different lengths are deposited on a continuous line of a higher resistivity diffusion barrier material such as TiN. In the regions where Al is present the electrical current passes mainly through the Al because of its much lower resistivity, whereas between the segments the current has to pass through the TiN. The advantage of this type of

[1] Experimentally determined values of Z* for Al range from -1 to -30 [9], [10].

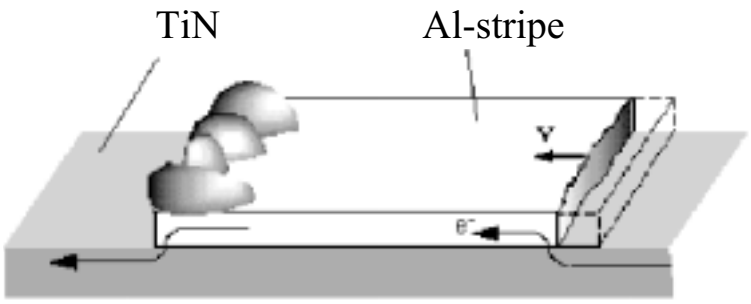

Figure 2.1: Schematic illustration of a typical test sample (Blech structure) used for edge displacement experiments.

test sample is that there are perfect flux divergences at both ends of the segments and the electromigration mass transport can be directly observed as depletion of material at the cathode end and accumulation or hillock formation at the anode end. The amount of edge displacement can be measured as a function of time and the corresponding drift velocity can be calculated. Fig. 2.2 shows the drift velocity as a function of current density for a 115 μm long Al segment on TiN as measured by Blech [12]. A linear dependence of the drift velocity on the current density is observed, but the line does not pass through the origin. Instead, a certain threshold current density is required before any edge displacement takes place. This threshold current density j_{th} depends on the length of the Al segment in such a way that the product of the threshold current density and segment length is a constant [1]- the critical product-. Therefore, the critical current density for drift is also related to the existence of the stress-driven backflux and the critical product for damage formation [13], [6].

When current flows through the Al segment, atoms are depleted from the cathode and accumulated at the anode. If the sample is constrained, say by the underlying substrate or the native oxide, this leads to the generation of mechanical stresses in the Al. The details of the generation of stress in an unpassivated polycrystalline Al segment with columnar grains can be described by the following picture: First, it is assumed that the vacancies are maintained in equilibrium along the grain boundaries since most of the grain boundaries are efficient sources

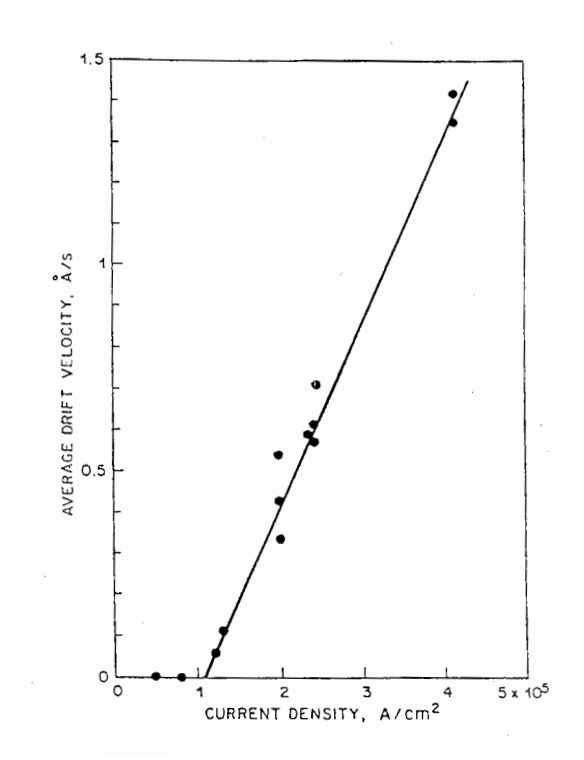

Figure 2.2: Average drift velocity of an 25 μm wide, 460nm thick, and 115 μm long Al segment on 260nm TiN (heat treated 500 °C, 1/2 h) as a function of current density as measured by edge displacement technique [12].

and sinks for vacancies even at chemical potential as small as 10^{-4}eV [14]. This means a stress of only $\sigma = 10^{-4}\text{eV}/\Omega \approx 1\text{MPa}$ ($\Omega = 1.66 \cdot 10^{-29}\text{m}^3$ is the atomic volume of Al) is necessary to maintain vacancies in equilibrium. Therefore, when atoms accumulate at the anode, there is an increase in the number of lattice sites, and if the sample is constrained this leads to the generation of compressive stresses. (The stress in turn changes the equilibrium concentration of vacancies, but this change is small in comparison with the number of vacancies that are created or annihilated in generating the stress, and can be neglected to first order.) If it is also assumed that grain boundaries can not sustain shear stresses then the increase in number of lattice sites must lead to compressive stresses normal to the grain boundaries, which lie in the plane of the film for a film with columnar grains. In a similar way, depletion of atoms leads to tensile grain boundary normal stresses at the cathode end of the segment. As a result a stress gradient is

developed along the segment which leads to a mechanical stress-driven backflux J_σ according to the following equation

$$J_\sigma = N\frac{D}{kT}\frac{\partial}{\partial x}(\mu_a - \mu_v) \ , \tag{2.5}$$

where μ_a and μ_v are the chemical potentials of the atoms and vacancies, and x is the coordinate along the segment in the direction of electron flow [2]. In the case of thermal equilibrium of the vacancies μ_v is equal to zero and the chemical potential function is given by [15]

$$\mu = \mu_a - \mu_v = \mu_0 - \Omega\sigma_n \ , \tag{2.6}$$

where Ω is the atomic volume, μ_0 the chemical potential of an atom in a stress free crystal, and σ_n the normal stress to the grain boundary. The stress-driven backflux J_σ can then be written as

$$J_\sigma = N\frac{D\Omega}{kT}\frac{\partial\sigma_n}{\partial x} \ . \tag{2.7}$$

2.1.3 The Critical Product of Current Density and Segment Length

Below the threshold current density, where no drift occurs, the electromigration flux J_{EM} is equal to the stress-driven backflux J_σ:

$$J_{EM} = J_\sigma \tag{2.8}$$

Substituting equations 2.4 and 2.7 in equation 2.8 yields

$$eZ^*\rho j = \Omega\frac{\partial\sigma_n}{\partial x} \ , \tag{2.9}$$

which can be rewritten as

$$(j \cdot l)_{crit} = \frac{\Omega\Delta\sigma_{th}}{eZ^*\rho}, \tag{2.10}$$

using $\partial\sigma_n/\partial x = \Delta\sigma_{th}/\Delta x$, where Δx is equal to the segment length l and $\Delta\sigma_{th}$ is the maximum difference between the grain boundary normal stresses at the

[2] Throughout the thesis the x-coordinate is always along the segment, the y-component perpendicular to the segment in the plane of the film and the z-coordinate perpendicular to the plane of the film.

anode and the cathode end of the segment that the material can sustain at a given temperature. This expression is generally known as the critical product of electromigration and was first derived by Ainslie [16] and Blech [12]. Experimentally determined values for the critical product in pure Al (polycrystalline unpassivated lines) at 225 °C range from 500 [17] to 2000 A/cm [12].

For a film with a grain size on the order of the film thickness the electromigration-induced material deposition at the grain boundaries leads to a stress distribution which is similar to biaxial over any cross section of the segment. This is because the grain boundary stresses are to a very good approximation in thermal equilibrium during electromigration in any particular cross section of the segment [3]. The chemical potential in any cross section of the segment is therefore constant at all grain boundaries, independent of their orientation, and the atoms are deposited at the differently orientated grain boundaries such that the normal stresses across the boundaries become equal.

[3] a typical diffusion distance l is on the order of the grain size, e.g. $l = 1\mu$m, and the time to reach local stress equilibrium can be estimated by the relation $t \approx l^2/D$ to be roughly $(10^{-6}m)^2/10^{-12}m^2s^{-1} \approx 1s$.

2.2 Factors Influencing the Critical Product

The influence of several parameters such as testing temperature, choice of diffusion barrier, the ratio of grain size to line width and anodic oxide thickness on the critical product of unpassivated pure Al segments has been investigated in the literature and is reported here.

Fig. 2.3 shows a summary of reported values for the critical product in polycrystalline pure Al segments as a function of temperature. There is a lot of scatter in the data which is generally attributed to variation in microstructure between samples made in different labs. Most of the data show a weak or no temperature dependence of the critical product. In contrast the data from Blech shows a fairly strong decrease in critical product with increasing temperature.

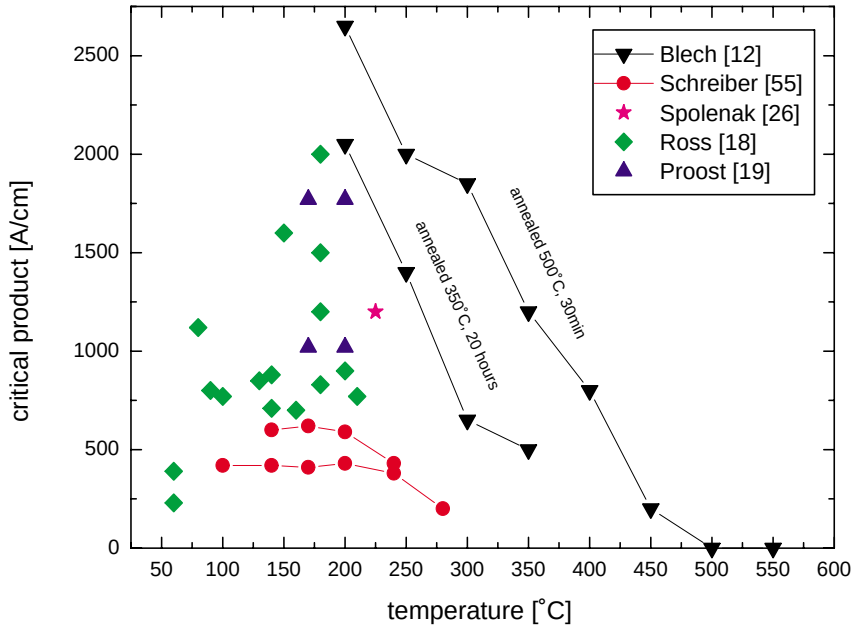

Figure 2.3: Critical products for different testing temperatures, as reported in the literature.

The influence of the ratio of the line width to grain size on the critical product

has not been systematically investigated, although narrow bamboo lines of 0.5 μm width show much higher critical products (up to 4500 A/cm as measured by Witt [20]) than wide polycrystalline lines. The near-bamboo regime is difficult to investigate because there are not only flux divergences at the cathode and anode ends of the segment but also in between due to changes in microstructure along the length of the segment. Polycrystalline clusters are often interrupted by single grains, which lead to additional flux divergences and complicate precise determination of the critical product.

The influence of anodic oxide thickness on the critical product has been investigated by Ross [21]. The results for the critical product as a function of anodic oxide thickness are shown in Fig. 2.4 where it is seen that the critical product increases only slightly (roughly 20 percent) as the oxide thickness increases from a few nm to 144 nm.

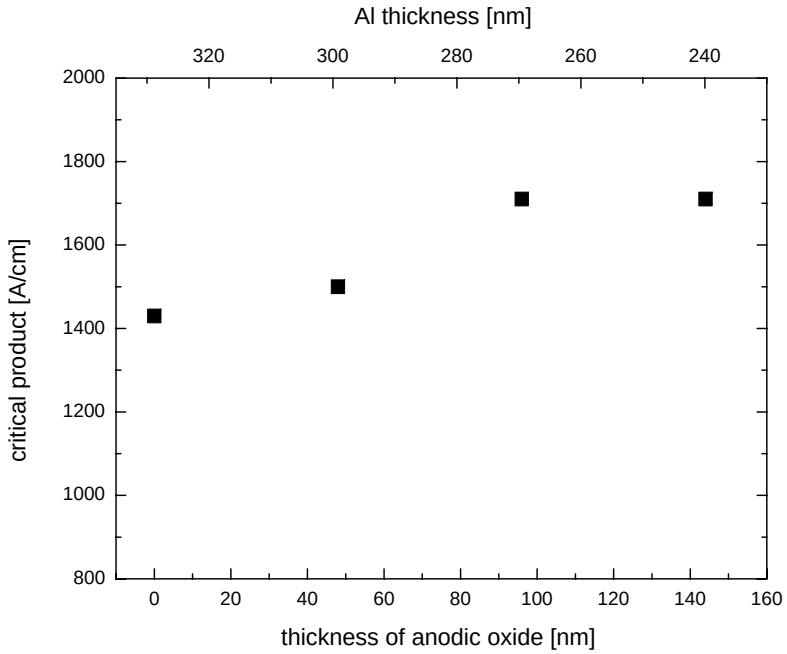

Figure 2.4: Critical product as a function of anodic oxide thickness measured for an initially 0.33 μm thick pure Al sample at a current density of roughly 1MA/cm^2 and testing temperature of 190 °C [21].

The influence of the diffusion barrier interface, which is usually an Al/TiN interface, and particularly of the Al_3Ti intermetallic compound which can form at this interface (depending on annealing history and deposition technique of the TiN) on the formation of voids has been investigated by several authors [22], [23]. These studies have shown that void formation is inhibited by the presence of Al_3Ti precipitates at the Al/TiN interface. This, presumably means that Al_3Ti raises the nucleation stress for void formation at the cathode end of the segment and therefore also the threshold stress for electromigration

2.3 Possible Origins for the Threshold Stress

There are a number of mechanisms that have been proposed in the literature to explain the existence of the electromigration threshold stress which include yielding of the Al by dislocation glide, diffusional creep, void nucleation and cracking of the native oxide. The details of how each mechanism leads to a threshold stress are summarized below and the predictions are compared with the dependencies discussed in the last section.

2.3.1 Dislocation Glide

The mechanism which is most often proposed as being responsible for the electromigration threshold stress is plastic deformation by dislocation glide, [12],[24],[6]. In this picture, the electromigration-induced stresses grow until they reach the threshold stress, which is assumed to be the yield stress of the material. This idea is supported by X-ray topography measurements [1] that show that the stress component σ_{xx} along the segment is around 120 MPa compressive at the anode end, which is close to the compressive yield stress of thin Al films [4]. Above the yield stress deformation is assumed to occur by dislocation glide and a hillock might be formed when dislocations are emitted from the grain boundary and glide to the top of the film resulting in a decrease of the stress and an increase in the height of the grain [25].

The yield stress in Al films is qualitatively consistent with the behavior of the critical product presented in the last section. For instance, from wafer curvature measurements the yield stress is known to decrease slightly with increasing temperature in agreement with the weak temperature dependence of the critical product. Also, the yield stress increases strongly with decreasing sample size which may explain the dramatic increase in critical product in bamboo lines in comparison with the wider polycrystalline lines.

[4] It should be noted that X-ray topography measures the average stress in the grains which may be slightly different than the grain boundary normal stress.

2.3.2 Diffusional Creep

A further possible mechanism which might lead to an electromigration threshold stress is diffusional creep [7], [26]. According to this picture, the electromigration threshold stress is the same as the diffusional creep threshold stress, which is a stress required to make grain boundary dislocations act as sources or sinks for vacancies. A threshold stress

$$\sigma_{th.} \approx \frac{Gb}{d} , \tag{2.11}$$

is necessary to overcome the line tension of the dislocations which act as sources and sinks for vacancies [27], [28]. G is the shear modulus, b the dislocation Burgers vector and d the grain size. For $d = 8 * 10^{-8}$m, $G = 12$ GPa and $b = 2.9 * 10^{-10}$m this leads to a threshold stress of roughly 80MPa, which is close to the threshold stress of 120 MPa measured by Blech.

Regarding equation 2.11, the temperature dependence of the critical product and threshold stress should essentially follow the temperature dependence of the shear modulus

$$\frac{d}{dT}(j \cdot l)_{crit} = \frac{\Omega}{eZ^*\rho} \frac{d\sigma_{th.}}{dT} = \frac{\Omega b}{eZ^*\rho d} \frac{dG}{dT}. \tag{2.12}$$

The temperature dependence of the shear modulus is given by [29]

$$dG/dT = 0.5\ G_0/T_m , \tag{2.13}$$

where G_0 is the shear modulus at 27 °C ($2.54 \cdot 10^4$MN/m^2) and T_m the melting temperature (660 °C) of Al. Substituting in equation 2.12 yields

$$\frac{d}{dT}(j \cdot l)_{crit} = \frac{\Omega b G_0}{2eZ^*\rho d T_m} \tag{2.14}$$

Using the following values, $\Omega = 1.66 \cdot 10^{-29}$m^3, $b = 2.9 \cdot 10^{-10}$m, $G_0 = 2.54 \cdot 10^{10}$N/m^2, $\rho = 28 \cdot 10^{-9}\Omega$ m, $e = 1,6 \cdot 10^{-19}$C, Z$^* = -6$, $d = 4 \cdot 10^{-7}$m, $T_m = 660$°C leads to a calculated slope of

$$\frac{d}{dT}(j \cdot l)_{crit.} = -2.2 \frac{\mathrm{A}}{\mathrm{cm\ °C}}, \tag{2.15}$$

which is in reasonable agreement with the widely scattered data shown in Fig. 2.3).

The critical product for narrow bamboo lines is expected to be higher than for polycrystalline wide lines, since the diffusional creep threshold stress is expected to be proportional to the inverse feature size.

2.3.3 Void Nucleation

Void formation is also a mechanism which might control the electromigration threshold stress. Homogeneous void nucleation, however, is a difficult and unlikely mechanism, because hydrostatic tensile stresses on the order of 5 GPa are necessary to cause void nucleation to occur at a significant rate, as estimated by Nix and Arzt [30]. Heterogeneous void nucleation at a flaw at the Al/TiN or Al/Al_2O_3 interface requires much smaller stresses and can be considered as an alternative nucleation mechanism. According to classical nucleation theory the free energy change upon creation of a void is given by [31]

$$\Delta F = -\sigma V + \gamma_{Al} A_{Al} + (\gamma_{TiN} - \gamma_{Al/TiN}) A_{TiN} - \gamma_{gb} A_{gb} , \qquad (2.16)$$

where the void was assumed to be created at a grain boundary intersection with the Al/TiN interface. γ refers to the interfacial free energy and A to the area of the interface, σ is the hydrostatic stress and V the volume of the void. The barrier for void nucleation is given by the maximum value of ΔF.

If this barrier to void nucleation is associated with the electromigration threshold stress, then the temperature dependence of the critical product should only be influenced by the temperature dependence of the interfacial free energy, which is known to be quite weak. For narrow bamboo lines the critical product is expected to be higher because there is usually no grain boundary at the very cathode end of the Al segment and therefore an additional energy of $-\gamma_{gb} A_{gb}$ is required to nucleate a void. The morphology of the Al/TiN interface is expected to show a strong influence on the critical product, since the interfacial free energy can change strongly with $TiAl_3$ phase formation. Summarizing, the electromigration threshold stress could also be due to the stress required to nucleate voids at the cathode end of the segment.

2.3.4 Cracking of the Native Oxide

The native oxide might control the electromigration threshold stress in two fundamentally different ways: First, it can act as a mechanical constraint for the Al line as for instance a passivation layer. In this case the threshold stress is determined by cracking of the native oxide (critical stress intensity factor). Sec-

ond, it strongly reduces the vacancy sink and source efficiency of the surface [32], [33]. In this case the threshold stress is determined by the stress necessary to activate the Al/Al_2O_3 interface as a source and sink for atoms. The threshold stresses for these two mechanisms are independent of each other and can and have considerably different values.

The idea that the electromigration threshold stress is due to a critical stress for cracking of the native oxide is consistent with the temperature dependence presented in the previous section since the fracture toughness of Al_2O_3 is almost independent of temperature in the investigated temperature range (200-350°C) [34]. However, whether the ratio of line width to grain size influences the threshold stress depends on exactly where and how the oxide fractures.

2.3.5 Summary

Several mechanisms have been reviewed which may be responsible for the electromigration threshold stress and which at least qualitatively are consistent with the experimental observations of the critical product. However, exactly which mechanism or mechanisms determine the threshold stress is not known. Therefore, the goal of this thesis is to compare these possible mechanisms with systematic measurements of the critical product in the hope of clarifying which mechanisms are dominant.

The thesis is organized in four remaining chapters. Chapter 3 describes the fabrication process of the test samples and the main experimental procedures used for the characterization and investigation of the samples. In Chapter 4 the experimental results are presented including a detailed characterization of the samples, investigations of hillock morphology and the influence of film thickness, temperature, and annealing treatment on the critical product. In Chapter 5 the electromigration threshold stress $\Delta\sigma_{th}$ is compared to the difference of flow stress $\Delta\sigma_f$ in tension and compression and possible reasons for the disagreement are discussed. Then, based on the observations of hillock morphology, a model for hillock formation is proposed which can explain the preferred growth in non-(111) grains and the difference between $\Delta\sigma_{th}$ and $\Delta\sigma_f$. Finally, possible threshold stresses associated with the proposed mechanism are shortly considered. Chapter 6 summarizes the presented research.

Chapter 3

Experimental procedure

In this chapter, the sample fabrication process and the experimental methods are briefly described. The fabrication of appropriate electromigration test samples involved a combination of e-beam lithography and reactive ion etching (RIE) and required extensive process development which is described in detail in the Appendix. The optimized process sequence used in actually making the samples is summarized here.

3.1 Sample Fabrication Process

The electromigration test samples (so-called Blech structures) consisted of 5 or 10 μm wide Al segments of different lengths on a continuous 5 or 10 μm wide TiN/Ti runner (Fig. 3.1) connecting two $150 \times 150 \mu$m contact pads. In order to fit as long a runner as possible in the limited writing field of the SEM ($400 \times 400 \mu$m) while still having sufficiently large contact pads the runner was divided in two arms by a right angle bend as shown in Fig. 3.2. The length of the Al segments ranged from 6 to 32 μm, in steps of two μm, and the spaces between the Al segments were 3 μm long. The samples were patterned from 100, 200, 400, 600, and 800nm thick pure Al films on 200nm TiN on 45nm Ti on 200nm SiO_2 on a (100) Si substrate. This is a typical film stack used in fabricating interconnects in microelectronic devices. All films were deposited by magnetron sputtering at approximately 225 °C at Bell Labs, Murray Hill, NJ. Fabricating the samples involved two e-beam lithography and two RIE processes as shown in Fig. 3.3: First, the Al

films were coated with 1 μm of negative e-beam resist (Ar 7700/5 from Allresist GmbH) using a spin coater at 4000 rpm for 30s and subsequently annealed on a hotplate at 90 °C for 2 minutes (Fig. 3.3 (a)). The e-beam lithography was carried out in a CamScan S 44 scanning electron microscope (SEM) adapted for lithography with a beam blanker and the appropriate software (Proxy-Writer from Raith). The exposure of the resist was done using the following parameters: accelerating voltage 40keV, spot size 5 (which corresponds to an e-beam diameter of roughly 50 to 100nm), probe current 100-140pA, aperture 100 μm, step size 25nm, dwell time 4μs. After e-beam writing, the resist was annealed at 110 °C for two minutes on a hot plate (Post-Exposure Bake) to induce cross-linking between the molecules in the exposed areas of the resist. The development of the resist (removal of the resist that is not cross-linked) was done in a mixture of Ar-300/26 (developer from Allresist) and deionised water (ratio 3:1) (Fig. 3.3 (b)). After development, a further annealing step was carried out at 130 °C on a hot plate for ten minutes. This annealing treatment increases the number of cross-links between the molecules and therefore the resistance of the remaining photoresist to etching. In the next step, continuous Al/TiN/Ti runners were etched from the films with $SiCl_4$ using a Plasmalab 80 Plus RIE from Oxford Instruments and the following etch parameters: base pressure 10^{-5}mbar, working pressure 40mTorr ($\approx$ 5.3 Pa), power 150 Watt, flow rate 20sccm $SiCl_4$. Using these parameters the etch rates for the different materials were approximately: 100nm Al/min, 20nm TiN/min, 10nm SiO_2/min, 30nm resist (Ar 7700/5)/min. The etching times for the different thickness Al films were calculated from the above rates, adding an additional minute to ensure removal of the metal. After etching, the sample was first rinsed in deionised water to remove any remaining Cl which might cause corrosion of the Al, and then rinsed in a mixture of Colamin, Hydroxylamin and Dihydroxybenzol (ACT 935 from Ashland-ACT) at 75 °C for 1-2 minutes to remove any residual resist (Fig. 3.3 (c)). At this point, the test samples consisted of continuous Al/TiN/Ti runners connecting the two $150 \times 150\mu$m contact pads.

To obtain Al segments of different lengths on the continuous TiN/Ti runner, spaces were etched in the Al using additional lithography and etching (process 2 in Fig. 3.3). The test samples were coated with a positive deep UV resist, which is also sensitive to e-beam exposure (Shipley UVIIHS 0.9), at 2000 rpm for 30s and subsequently soft-baked at 120 °C for 60s (Fig. 3.3 (e)). The e-

beam lithography was done in the same way as before except that the SEM was used in the backscattered electron mode in order to see the test samples below the resist. This was necessary because the lithography software does not contain alignment tools and the features used to define the spaces between Al segments must be correctly positioned on the continuous AL/TiN/Ti runner. It is important that the positioning of these features is carried out using as little total beam current as possible, since resist is exposed during imaging. The following exposure parameters were used for this lithography step : accelerating voltage 40keV, spot size 5, step size 25nm, probe current 50pA, aperture 100 μm, dwell time 10 μs. After e-beam writing, the samples were baked at 130 °C for 90 s (to cut the bonds of the polymers in the exposed areas), developed and subsequently baked at 140 °C for 3 minutes to increase the etch resistance of the residual resist (Fig. 3.3 (f)). The spaces in the Al segment were etched by RIE using the same etching parameters as in the first process. The etch time was chosen according to the Al film thickness (an approximate etch rate of 100nm Al/min, plus 1 min over-etch) (Fig. 3.3 (g)). After etching the spaces, the samples were rinsed in deionised water and the residual resist was removed by ACT in the same way as in the first process (Fig. 3.3 (h)).

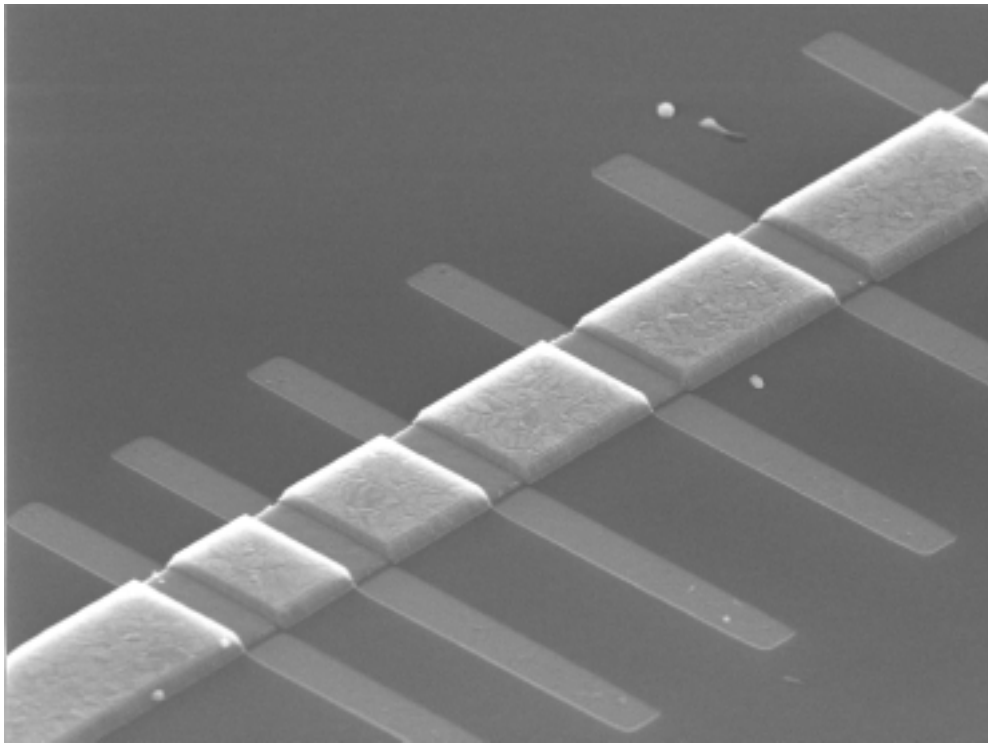

Figure 3.1: SEM picture of Al segments on a continuous TiN/Ti runner (10 μm wide) connecting the contact pads of a test sample as shown below.

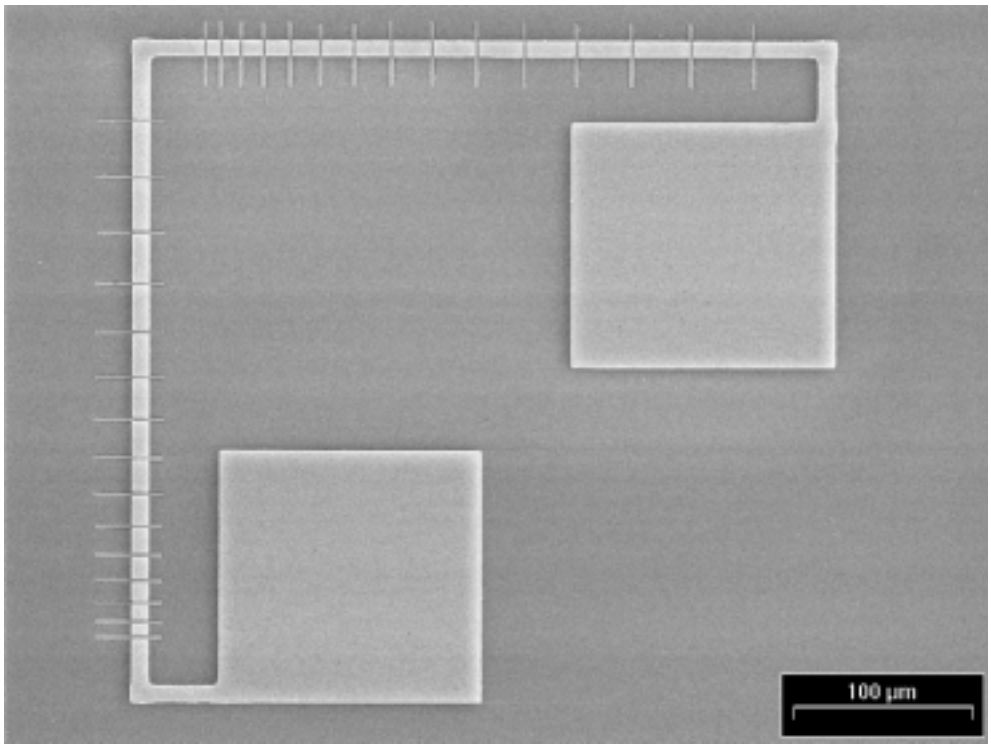

Figure 3.2: SEM picture of an electromigration test sample.

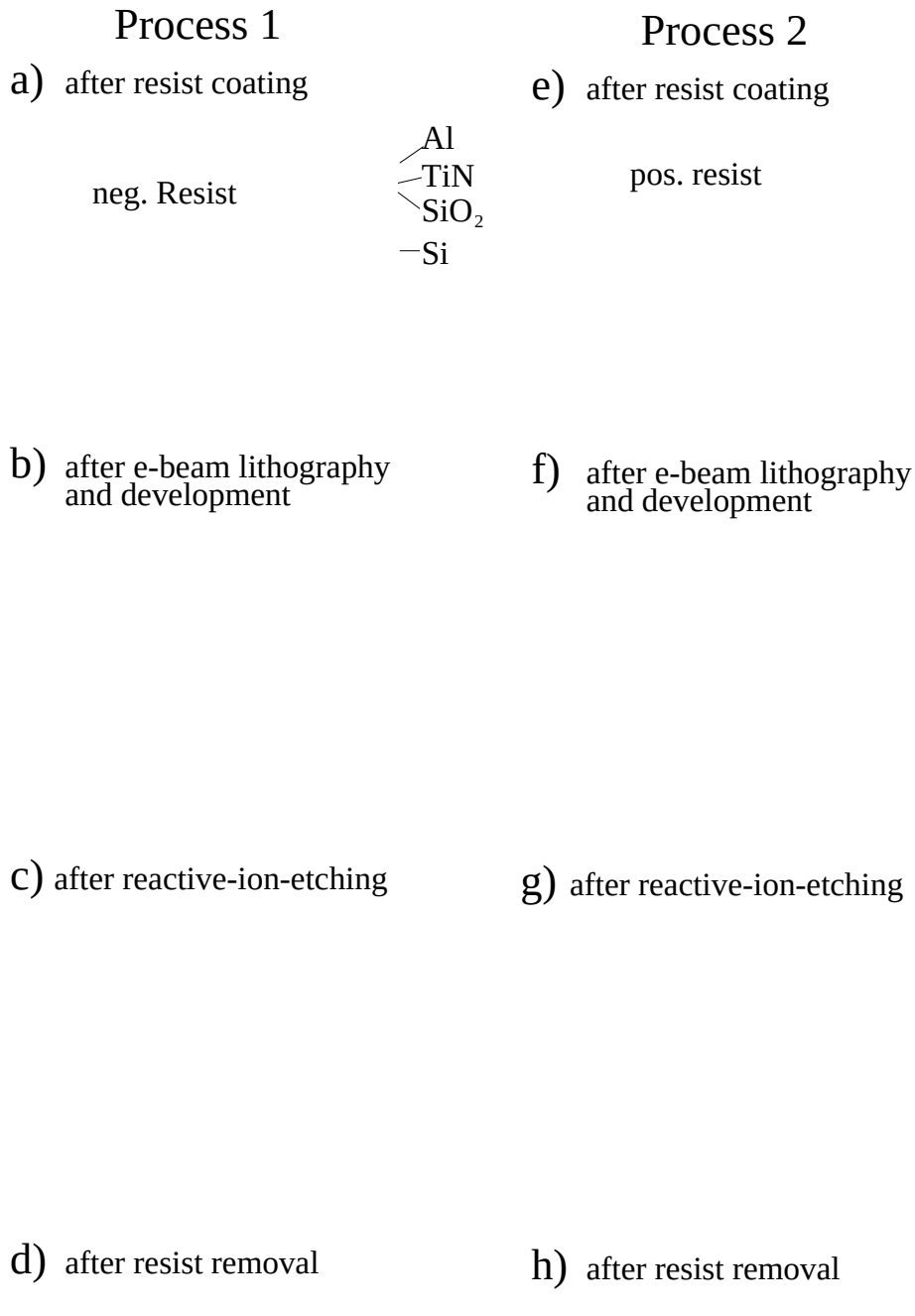

Figure 3.3: Schematic illustration of the sample fabrication process.

3.2 Electromigration Testing Procedure

All samples were tested at constant current and constant temperature. The electromigration measurements were performed in either an ex-situ (Fig. 3.4) or an in-situ probe station (Fig. 3.5) depending on availability. It was verified that both probe stations lead to the same value for the critical product for the same test sample within the observed experimental scatter. The ex-situ probe station consists of a hot plate, probe needles to contact the sample, an optical microscope to position the probe needles on the contact pads of the test sample, and a constant current source. The in-situ probe station is similar, but can be

Figure 3.4: Picture of the ex-situ electromigration probe station.

mounted in a SEM (Camscan 44) where the electron beam is used to image the sample and, with the help of motorized controls, position the needles on the sample contact pads. In addition, the SEM has software (Analysis from SIS) which allows automatic data acquisition so that pictures of the sample can be taken at regular intervals, which is especially useful for electromigration drift measurements.

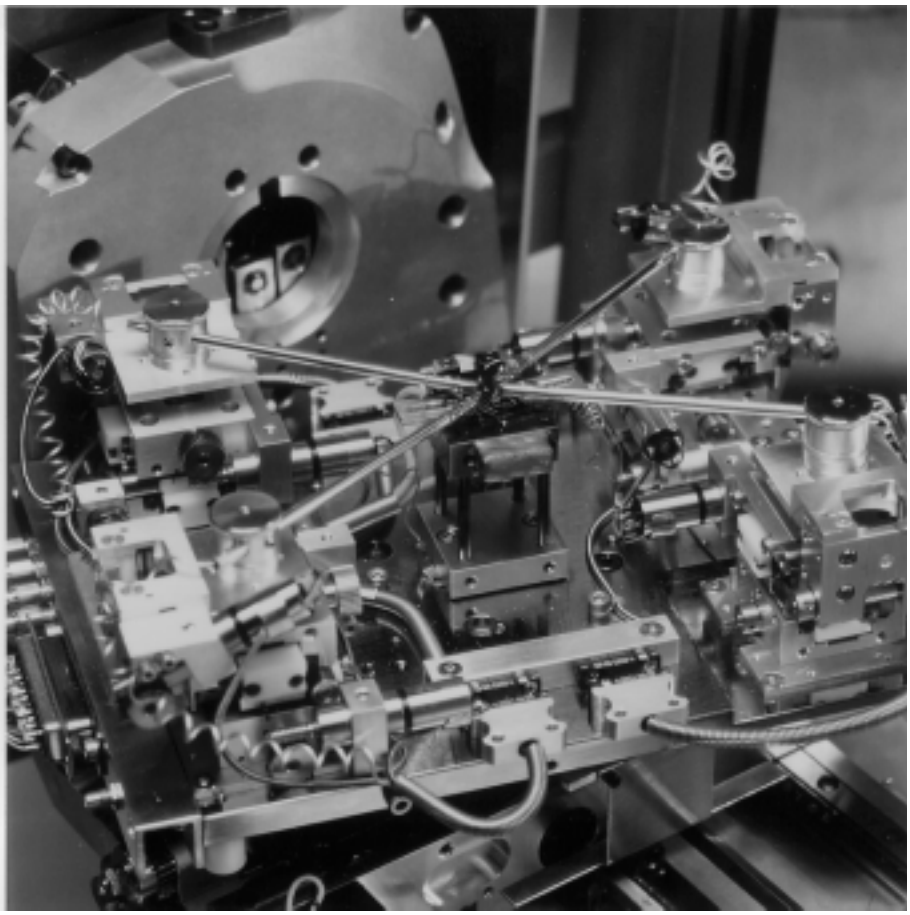

Figure 3.5: Picture of the in-situ electromigration probe station.

3.3 Joule Heating Measurement

During electromigration testing, the actual temperature of the test samples may be higher than the temperature of the hot plate due to Joule heating. It is difficult to measure the temperature of the test sample directly, but it can be determined indirectly by resistance increase measurements, since the resistivity depends on temperature.

The resistance was determined by a four point measurement as illustrated in Fig. 3.6. Two of the four needles were used to apply a constant current

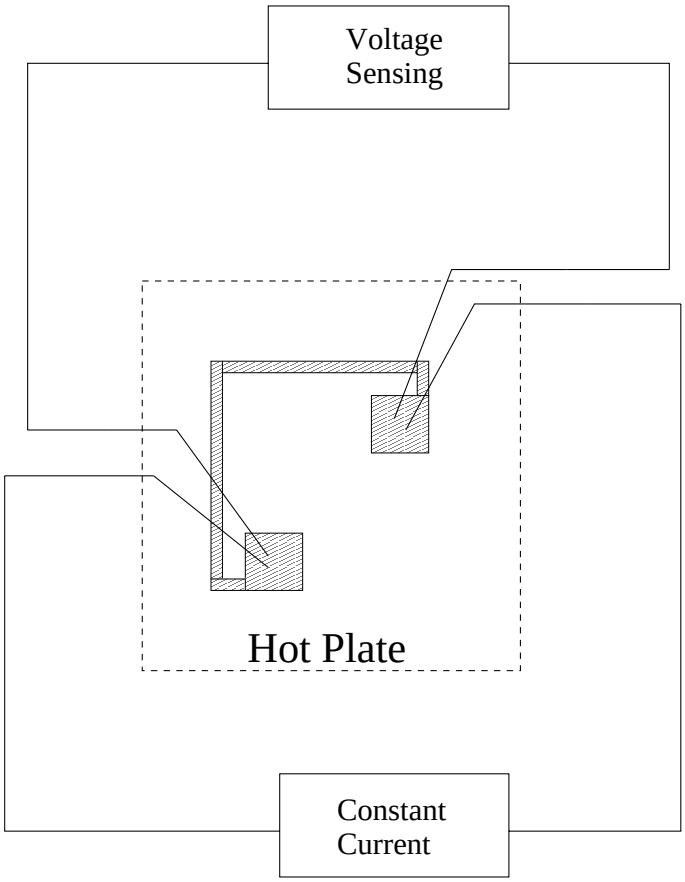

Figure 3.6: Schematic illustration of the four point resistance measurement. The current is applied by two needles and the voltage drop is measured by the two other needles.

and the other needles were used to measure the voltage drop. This method minimizes contributions from the contact resistance of the needles. To eliminate

thermoelectric contributions from the needle to contact pad junctions, the voltage drop was measured for both current directions and the average value was taken.

3.4 Electromigration Testing Under External Stress

To investigate the influence of external mechanical stress on the critical product, a four point bending apparatus was constructed as illustrated in Figs. 3.7 and 3.8 . A similar apparatus was also used by Kahn and Thompson [35] to investigate the effect of external stress on electromigration lifetime. A beam of silicon (1 cm wide, 10 cm long and 500 μm thick) with electromigration test samples was mounted in either the tensile (Fig. 3.7) or compressive (Fig. 3.8) four point bending apparatus and loaded using 50 and 100g weights. The distance between the inner contact points was four centimeters and between the outer contact points eight centimeters. The maximum stress that could be applied to the test samples was limited by the fracture of the silicon piece and determined to be approximately $\pm$ 50 MPa. Thermal contact between the silicon and the hot plate was made by a droplet of liquid gallium, which applied negligible mechanical resistance to the bending of the silicon.

In order to apply a current, the sample and bending apparatus were placed in the ex-situ probe station and the optical microscope was used to position the probe needles on the contact pads of the electromigration test samples. All tests were performed at 225 °C at a current density of 1MA/cm^2 on samples with 5 μm wide and 500nm thick Al segments.

In symmetric four point bending, the bending moment between the inner contact points is constant and given by

$$M = \frac{W}{2}a, \tag{3.1}$$

where W is the weight and a is the distance between the inner and outer contact points which was 2 cm for the apparatus used here. This bending moment causes a bending stress according to [36]

$$\sigma = \frac{My}{I}, \tag{3.2}$$

where I the moment of inertia and y is the distance from the wafer surface to the neutral plane. For a homogeneous rectangular cross section of width b and thickness h_s, the moment of inertia I is given by ${bh_s}^3/12$ and the distance y is equal to $h_s/2$. The uniaxial bending stress at the surface of the Si beam is then given by

$$\sigma = \frac{3Wa}{b{h_s}^2} \ , \tag{3.3}$$

leading to strains in the Si of σ/E_{Si} along the stress direction and $-\nu_{Si}\sigma/E_{Si}$ perpendicular to the stress direction. For the particular orientation of the Si beam in the experiments, E_{Si} is the Youngs modulus for the (011) direction and ν_{Si} is the Poisson ratio for strain induced in the $(0\bar{1}1)$ direction due to a strain applied in the (011) direction.

The in-plane strains in the Al test samples are to very good approximation the same as the in-plane strains at the surface of the Si beam because the samples adhere to the substrate and are much thinner than they are wide. Assuming isotropic material properties for Al, the stress in the Al test samples are

$$\sigma_{\parallel} = \frac{E_{Al}}{E_{Si(011)}} \ \frac{1-\nu_{Al}\nu_{Si}}{1-{\nu_{Al}}^2}\sigma \tag{3.4}$$

along the Si beam, and

$$\sigma_{\perp} = \frac{E_{Al}}{E_{Si(011)}} \ \frac{\nu_{Al}-\nu_{Si}}{1-{\nu_{Al}}^2}\sigma \tag{3.5}$$

perpendicular to the direction of the Si beam. The ratio of the parallel and perpendicular stress component is then given by

$$\frac{\sigma_{\parallel}}{\sigma\perp} = \frac{1-\nu_{Al}\nu_{Si}}{\nu_{Al}-\nu_{Si}} = 3.34 \tag{3.6}$$

using $\nu_{Si} = 0.07$ and $\nu_{Al} = 0.36$ [37]. Therefore, the applied stress is almost uniaxial.

To check the equation for the stress along the Si beam, the curvature of a Si beam was measured, as described below, for different applied weights and the calculated stresses where within 5 percent of the stresses predicted by equation 3.4.

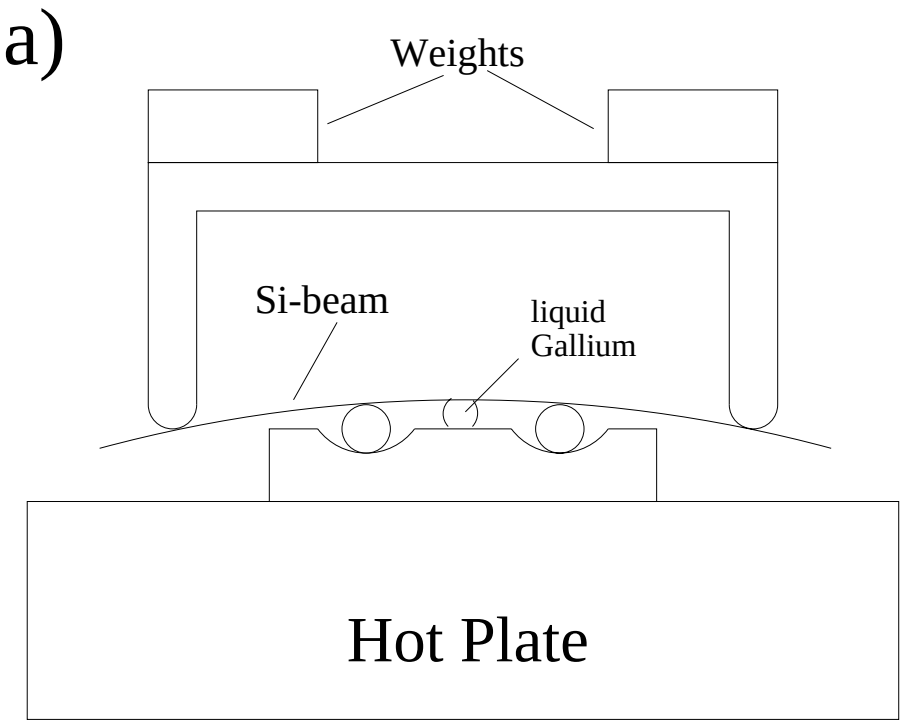

b)

Figure 3.7: (a) Schematical presentation of the four point bending apparatus for applying tensile stress. (b) Four point bending apparatus used in the experiment.

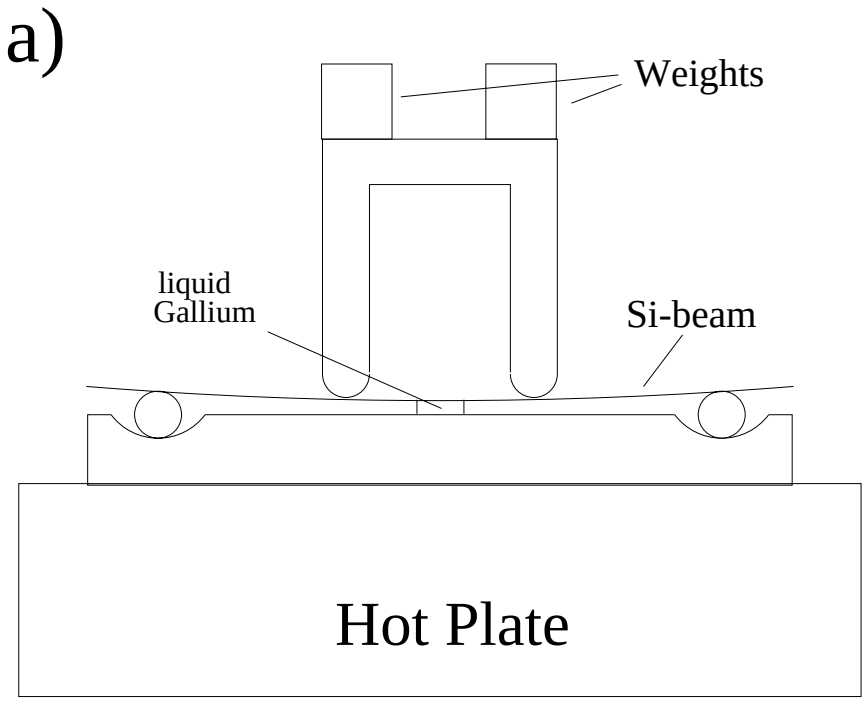

b)

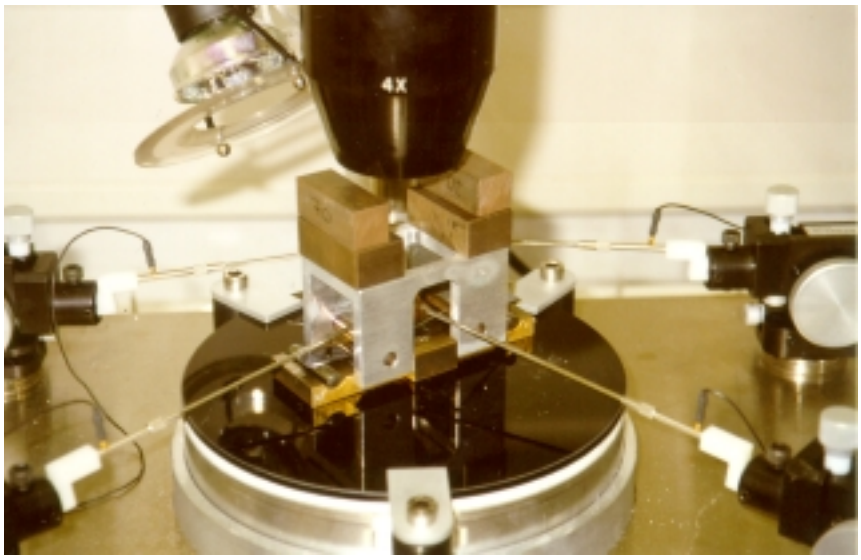

Figure 3.8: (a) Schematical presentation of the four point bending apparatus for applying compressive stress. (b) Four point bending apparatus used in the experiment.

3.5 Stress Measurements by Wafer Curvature Technique

The wafer curvature technique is one of the most common methods to determine the stresses in thin films on substrates. It is based on the fact that a stress in the film will lead to a curvature of the film-substrate composite. This curvature can be measured with a laser scanning apparatus [38] and the stress in the film can be calculated using the Stoney equation [39]

$$\sigma = \frac{E}{1-\nu}\,\frac{h_s^2}{6h}\,\frac{1}{R}, \tag{3.7}$$

where $\mathrm{E}/(1-\nu)$ is the biaxial modulus of the substrate, $1/R$ the curvature of the substrate, and h_s and h are the thicknesses of the substrate and film, respectively. This relation is valid if the substrate is elastically isotropic and the film is much thinner than the substrate. Information about the film elastic properties and flow stresses as a function of temperature can be obtained by thermal cycling the film-substrate composite. Due to the difference in thermal expansion coefficients between the film and the substrate biaxial strains (and stresses) can be imposed in the film by varying the temperature and the corresponding changes in film stress can be determined by measuring the curvature.

To determine the stress in the multilayer film samples used for electromigration testing, the curvature due to the Al/TiN composite film is measured first, then the Al film is etched away and the curvature due to the TiN film is measured. Subtracting the curvature due to the TiN film from and the curvature due to the Al/TiN composite film and substituting the resulting curvature in equation 3.7 yields the stress in the Al.

All measurements were performed using a wafer curvature apparatus in a vacuum furnace at Bell Labs [38], because experiments in the controlled atmosphere system (ROSE) at MPI led to irreproducible results, which were attributed to oxidation of the TiN films. The Bell System has also the advantage that small sample pieces ($0.5\mathrm{cm} \cdot 1.5\mathrm{cm}$) can be used rather than full wafers. On the other hand, the determination of absolute stresses is quite difficult due to the fact there may be thickness gradients in the substrate after the polishing process, which was performed to increase the curvature signal, and due to the fact that the wafers

are not flat and positioning of the scanning laser in the same place on the sample after the Al film removal is difficult. This leads to uncertainties of roughly ± 50MPa in the value of the stress.

3.6 Characterization Methods

3.6.1 Grain Size Analysis with the Focussed Ion Beam (FIB) Microscope

The FIB Microscope (FEI 200xP) works basically the same as a conventional secondary electron microscope (SEM), except that Ga ions are used instead of electrons as the primary beam. The Ga ions are emitted from a liquid-metal ion source, accelerated by a high voltage (30keV) towards the sample, and scanned by electrostatic lenses. When the ions hit the sample surface they scatter with the sample atoms and cause physical sputtering combined with secondary electron emission. If the orientation of the sample is such that the ions channel into the crystal, then fewer secondary electron are emitted. The variable extent of secondary electron emission leads to different contrast in a FIB image for different crystal orientations. Therefore, the FIB microscope can be used to make the grain structure of a material visible. An additional advantage of the FIB is that, because the ions cause sputtering, they can be used for making cross sections of the samples or for removing the native oxide from Al so that the microstructure can then be imaged.

For determining the grain size of the electromigration test samples, FIB images were used in conjunction with image analysis software provided with the microscope. To unambiguously identify single grains, three images of the microstructure at different tilt angles ($15°, 20°, 25°$) were taken (Fig. 3.9), because at a single tilt angle adjacent grains may still have the same contrast [40]. The three images were then aligned by the software using three alignment marks "drilled" with the FIB in the field of view. The aligned images were converted to a binary image of the grain structure. The measured grain sizes were plotted as a log-normal distribution, as shown in Fig. 3.10. From this, the median grain size d_{50} and the standard deviation σ were calculated.

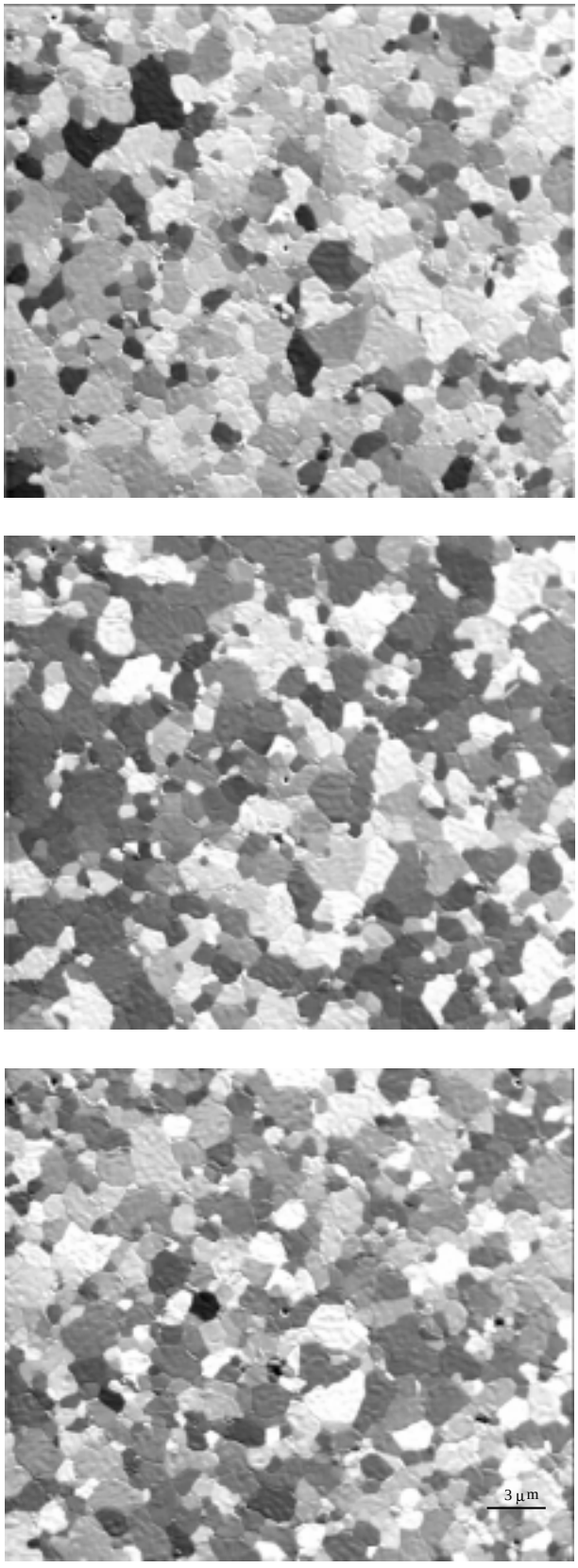

Figure 3.9: FIB images of a 600nm thick Al film annealed for 1 hour at 400°C at three different tilt angles $(15°, 20°, 25°)$.

The deviation from log-normal behavior at small grain sizes is due to the limited spatial resolution of the FIB and does not represent the true distribution of grains in the film. It is not clear whether the deviation at large grain sizes is a real effect or an artifact of the imaging method.

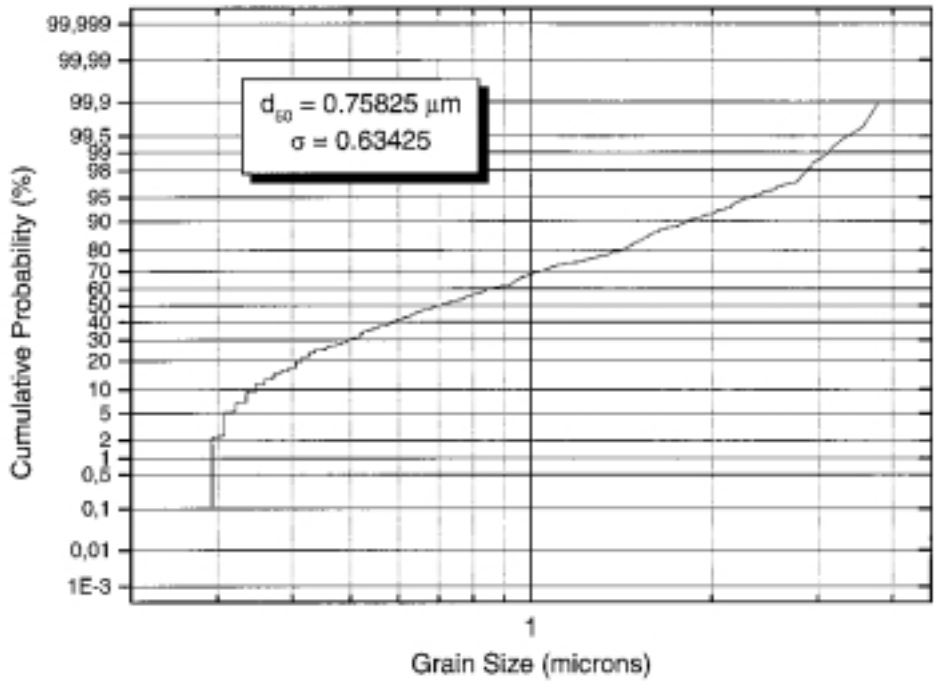

Figure 3.10: Example of a grain size distribution of a 600nm thick Al film annealed for 1 hour at 400°C.

3.6.2 Auger and SIMS Depth Profiling

Auger electron spectroscopy (AES) provides information about the chemical composition of a sample surface. When the primary electron beam interacts with an atom in the sample, a core electron of the atom can be raised to a higher energy level and then fall back to the ground state by either emitting a photon or an electron. The emitted electrons have a very low energy (a few hundred eV) and are called Auger electrons. Because of their low energy they can only be detected from the first few monolayers of a surface. In order to get information about the element distribution as a function of depth, an unfocussed Ar ion beam is

used in an UHV environment to sputter away the surface which is subsequently analyzed.

Secondary Ion Mass Spectroscopy (SIMS) also provides information about the chemical composition of a sample surface. This technique has been used in conjunction with the FIB. By sputtering the sample surface with Ga ions, secondary ions are created and analyzed in a quadrupole SIMS detector. Depending on the material, element detection can be comparable to the AES technique but quantification is much more difficult because the secondary ion yield depends strongly on the element, the matrix surrounding the element and the presence of oxygen.

3.6.3 X-ray Analysis

X-ray diffraction was used to characterize the Al/TiN/Ti films from which the electromigration test samples were made. $\theta - 2\theta$ scans were used for phase determination and for qualitative determination of texture components [41]. Rocking curves were used to determine the angular width of a given diffracted beam. The angular width of the rocking curve is a measure of the sharpness of the crystal texture in the sample.

Chapter 4

Results

In this chapter the experimental results are presented. First, the films that were used for making the electromigration samples are characterized both in the as-deposited condition and after annealing at 400 °C for one hour in air. Then, measurements of the resistivity of the electromigration samples as a function of temperature and current density are presented. These are then used to determine the sample temperature during testing. After this, the influences of current density, film thickness, temperature, annealing treatment and externally applied stress on the electromigration critical product are reported. Finally, FIB and Electron Back-Scatter Diffraction (EBSD) investigations of the morphology and orientation of electromigration-induced hillocks and depleted regions are shown.

4.1 Characterization of Films

The measurements presented later in this chapter show that the electromigration critical product depends on the sample annealing history as well as on the film thickness. Therefore, detailed characterization of the as-deposited and annealed films of different thicknesses used for making the electromigration test samples was carried out. Particular attention was paid to microstructure (grain size and texture), the Al/TiN interface, the native oxide and thermomechanical properties.

4.1.1 Grain Size

The distribution of grain sizes in the 100, 200, 400, 600 and 800nm annealed films as determined using the FIB are plotted log-normally in Fig. 4.1. All films were annealed for 1 hour at 400 °C in air before the analysis. The median grain size was found to be on the order of the film thickness (Fig. 4.2), as expected [42], except for the 800nm thick film where the median grain size was roughly twice the film thickness. The deviation of the median grain size increases with the thickness of the film.

For all films other than the 800nm thick film the grain size distribution before and after annealing was the same. This was clear from the fact that the as-deposited grain structure, visible from the surface grooves (which did not move during annealing), coincided with the annealed grain structure, visible by the channeling contrast of the FIB. In the 800nm thick film, annealing did produce grain growth and both the as-deposited grain structure, as evidenced by the surface grooves and the larger annealed grain structure, as evidenced by the channeling contrast, were visible in a single image. The fact that grain growth occurs in the 800nm thick film and not in the thinner films might be explained by assuming that there exists a driving force for grain boundary motion which increases with film thickness and becomes strong enough to overcome the pinning effect of the surface grooves. Such a driving force could be the plastic strain energy in the film due to point defect clusters and dislocations or texture-induced variations in elastic strain energy.

4.1.2 Texture

The texture of a 600nm thick as-deposited and annealed Al film was investigated by $\theta - 2\theta$ scans and rocking curves using X-ray diffraction (CuK_α radiation). The $\theta - 2\theta$ scans for 2θ between 20 and 110° showed only (111) and (222) reflection from Al indicating a strong (111) texture for both the as-deposited and annealed film (Fig. 4.3). The Ti (100), (201), and (202), the TiN (111) and (311), and the Si (200) and (400) diffraction peaks were also observed. Other phases and textures were not detectable. Rocking curves of the Al (222) reflection showed a single peak with a full width at half maximum (FWHM) of around 5° (Fig. 4.4)

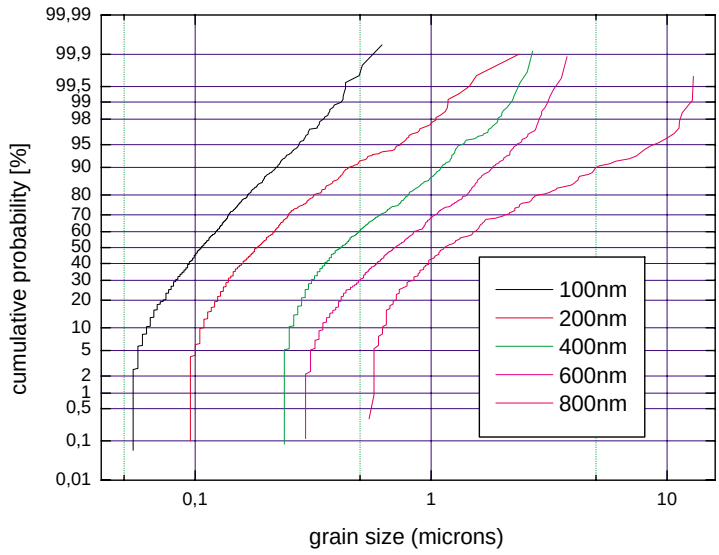

Figure 4.1: Log-normal grain size distribution of 100, 200, 400, 600 and 800nm thick Al films after annealing for 1 hour at 400 °C.

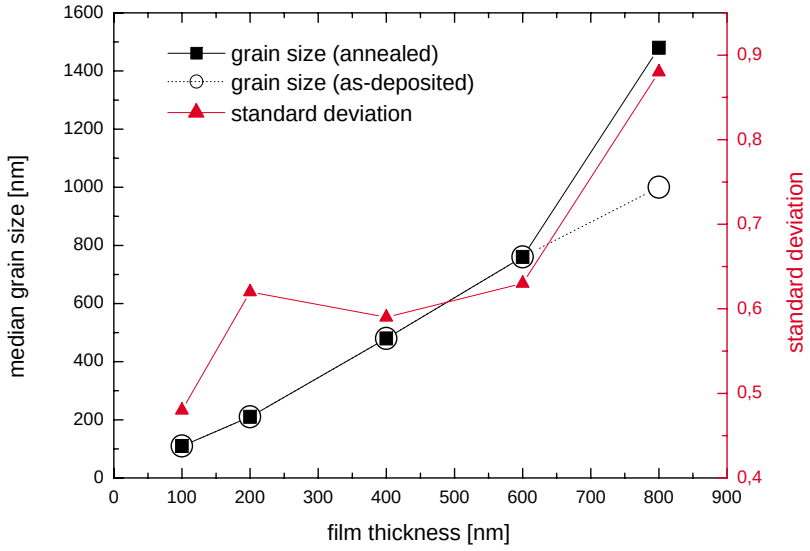

Figure 4.2: Median grain size and standard deviation of the annealed films and median grain size of as-deposited films.

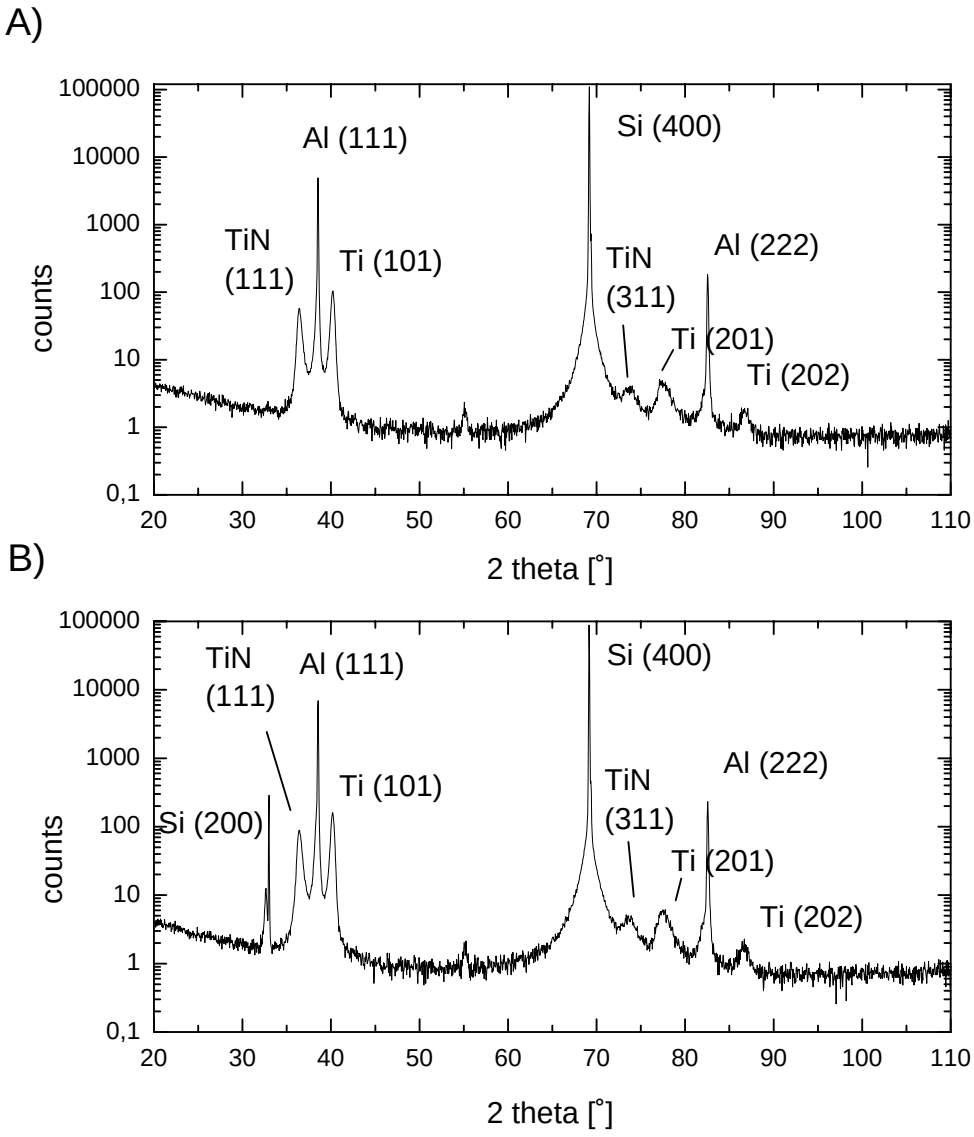

Figure 4.3: $\theta - 2\theta$ scan of A) as-deposited and B) annealed 600nm thick Al films on $TiN/Ti/SiO_2/Si$.

for both the as-deposited and annealed film, indicating that the (111) texture distribution was unchanged by the anneal.

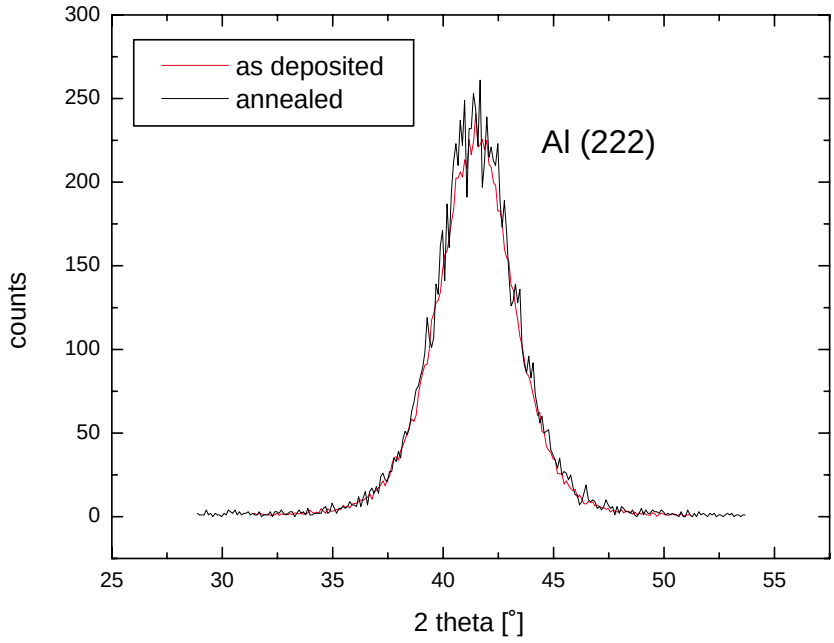

Figure 4.4: Rocking curve of the Al (222) reflection for as-deposited and annealed 600nm thick films.

4.1.3 Characterization of the Al/TiN Interface

As discussed in Chapter 2, there is some evidence in the literature that the Al/TiN interface can influence the critical product. Therefore, the Al/TiN interface was characterized in detail using Auger depth profiling, X-ray analysis, and cross-sectional TEM, in both the as-deposited and annealed films.

Auger depth profiles

To investigate if there was any redistribution of elements at the Al/TiN interface due to the annealing treatment, an Auger depth profile was performed. The Ar sputter process causes some roughness, because the sputter rate depends on the specific orientation of the Al grains and differs from grain to grain which leads to an increasing roughness with increasing sputter time. To minimize the sputter-induced roughness, a 200nm thick Al film was chosen since the initial surface roughness was found to be lower than for the thicker films and since the sputter time to reach the Al/TiN interface is shorter than for the thicker films.

The results for the as-deposited and annealed 200nm thick Al films are compared in Fig. 4.5, where the normalized counts per second (cps) of the Auger electrons from various elements are plotted against sputter time. At the beginning of the measurements only electrons from Al are observed. After around 14 minutes of sputtering the Al signal decreases and at the same time signals from nitrogen and titanium are observed and start increasing. After roughly 27 minutes the signal from Al is close to zero and the signal from nitrogen and titanium have reached their maximum value. Using the nominal thickness of the Al and TiN, the sputter rate of Al can be estimated from Fig. 4.5 to be approximately 11.1 nm/minute and for TiN 4.4nm/minute.

The point at which the Al signal decreases and the Ti and N signals increase (marked by the first dashed line) starts slightly earlier for the as-deposited sample (Fig. 4.5 A) than for the annealed sample (Fig. 4.5 B), which might be due to local variations in film thickness as a function of position or just due to intrinsic variations in the sputter rates in the Auger microprobe. The width of the interface region is roughly the same for both samples and can be estimated as lying between 100 and 200nm, based on the sputter rates of the pure Al and pure TiN films.

This width may be caused by roughness, by the presence of an interface reaction

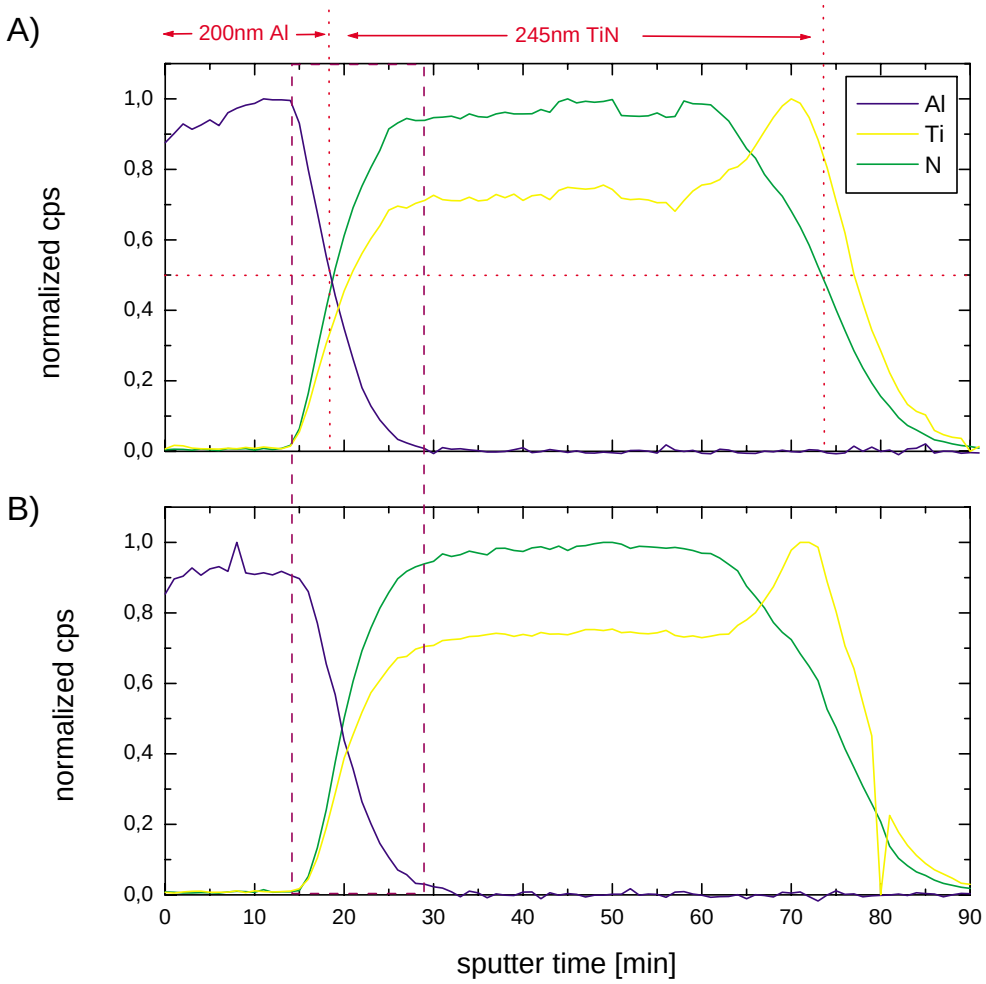

Figure 4.5: Auger depth profiles of 200nm thick Al films on 200nm TiN/45nm Ti/200nm SiO_2/Si: A) as-deposited B) annealed at 400 °C for 1 hour.

layer or an interdiffusion zone at the original Al/TiN interface, or by sputter-induced roughness. The sputter-induced roughness (defined as the root mean square of the difference between the local depth and the mean sputtered depth) of polycrystalline Al films has been investigated for the Auger system used here by Wöhner [43] and was found to be 40nm for a mean sputter depth of 170nm. The

extent of the interface region during sputtering is expected to be roughly twice the sputter-induced roughness. Assuming that the sputter rate of the interface region is similar to the arithmetic average of the sputter rate for Al and TiN, this leads to an absolute extent of the interface region of roughly 117nm, which is slightly more than twice of the sputter-induced roughness found be Wöhner. Therefore, the observed interface width in Fig. 4.5 is likely completely due to sputter-induced roughness and does not allow a comparison of the interface morphology of the as-deposited and annealed samples.

X-Ray Analysis

Phase determination was performed by a $\theta-2\theta$ scan on as-deposited and annealed 600nm thick pure Al films, as shown and already described in Fig. 4.3. There is no difference observable in these two scans, except that the annealed film shows an additional intensity peak at 32.9 ° which corresponds to the forbidden (200) reflection of Si. Subsequent measurements of as-deposited samples also showed the (200) Si peak. This peak is not expected to show up and it is not entirely clear why it does, but it might be due to some damage in the silicon. In any case, it is not an indication of any changes in the overlying films so it was not investigated further.

Both the as-deposited and annealed films show peaks for Al, Ti, TiN and Si. Neither film shows evidence of additional phases. In particular, there is no sign of $TiAl_3$. However, a thin and/or untextured reaction layer at the interface would not be detectable with the available intensity of the x-ray source.

TEM Investigations

For TEM analysis of the Al/TiN interface, cross-sectional samples of an as-deposited and an annealed 600nm thick Al film were prepared using thinning by Argon milling as described in [44]. After the preparation, an area along the interface of roughly 4 μm in length was thin enough to be investigated by TEM.

The Al/TiN interface of the as-deposited film (Fig. 4.6) looks flat and smooth, whereas the interface of the annealed film (Fig. 4.7) is much rougher and contains precipitates. The resolution of the TEM was not good enough to determine the

phase of the precipitates by selected-area diffraction, however based on reports in the literature [45], it is likely that they are $TiAl_3$ precipitates. The increased roughness of the interface of the annealed sample may be due to a combination of interdiffusion and phase formation.

The presence of interface precipitates was supported by FIB cross-sectioning and imaging of 600nm thick films from which an average precipitate density of roughly 1 per μm^2 was determined (see for example Fig. 4.43).

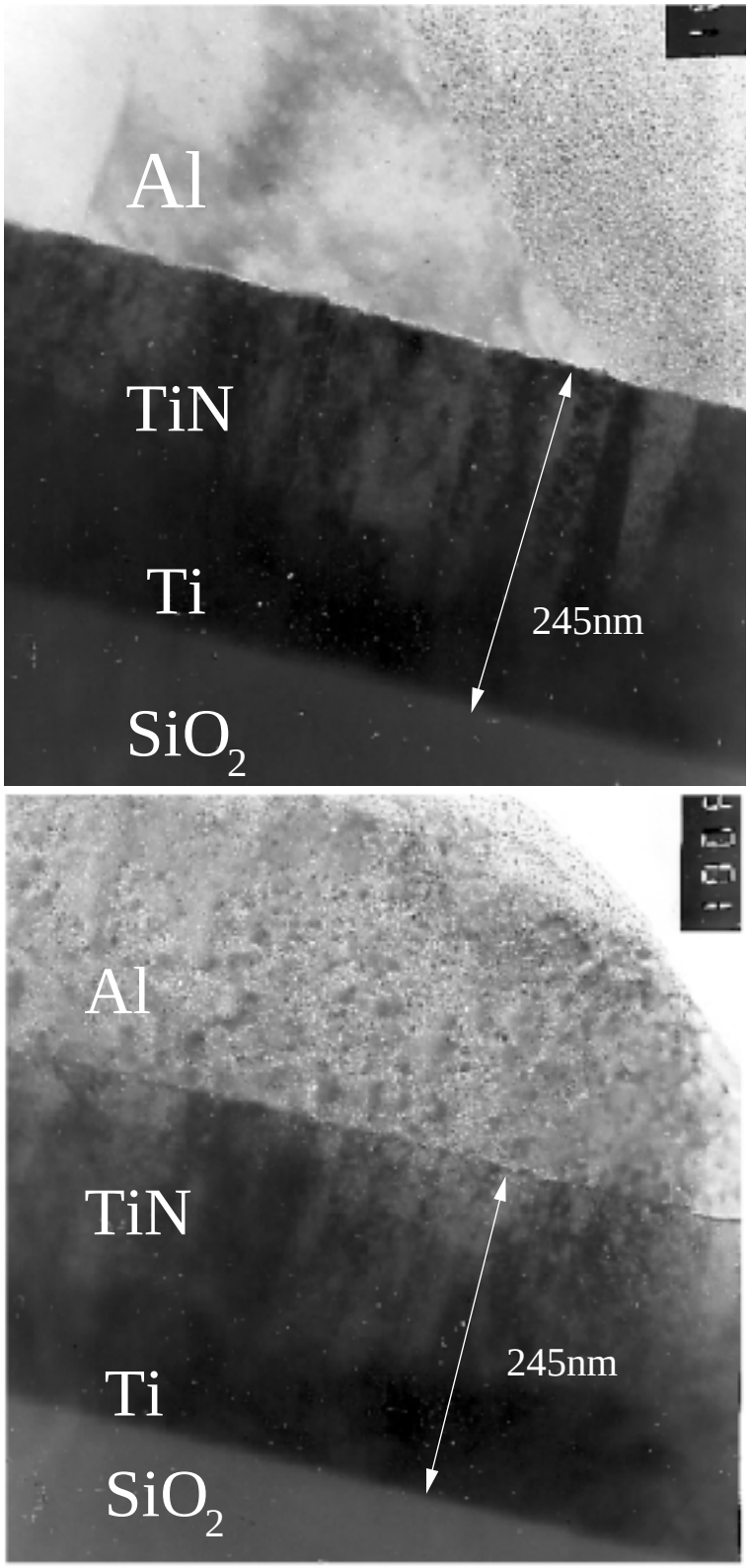

Figure 4.6: TEM cross sections of an as-deposited 600nm thick film, showing a flat and smooth Al/TiN interface.

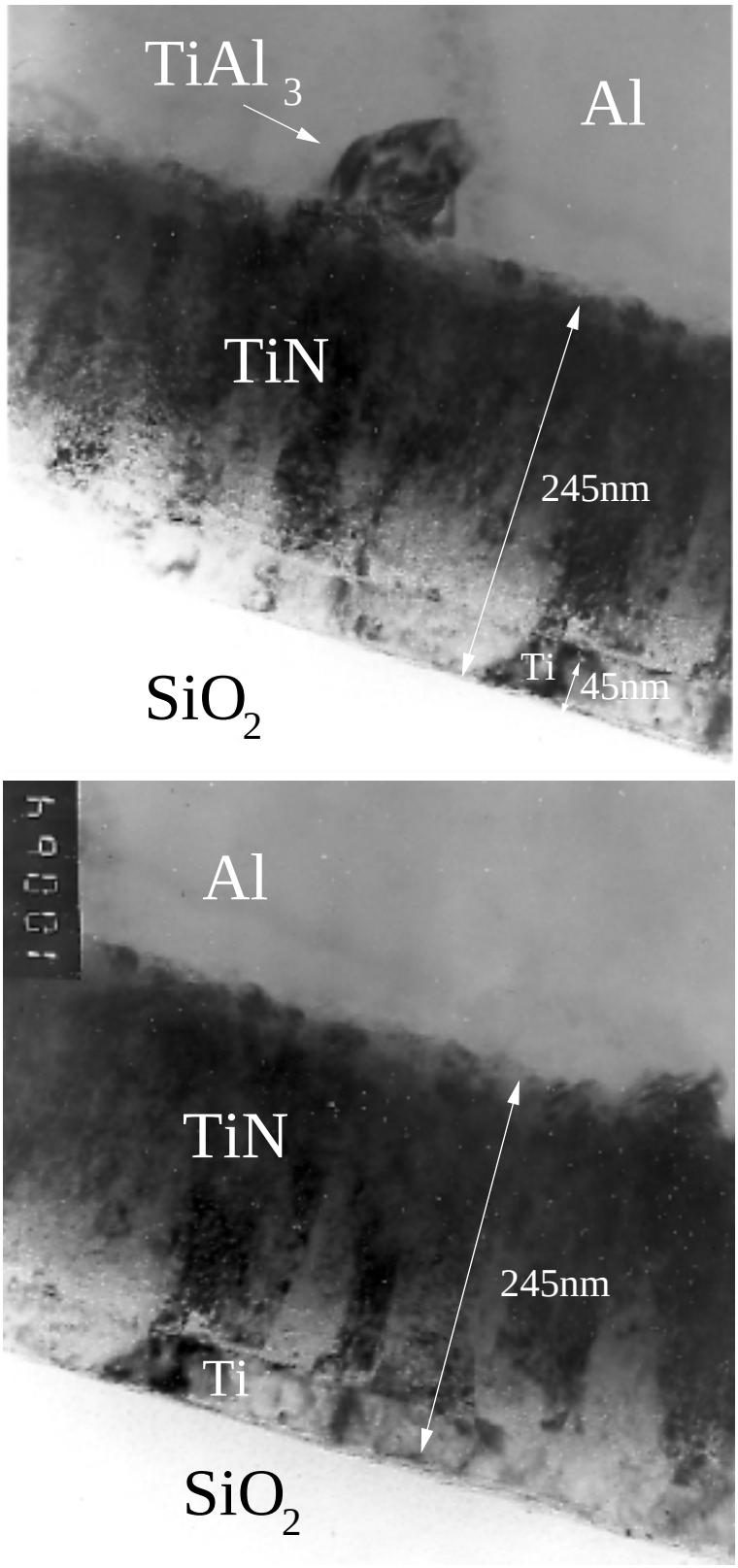

Figure 4.7: TEM cross sections of an annealed 600nm thick film, showing a rough Al/TiN interface with a $TiAl_3$ precipitate.

4.1.4 Native Oxide Thickness

As described in Chapter 2, the native oxide of Al may act as a mechanical constraint, similar to the case of passivation layer, in which case the effectiveness of the oxide in constraining the Al depends on its thickness. To measure the oxide thickness, both Auger and FIB/SIMS depth profiling of oxygen were performed, depending on the availability of the system.

The normalized Auger depth profiles for as-deposited and annealed 600nm thick Al films are shown in Fig. 4.8. The oxygen signal from the annealed oxide extends deeper into the sample than for the as-deposited sample. The sputter time at which the count rate has fallen to half the maximum value is used as a measure of the oxide thickness, indicating that an increase in thickness of roughly 40 percent occurs on annealing. Since the sputter rate of Al_2O_3 for the parameters used in the Auger microprobe is not known, the sputter rate of Ta_2O_5 was used (1nm per minute). According to this, the thickness of the native oxide for the as-deposited sample is roughly 1.3nm and for the annealed sample 1.8nm. The value for the as-deposited sample is close to the value of 1.4nm as measured by [46] for pure Al after oxidation for 1 hour at room temperature in pure oxygen.

The SIMS oxygen depth profiles of the as-deposited and annealed films (Fig. 4.9) show similar behavior: The normalized oxygen signal from the annealed film is smaller and extends deeper into the sample than for the as-deposited sample. The annealed oxide thickness, as determined from the sputter time when the count rate falls to half the maximum value, is 15 percent larger than the as-deposited oxide thickness.

Both analyses show that the native oxide for the annealed sample is thicker than for the as-deposited sample, as expected. However, the SIMS technique shows a smaller thickness increase of the native oxide than the Auger technique does. This may be due to a lower sputter yield at the beginning of the sputter process in the FIB. The steady state sputter rate in the FIB is expected to be achieved only after the surface region of the sample has been damaged or a thickness corresponding to the range of 30 keV Ga ions has been removed, because of the influence of the Ga incorporation on the sputter rate.

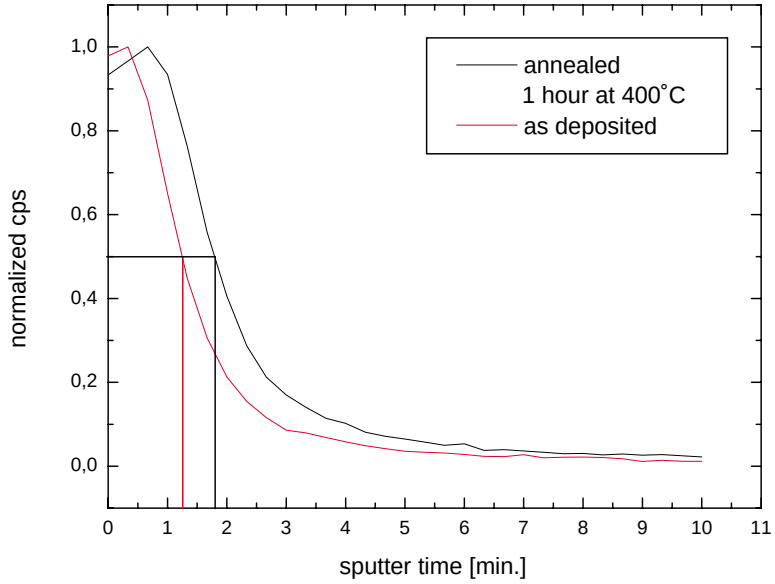

Figure 4.8: Auger depth profiles of oxygen for as-deposited and an annealed 600nm thick Al films.

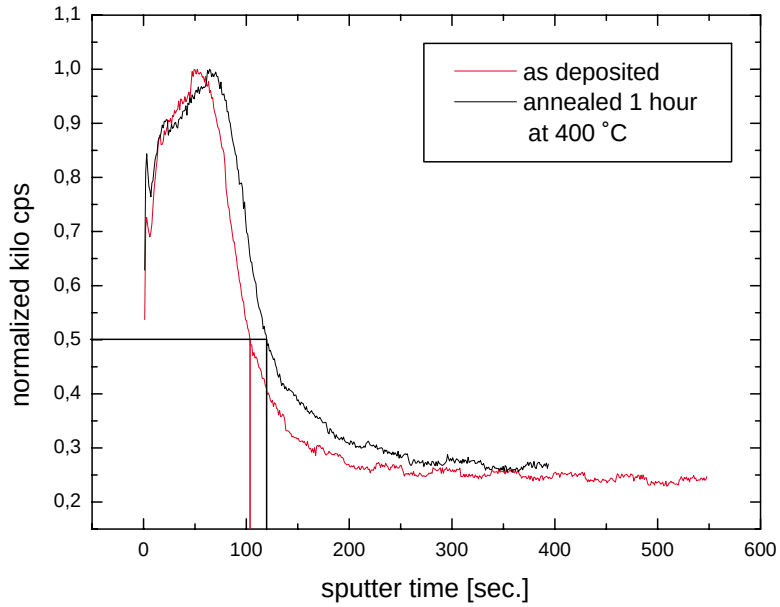

Figure 4.9: SIMS depth profiles of oxygen for as-deposited and an annealed 600nm thick Al films.

In contrast, in the Auger system, very little Ar is incorporated in the sample during sputteringand the steady state sputter rate is quickly achieved. Also, the oxygen signal in the FIB/SIMS profile does not reach zero at longer sputter times as in the case of the Auger profile. This is due to the fact that the Auger technique is carried out in an UHV environment ($5 * 10^{-9}$ mbar) whereas the pressure in the FIB chamber is around hundred times higher. This can lead to re-formation of native oxide during sputtering and also to oxygen signals from the ambient gas in the chamber.

4.1.5 Thermomechanical Properties Determined by Wafer Curvature Measurement

Since the critical product is associated with a certain threshold stress $\Delta\sigma_{th}$ it is reasonable to assume that there may be a connection with mechanical properties such as flow stress or creep behavior. Therefore, wafer curvature measurements were performed to determine the thermomechanical behavior of the films. In the following the experimental procedure is described for the 600nm thick film, and the results for the other film thicknesses are shown at the end of the section.

A 600nm thick Al film was cycled twice at a heating- and cooling rate of 20 °C/minute from room temperature to 400 °C and the stresses in the Al film were measured by the wafer curvature technique, as explained in Chapter 3. Two cycles were performed to determine the thermomechanical behavior of the films in the as-deposited and annealed condition. The heat treatment during the first wafer curvature cycle was assumed to be roughly equivalent to the 1 hour annealing treatment at 400 °C applied to the electromigration test samples.

The wafer curvature measurements were performed using the following procedure: First, the Si wafer was thinned down from 670 to 257 μm by a chemical-mechanical polishing step in order to increase the signal to noise ratio of the curvature measurement which is inversely proportional to the square of the substrate thickness. Then, two curvature cycles of the TiN/Al composite were measured at a heating- and cooling rate of 20°C/min from room temperature to 400 °C, as shown in Fig. 4.10. Finally, the Al was selectively etched from the wafer using PAE Etchant (Phosph. 85 % 16 parts, Nitric 70 % 1 part, Acetic 100 % 1 part H_2O 2 parts) and the curvature due to the TiN film alone was measured (Fig. 4.11) which shows that the TiN film behaves completely elastically in the investigated temperature regime.

To determine the stress in the Al film, the curvature of the TiN (Fig. 4.11) was subtracted from the curvature of the TiN/Al composite (Fig. 4.10) and the resulting curvature was used to calculate the stress in the Al according to the Stoney equation, as explained in Chapter 3. The stress-temperature curves for the 600nm thick Al film are presented in Fig. 4.12. Both elastic and plastic contributions were observed, similar to what is reported in the literature [47],[48], [49], [50].

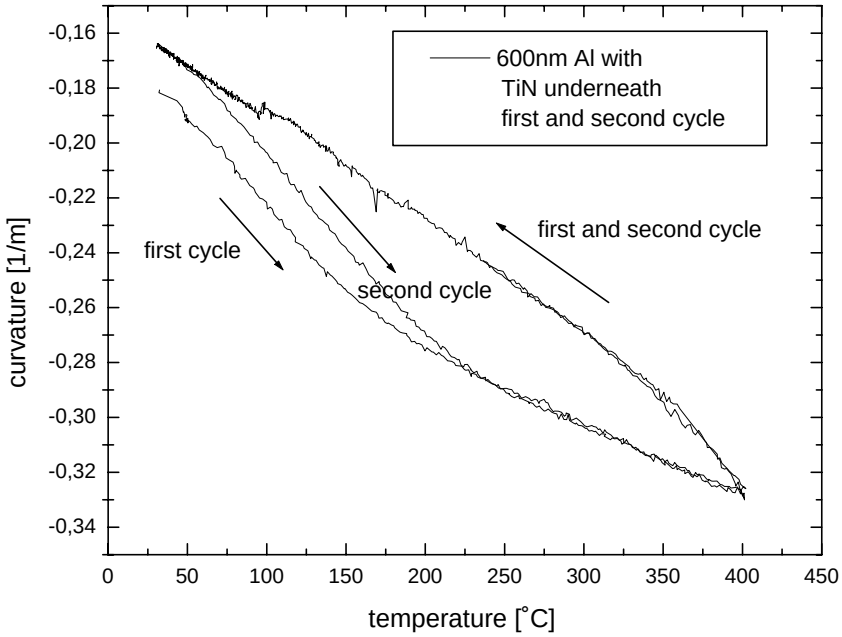

Figure 4.10: Wafer curvature measurement of a 600nm thick Al film on TiN.

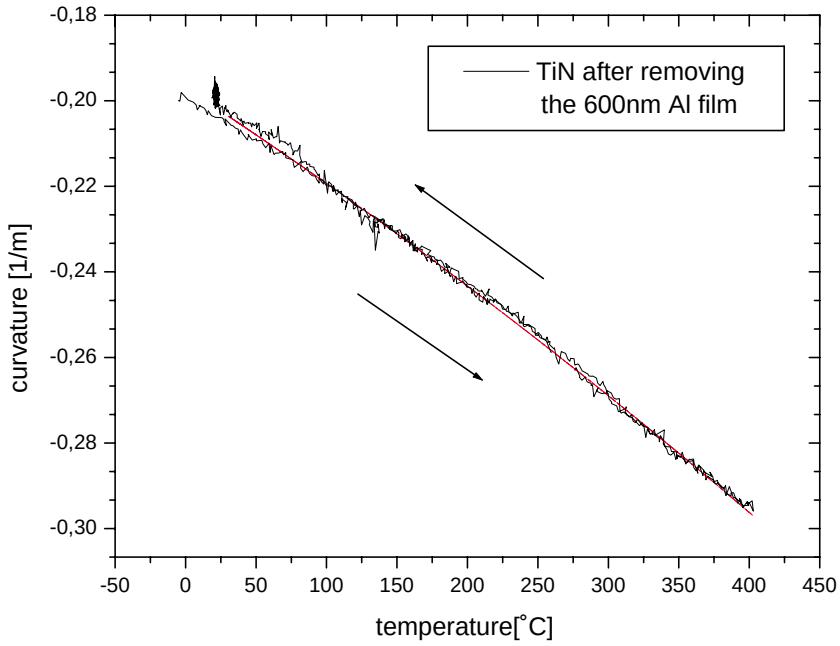

Figure 4.11: Wafer curvature measurement of the TiN film after removing the Al.

The elastic behavior on both heating and cooling is well described by a slope of 1.5 MPa/°C (red lines) which is considerably lower than the expected value for (111) textured Al of [50]

$$\mathrm{m} = \frac{\mathrm{E}}{1-\nu}\,(\alpha_{\mathrm{Al}} - \alpha_{\mathrm{Si}}) = 113.2\ \mathrm{GPa} \cdot 20.5 \cdot 10^{-6}\ {}^{\circ}\mathrm{C}^{-1} = 2.32\ \mathrm{MPa}/{}^{\circ}\mathrm{C} \qquad (4.1)$$

Repeated wafer curvature measurements on the 600nm thick film showed the same elastic slope of 1.5 MPa/°C. Similar behavior was also found by Venkatraman [47] on (111) textured polycrystalline (1.8 MPa/°C) and single crystal (2 MPa/°C) films. The low measured values might caused by some plasticity due to the low

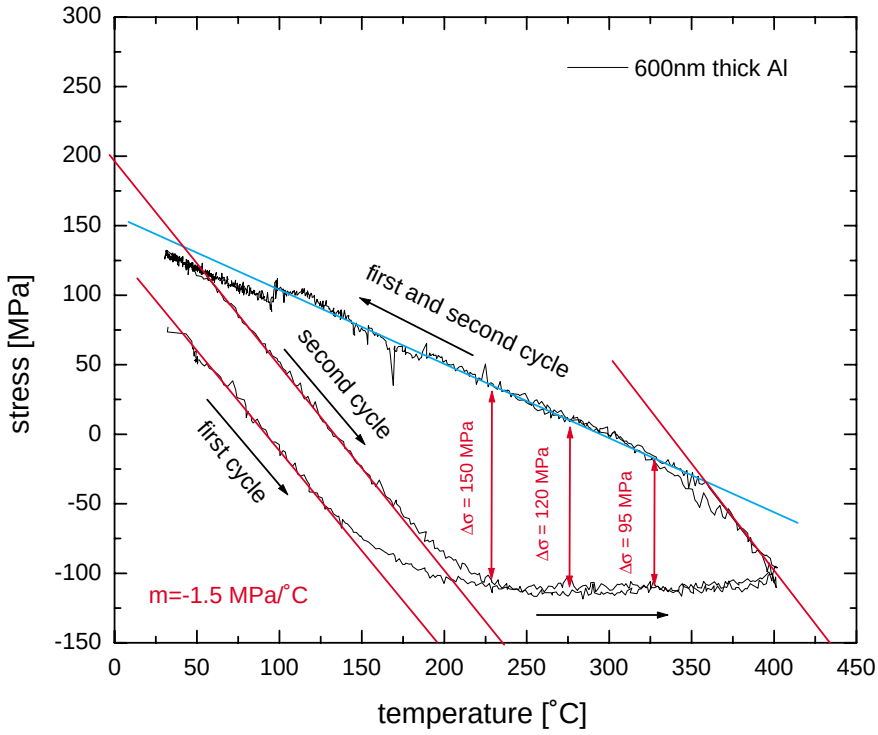

Figure 4.12: Calculated stress in a 600nm Al film as a function of temperature.

strain rate on heating ($-7 \cdot 10^{-6}\mathrm{s}^{-1}$). The deviations from the elastic behavior indicate the onset of plasticity where the value of the measured stress is taken to be an indication of the flow stress of the material at the imposed strain rate.

Except in the initial elastic portion during heating, the stresses for both cycles are equal. This indicates that heating to 400°C does not change the creep and plastic behavior of the film. The difference between the flow stress under tension and compression at the electromigration test temperature of 225°C was roughly 150 MPa during both cycles. Based on this results, it is assumed that the mechanical properties of the electromigration test samples are unchanged by the 400°C anneal.

The stress-temperature curves for the other film thicknesses (100, 200, 400, and 800nm) are shown in Figs. 4.13 - 4.16. The elastic slope (drawn in the figures) is higher than for the 600nm thick film and closer to the theoretically expected value of 2.32 MPa/°C, but there is no trend as a function of film thickness. The difference of flow stress $\Delta\sigma_f$ in compression and tension (drawn in the Figures) also shows no trend with film thickness. This is not expected, because the flow stress of thin films is generally accepted to be proportional to the inverse film thickness and inverse grain size [51], [52]. For the 100 and 200nm thick films $\Delta\sigma_f$ may not represent the actual flow stresses of the films because the stress-temperature curves do not clearly show the onset of plastic behavior as for the thicker films. For the 200, 400 and 600nm thick films $\Delta\sigma_f$ is also determined at higher temperatures and compared to the temperature dependence of the electromigration threshold stress $\Delta\sigma_{th}$ in the discussion part.

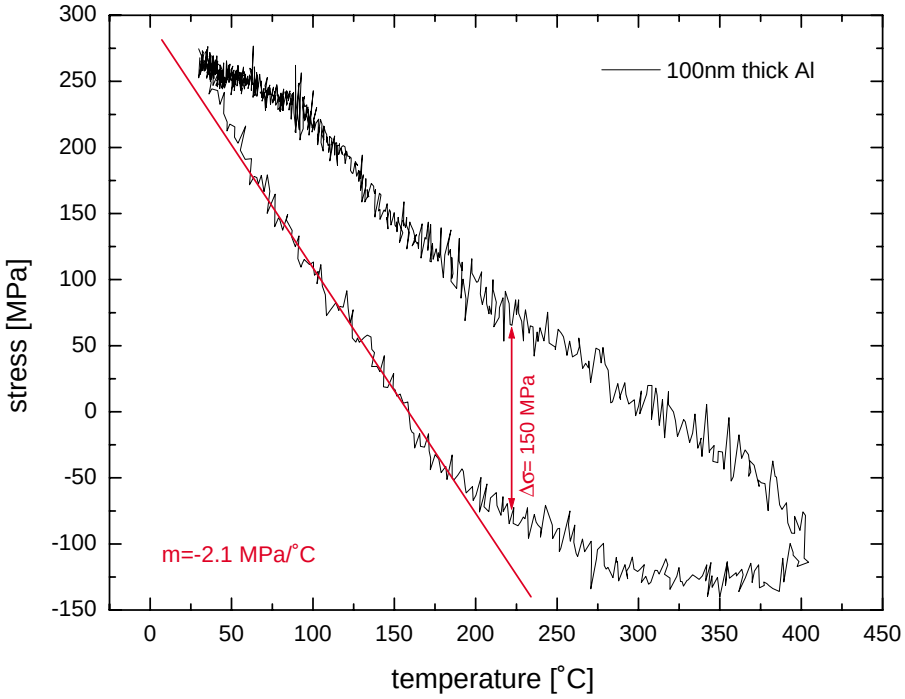

Figure 4.13: Stress in a 100nm Al film during the second cycle.

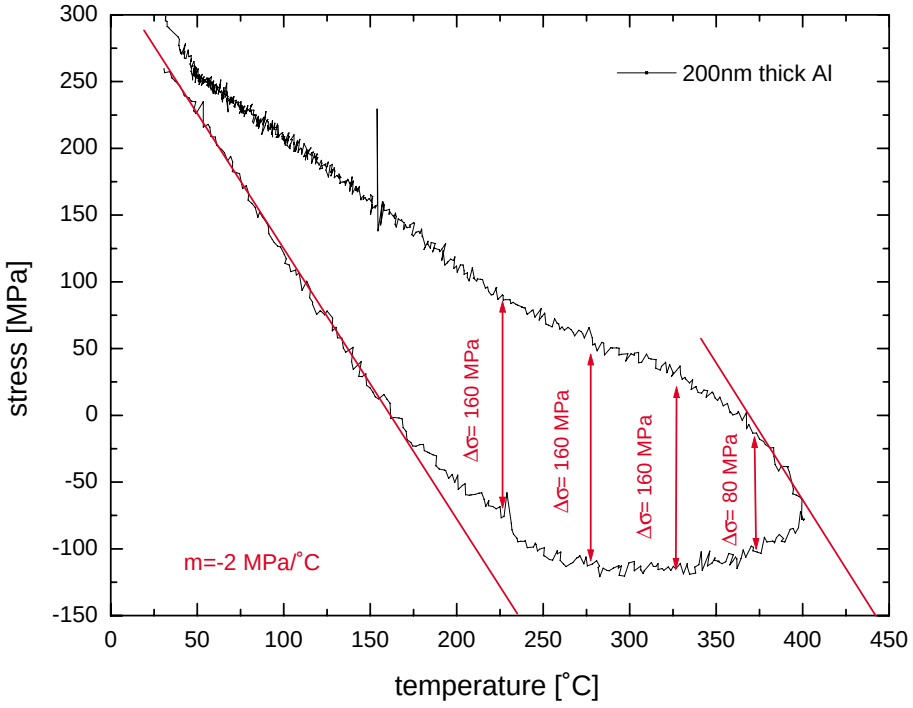

Figure 4.14: Stress in a 200nm Al film during the second cycle.

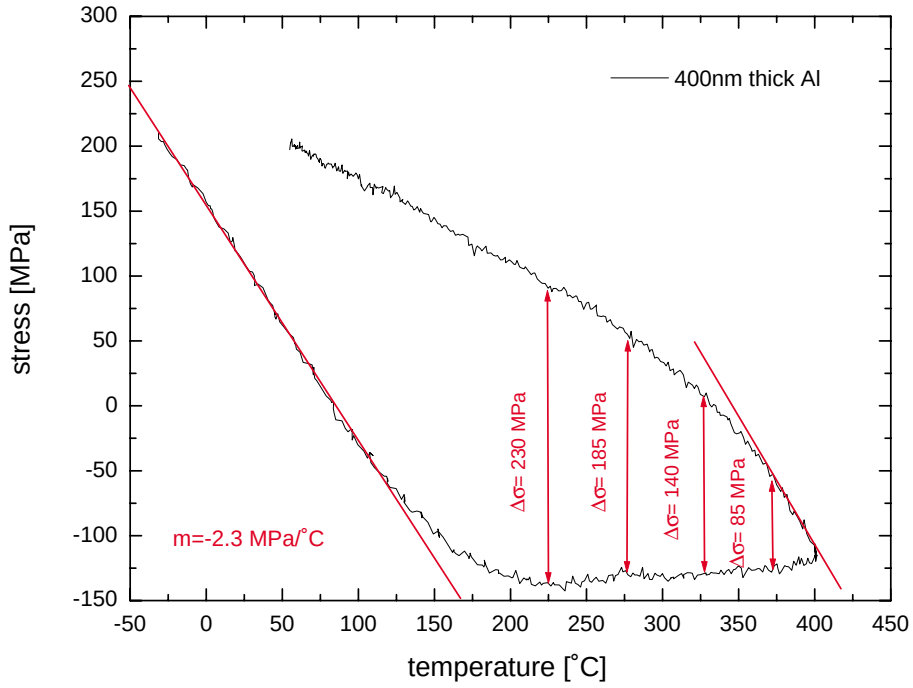

Figure 4.15: Stress in a 400nm Al film during the second cycle.

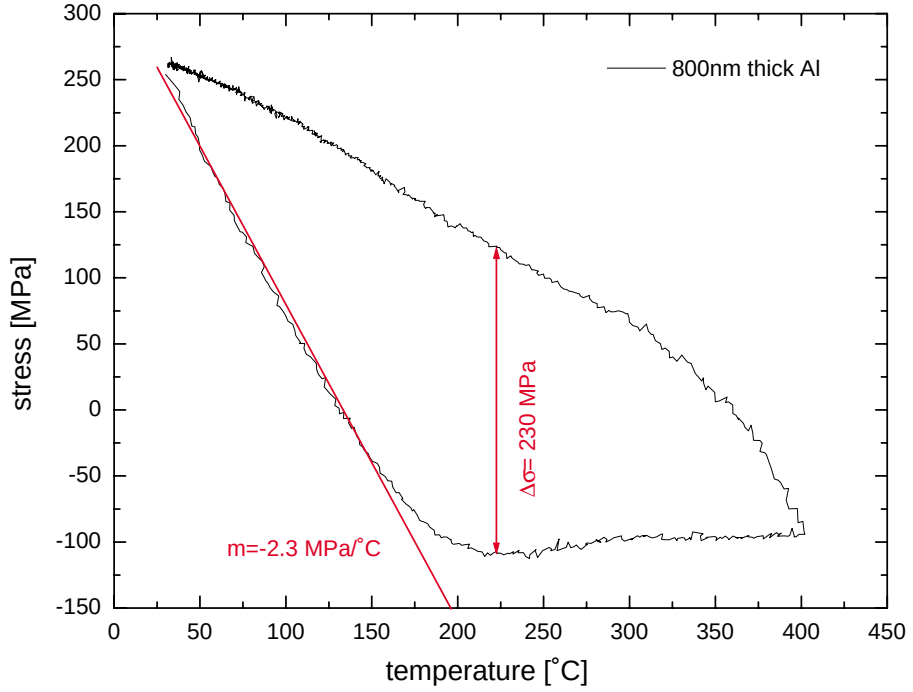

Figure 4.16: Stress in a 800nm Al film during the second cycle.

4.2 Joule Heating in the Electromigration Test Samples

During electromigration testing at elevated current densities the actual temperature of the test samples can be much higher than the temperature of the hotplate due to Joule heating. If not taken into account this can lead to incorrect conclusions, particularly when comparing the behavior of the samples made of different film thicknesses.

For example, in the test samples, Joule heating is mainly generated in the spaces between the Al segments where the current has to pass through the TiN segment with a much higher resistivity than the Al. However, the thickness of the underlying TiN stripe was always 245nm and did not scale with the Al film thickness. Therefore, in order to maintain a constant current density in the Al, the current density in the TiN stripe connecting the Al segments must vary by a factor of eight, and accordingly the amount of Joule heating generated in the TiN stripe varies by a factor of 64, since it is proportional to the square of the current density.

The temperature increase due to Joule heating in the electromigration samples cannot be determined from resistance measurements because the temperature distribution along the electromigration test sample is quite inhomogeneous due to different cross sections and different materials. Therefore, the actual temperature in the electromigration test sample was determined by the following procedure: First, the temperature increase in a continuous TiN segment (where the temperature is homogeneous) was determined as a function of current density using resistance measurements. This provides an upper limit for the temperature increase in an electromigration test sample where the current passes mainly through the Al segments on top of the TiN stripe due to their much lower resistivity. The temperature in the TiN stripe is then compared with a two-dimensional (2D) thermal finite element model and used to determine the thermal resistance between the chip and the hotplate. Finally, a more detailed three-dimensional (3D) thermal-electric coupled finite element model of the temperature distribution along an electromigration test sample was performed.

4.2.1 Temperature Increase in a Continuous TiN Stripe as a Function of Current Density

To obtain a continuous TiN stripe, the Al segments were selectively removed from the electromigration test sample using a special etching solution (Riedel-de Haen, PWS-80-16-4(65)). Then, the sample was placed on a hot plate and the resistance of the TiN stripe was measured both as a function of hot plate temperature and as a function of current density by a four point resistance measurement, as explained in section 3.3. The resistivity ρ of TiN was calculated from the measured resistance according to

$$\rho = \frac{R * w * h_{TiN}}{l} \ , \tag{4.2}$$

where R is the resistance, w the width, h_{TiN} the thickness and l the length of the stripe. The results for the resistivity as a function of temperature and current density are plotted in Figs. 4.17 and 4.18.

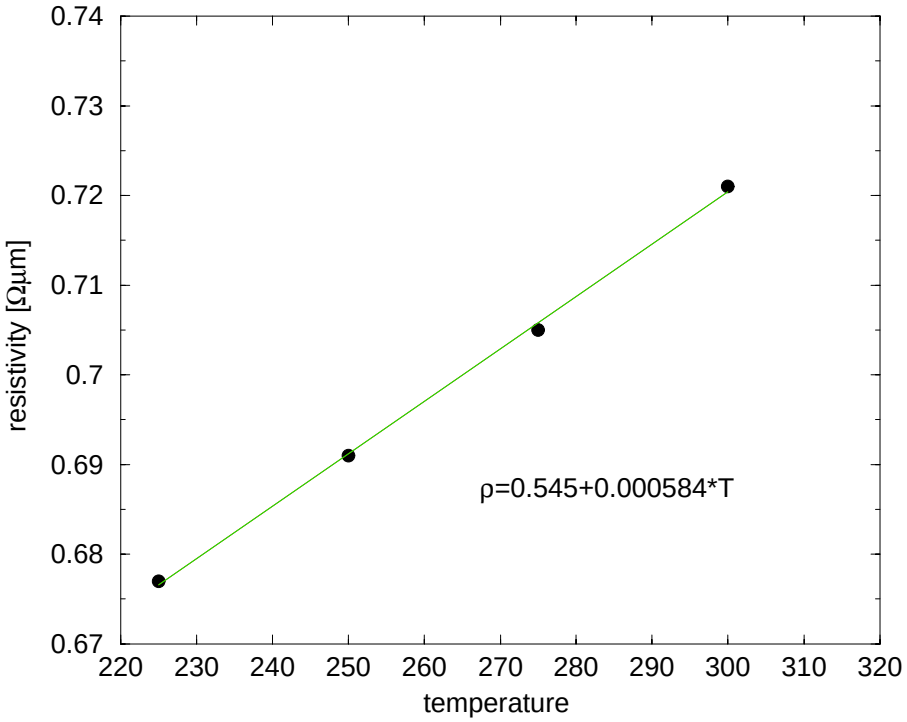

Figure 4.17: Resistivity of TiN as a function of temperature.

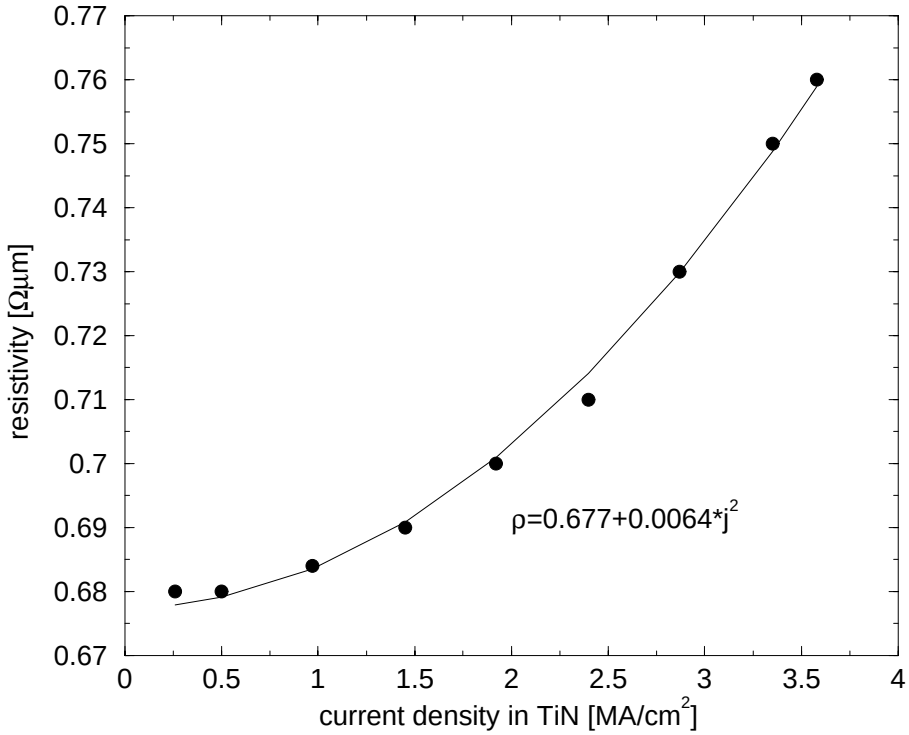

Figure 4.18: Resistivity of TiN as a function of current density (measured at a hotplate temperature of 225 °C).

The measurements as a function of hot plate temperature were performed at a low current density ($0.1 MA/cm^2$) in order to avoid significant Joule heating. The two Figures show that the resistivity of TiN increases linearly with temperature and with the square of the current density, as expected. Least square fits to the data in Figs. 4.17 and 4.18 yielded $\rho[\Omega\mu\text{m}] = 0.545[\Omega\mu\text{m}] + 0.000584[\Omega\mu\text{m}/°\text{C}] *$ T[°C] and $\rho[\Omega\mu m] = 0.677[\Omega\mu m] + 0.0064 * j[MA/cm^2]^2$).

From these two fit functions the temperature of a continuous TiN stripe (on a silicon chip on a 225 °C hotplate) can be determined as a function of current density by eliminating the resistivity. The results are plotted in Fig. 4.19. This shows that Joule heating in a TiN stripe can cause a significant temperature increase. In a real test sample, to achieve a current density of 1 MA/cm^2 in the 100, 200, 400, 600 and 800nm thick Al segments, a current densities of 0.41, 0.82, 1.63, 2.45, 3.27, MA/cm^2 is required in the 245nm thick TiN stripe connecting

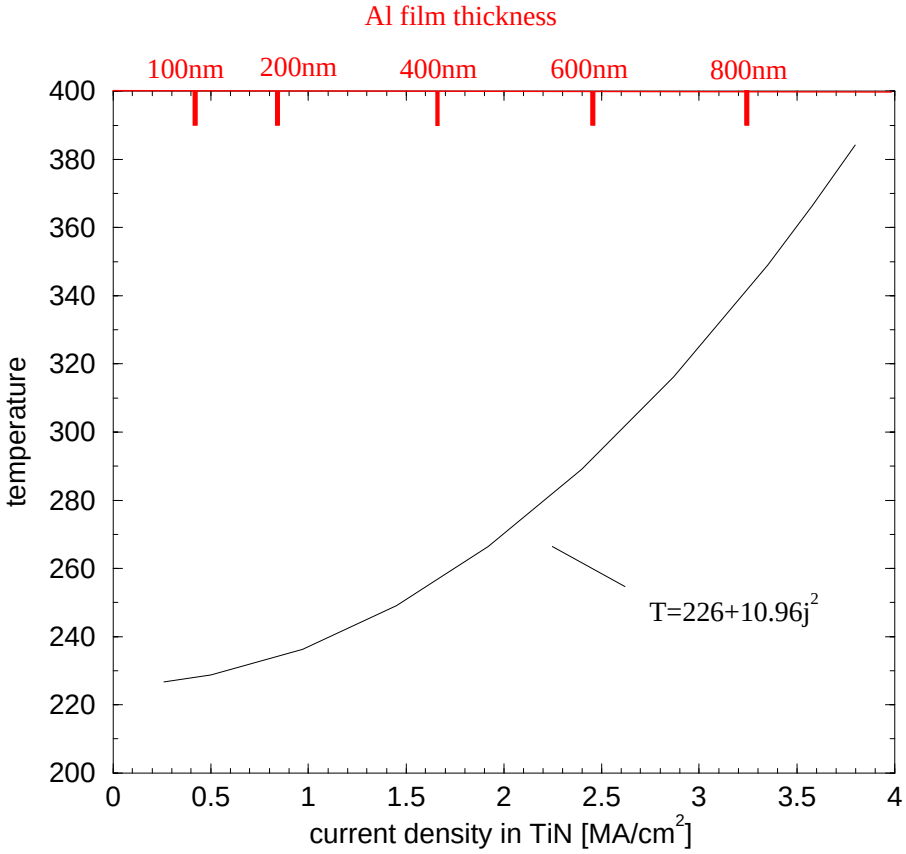

Figure 4.19: Actual temperature of a continuous TiN stripe on a silicon chip on a 225°C hotplate as a function of current density.

the Al segments (drawn on the top axis of Fig. 4.19). According to this, the upper limit for the actual temperature of an 800nm thick electromigration test sample (tested at a current density of 1MA/cm^2 on a 225 °C hotplate) would be roughly 340 °C which is significant. However, the actual temperature increase in the electromigration test structures is expected to be much lower than for a continuous TiN stripe and therefore, additional calculations have to be carried out to determine more realistic values for the actual temperature increase in the electromigration test samples.

4.2.2 Finite Element Simulation of Joule Heating

The Joule heating calculations in this section are divided into two parts: First the temperature increase of a continuous TiN stripe is calculated using a 2D thermal finite element model and compared with the experimentally determined values. From this comparison the thermal contact resistance at the bottom of the chip to the hotplate is determined (which is the only unknown parameter in the model). The real test sample containing Al segments on top of the TiN is then simulated by a 3D electric-thermal coupled finite element model using the thermal resistance between the chip and the hotplate determined from the 2D calculation. The finite element calculations were carried out using the commercial software ANSYS 5.4. The material parameters used are listed in the source code in Appendix C.1.

Simulation of the Temperature Increase along a Continuous TiN Stripe using a 2D thermal finite element model

A 2D thermal finite element model of a cross section of a continuous TiN stripe was set up to calculate the temperature increase as a function of current density (illustrated in Fig. 4.20). Due to the symmetry it is sufficient to model only half of the cross section. The geometrical dimensions of the 2D cross-sectional model corresponded to the dimensions of the electromigration test sample (8.6 μm wide and 245nm thick TiN stripe on a 670 μm thick Si substrate with 200nm thick SiO_2 on top and bottom). The substrate width in the model was set to 2mm, even if the actual substrate width is much larger, because it was found that a substrate width of more than 2mm did not influence the calculated temperature in the TiN stripe. The bottom of the test chip was set to the hotplate temperature of 225 °C. At all other faces adiabatic boundary conditions were applied. Convection and radiation were not considered in the model. The heat generation rate per unit volume in the TiN due to the electrical current was calculated according to $P/V = \rho * j^2$, where P is the power, V the volume, ρ the resistivity and j the current density (electric-thermal coupled elements could not be used in this analysis since the current direction is perpendicular to the paper plane). The following material properties were used: $\rho_{\mathrm{Al}} = 3.4\Omega\mu\mathrm{m}$, $\lambda_{\mathrm{Al}} = 237\mathrm{W/Km}$, $\rho_{\mathrm{TiN}} = 50\Omega\mu\mathrm{m}$, $\lambda_{\mathrm{TiN}} = 200\mathrm{W/Km}$, $\lambda_{\mathrm{SiO_2}} = 1.3\mathrm{W/Km}$, $\lambda_{\mathrm{Si}} = 148\mathrm{W/Km}$, where λ is the

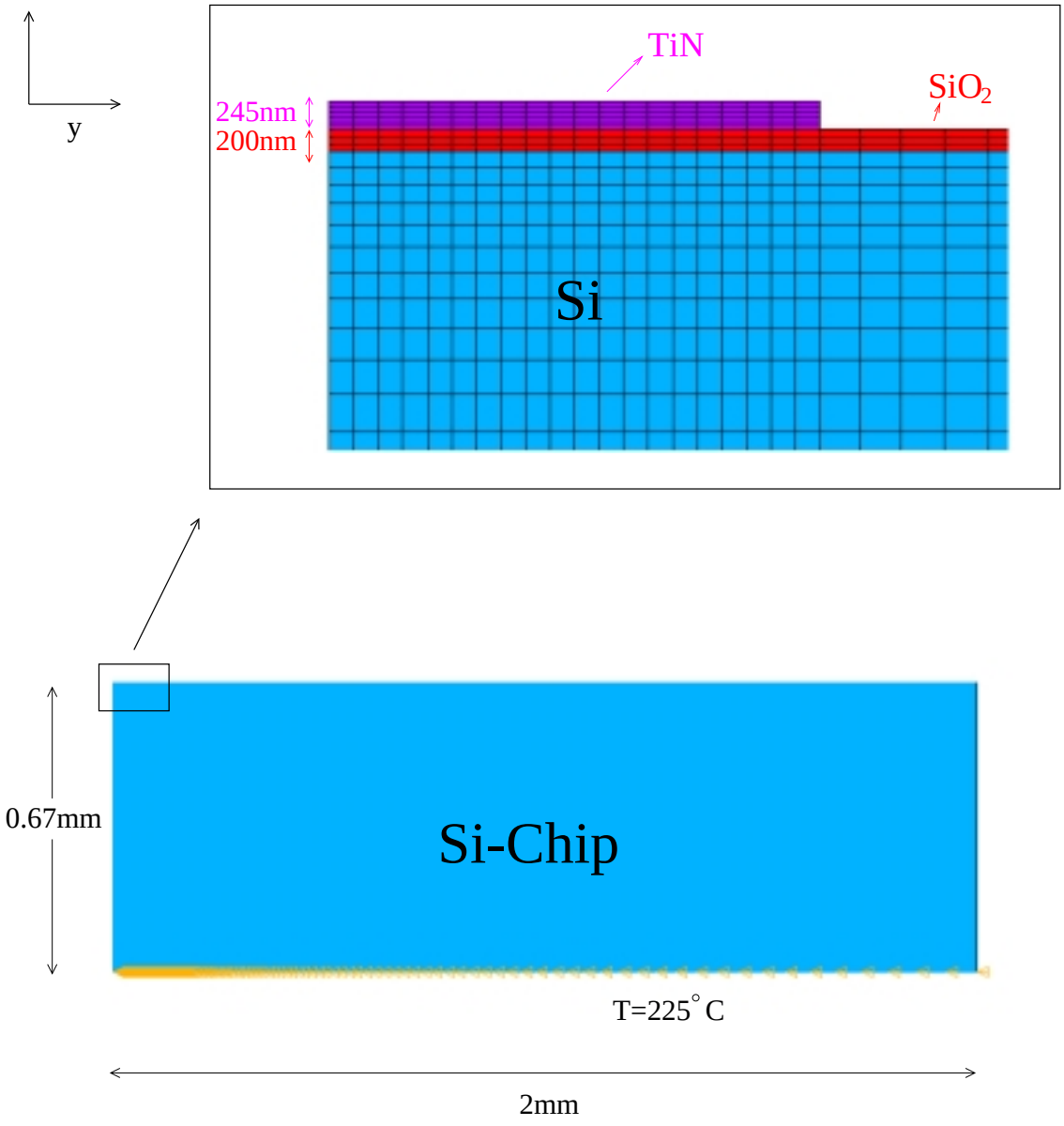

Figure 4.20: 2D thermal finite element model of a cross-section through a continuous TiN stripe. Due to the symmetry only half of the cross section was modelled.

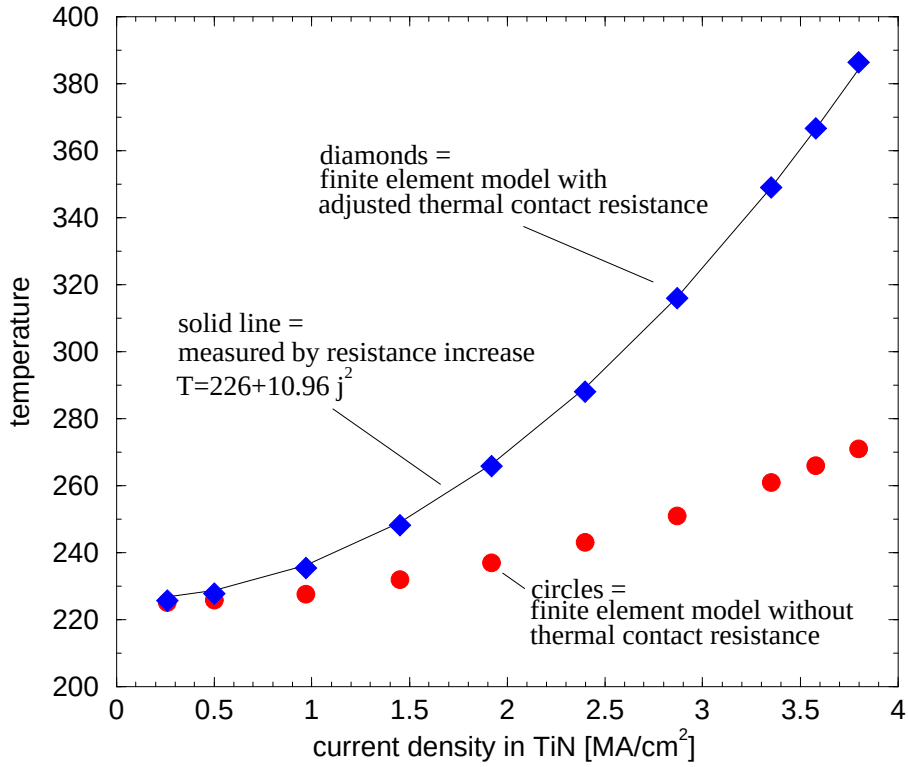

Figure 4.21: Modelled (data points) and measured (solid line) temperatures of a TiN line as a function of current density.

thermal conductivity.

Fig. 4.21 shows the results of the model (circles) and the experimentally determined values (solid line), as already presented in Fig. 4.19. The calculated temperatures are much smaller than the measured ones. This discrepancy is likely due to a high thermal resistance between the bottom of the chip and the hotplate. The heat transfer between the unpolished Si/SiO_2 surface and the hotplate, which are only pushed against each other by the weight of the chip and the force of the contact probes, is expected to be quite poor.

To simulate the high thermal resistance between the chip and the hotplate, the thermal conductivity of the SiO_2 layer was reduced until the calculated values for the temperature increase were equal to the experimentally measured values, as shown in Fig. 4.21 by the squares. The agreement of the calculated and measured

values was obtained with a thermal conductivity of $\lambda = 0.68 \cdot 10^{-3}$W/Km for the bottom SiO_2 layer which is roughly a factor of 2000 lower than the thermal conductivity of SiO_2.

Simulation of the Temperature Increase in a Test Sample using a 3D electric-thermal coupled finite element model

After approximating the thermal contact resistance between the silicon chip and the hotplate by reducing the thermal conductivity of the bottom SiO_2 layer, a 3D electric-thermal coupled finite element model was set up to calculate the local temperature increase in an Al segment on top of the TiN stripe in a real test sample.

A coupled-field analysis takes the interaction of two or more fields into account. Two distinct methods of a coupled field analysis can be identified, the direct and indirect method. The indirect method involves two sequential analyses where the fields are coupled by applying the results from the first analysis as loads for the second analysis. The direct method involves just one analysis that contains all necessary degrees of freedom. The direct method is best suited for recursive coupling situations, whereas the indirect method is generally used in coupling situations, where the solution of one field only affects the solution of the other, but not vice-versa. The finite element analysis in this section was performed by the indirect method. The current density field affects the temperature field due to Joule heating but the temperature field does not in turn affect the current density field significantly, because the resistivity increase of Al and TiN is below 6 percent in the range of 225 to 325 °C.

A part of a typical test sample is shown schematically Fig. 4.22. The length difference between adjacent Al segments is only 2 μm and therefore will be ignored. The symmetry resulting from this simplification reduces the number of elements and saves computing time because only a quarter of the considered Al segment has to be modelled, as drawn by the red line in Fig. 4.22. The calculation of the temperature increase was carried out for the 800nm thick Al sample, where the most Joule heating is expected. For a constant current density in the Al segments the thickest samples carry the highest absolute current and therefore will be the hottest.

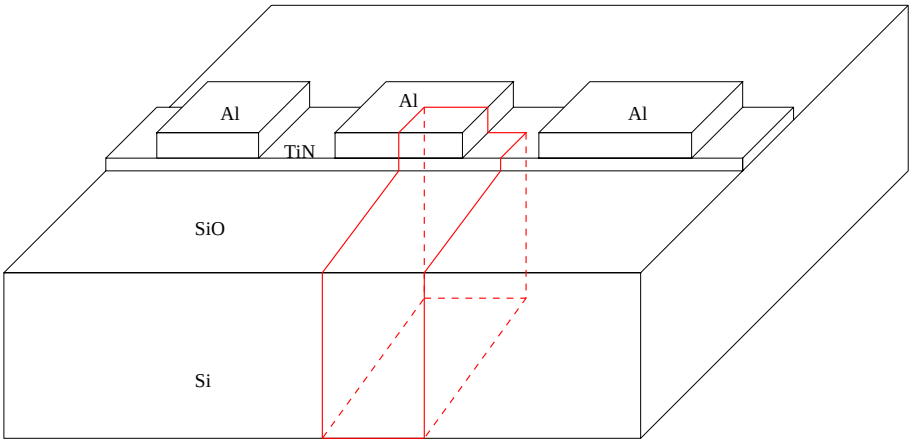

Figure 4.22: Schematic illustration of a typical test sample. Due to the symmetry only a quarter of the Al segment was modelled as marked by the red line.

Fig. 4.23 shows the finite element model containing a quarter of a 800nm thick Al segment on a 245nm thick TiN stripe on 200nm SiO_2 on a 0.67mm thick and 2mm wide Si substrate. The Al segment length was set to the critical length of 7 μm determined from the experiment. The width of the Al segment and TiN stripe was 8.6 μm, the spaces between the Al segments were 3 μm and the applied current was 80mA (which corresponds to a current density of roughly 1MA/cm^2 in the Al segment). The material properties were the same as for the 2D thermal finite element model. At all model faces other than the bottom face, adiabatic boundary conditions were applied. A homogeneous current density was applied to the TiN stripe and the nodes at the other end of the TiN stripe and Al were set to zero volts. By calculating the temperature increase without Al on top of the TiN stripe it was verified that the values obtained for the 3D electric-thermal coupled finite element model were the same as for the 2D thermal model, as expected.

The results for the current density, temperature increase, and temperature gradients are shown in Figs. 4.24 - 4.26. Fig. 4.24 shows that the current density in the Al segment is homogeneous (roughly 1MA/cm^2), as expected.

Fig. 4.25 shows the modelled temperature in an electromigration test structure due to Joule heating. The highest temperature of 281°C occurs in the TiN

stripe, as expected. In the Al segment the temperature ranges from 280 °C at the end of the segment to 277 °C in the middle of the segment. The average temperature in the Al segment is therefore roughly 50 degrees higher than the temperature of the hotplate. This temperature increase is much lower than in a continuous TiN stripe where a current density of 1MA/cm^2 caused a temperature increase of roughly 115 °C.

Fig. 4.26 shows that temperature gradients up to almost 5 °C/μm are generated at the edge of the Al segment. These gradients can cause a mass flux due to thermomigration according to the following equation [53]

$$J_{th} = -\frac{D}{\Omega\ k\ T}\ \frac{Q^*}{T}\ \frac{\delta T}{\delta x}\ , \tag{4.3}$$

where Q^* is the heat of transport. For Al, Q^* is roughly -7 kJ/mol [53], where the negative sign means that the atoms move from the cold to the hot regions. For the calculated temperature gradients of 5 °C/μm the above equation predicts significant material transport due to thermomigration however, experimental investigations of 800nm thick Al segments, that were shorter than the critical length and had been stressed for a few days at 1MA/cm^2, did neither show damage at the cathode nor at the anode end of a segment and therefore the effect of thermomigration was not considered further.

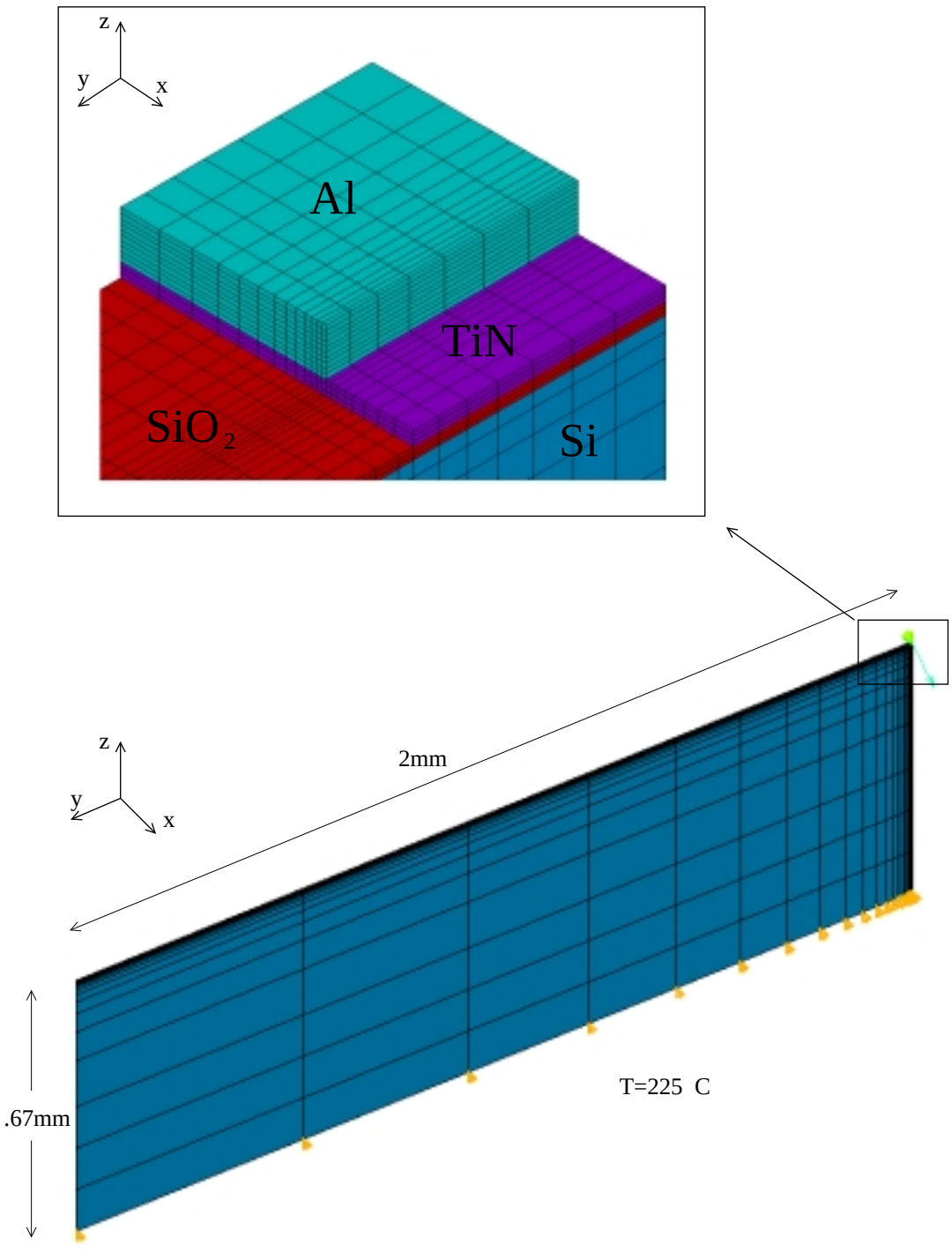

Figure 4.23: 3D electric-thermal finite element model of the test sample.

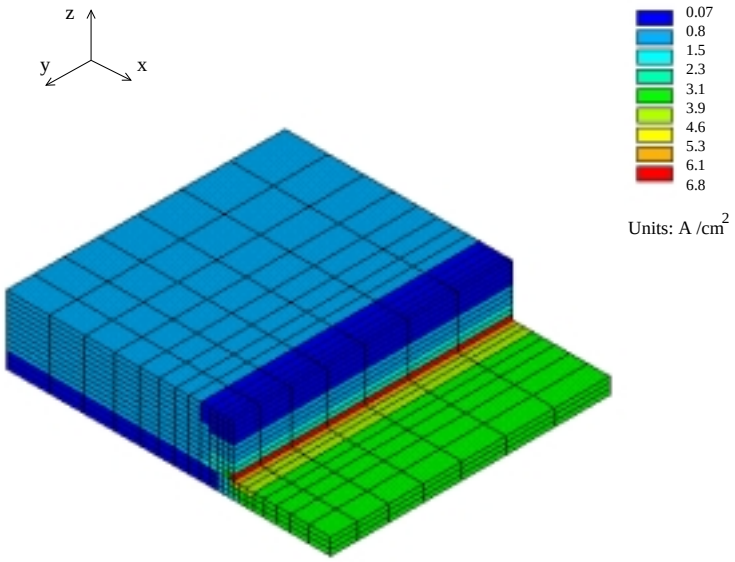

Figure 4.24: Current density distribution in an 800nm thick Al segment on a TiN stripe at an applied current of 80mA. Current crowding, where the current enters the Al from the TiN leads to a factor six increase in local current density.

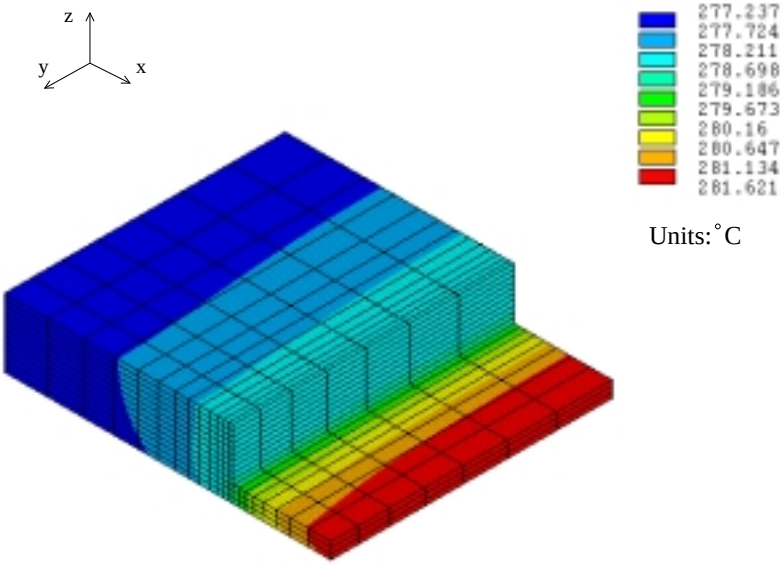

Figure 4.25: Temperature distribution in an 800nm thick Al segment on a TiN stripe at an applied current of 80mA. The temperature in the Al segment is roughly 277 °C which is around 50 °C higher than the temperature of the hotplate (225 °C).

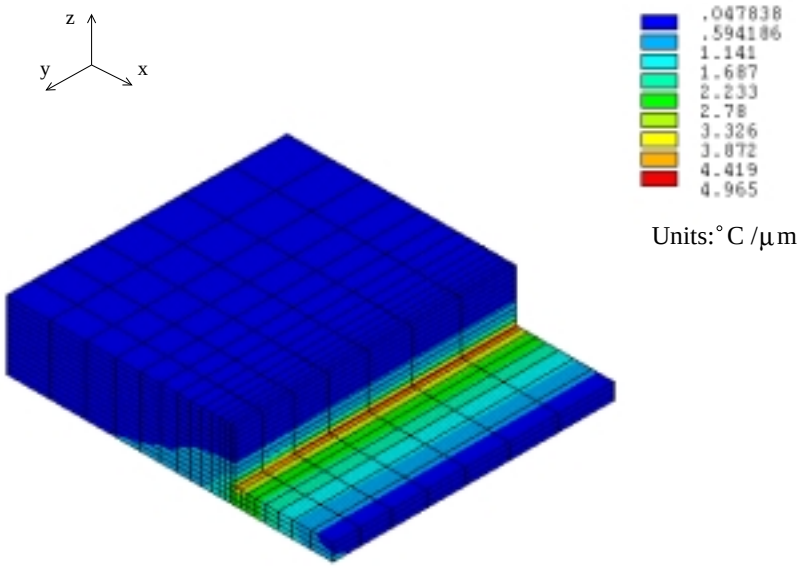

Figure 4.26: Temperature gradients in an 800nm thick Al segment on a TiN stripe at an applied current of 80mA. Temperature gradients as large as 5 °C/μm occur at the end of the Al segment, where the current enters the Al from the TiN.

4.3 The Critical Product

In this section, measurements of the critical product in the electromigration samples are presented. It was first verified that the critical product is in fact constant for various current densities, then the influence of film thickness, temperature, annealing history and native oxide on the critical product were investigated.

In what follows, the current applied was picked such that the current density of in 10 μm wide Al segments was 1MA/cm^2 ignoring the TiN. In fact, due to small variations in segment width and due to the TiN, the actual current density varied by roughly $\pm 10\%$ (the actual current densities and segment widths are listed in Appendix B). Assuming that the Al and TiN act as parallel resistors the current in the Al is given by the following expression:

$$I_{Al} = \frac{I_{total}}{1 + \frac{\rho_{Al}\ h_{TiN}}{\rho_{TiN}\ h_{Al}}}, \tag{4.4}$$

where h is the film thickness. For example, in a 100nm thick test sample 87 % of the total current passes through the Al, whereas in a 800nm thick test sample 98 % passes through the Al (using $\rho_{\mathrm{Al}} = 3 \cdot 10^{-8}\Omega$m, $\rho_{\mathrm{TiN}} = 50 \cdot 10^{-8}\Omega$m and $h_{TiN} = 245$nm).

4.3.1 Influence of Current Density

The experiment was performed with the in-situ probe station in the SEM at a testing temperature of 225°C using 200nm thick Al segments. The samples were annealed at 400°C for 1 hour in air before testing. The critical lengths were determined by taking the arithmetic mean of the longest segment that showed no drift and the shortest segment that drifted. Since the difference in length of two adjacent segments is 2 μm, this leads to an uncertainty of $\pm 1\mu$m in the critical length at a given current density.

The critical length was first measured at a low current. Then the current density was increased and the critical length was measured again in the same sample. This process was continued until all segments in the test sample had drifted. There is some scatter in the value of the critical product as a function of current density which may come from deviations in the critical product itself

(presumably due to variations in microstructure) or just from the fact that the time waited for onset of damage formation was not long enough. The results are shown in Fig. 4.27. A best fit leads to a critical product of $\beta = 1342 \pm 20$A/cm for this test sample, which falls in the range of what is reported in the literature (see Fig. 2.3).

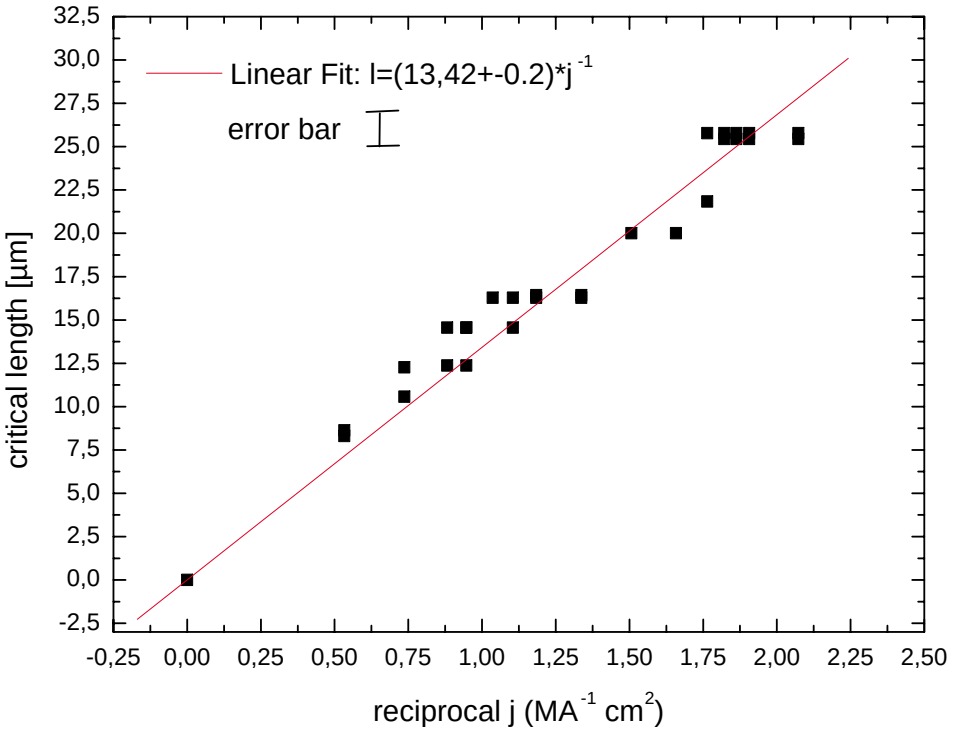

Figure 4.27: Critical length as a function of reciprocal current density in a 200nm thick test sample. A linear fit ($l = (13.42 \pm 0.2) \cdot j^{-1}$) through these data leads to a critical product of 1342 $\pm$ 20 A/cm.

4.3.2 Influence of Film Thickness

As described in Chapter 2, the yield stress of a material is expected to be related to the critical product. Therefore, the film thickness should show an effect on the critical product, because the yield stress of thin films is predicted to be proportional to the inverse film thickness [51] and inverse grain size [54]. Such a relation between the yield stress and the film thickness and the grain size has also been experimentally observed in [47].

The critical product was determined as a function of film thickness for 100, 200, 400, 600 and 800nm thick Al samples. Several test samples of each film thickness were measured to check for reproducibility and to obtain information about the scatter (6 samples of the 100nm thick films, 5 samples of the 200nm thick films, 8 samples of the 400nm thick films, 5 samples of the 600nm thick films and 5 samples of the 800nm thick films were investigated). The values obtained from the two arms of one test sample were averaged to get an average critical product for one test sample. The experiment was carried out with the ex-situ probe station at a testing temperature of 225 °C. All samples were annealed at 400 °C in air for one hour before testing.

Figures 4.28 - 4.30 show FIB pictures of the 100, 600 and 800nm thick samples tested at a current density of 1MA/cm^2 at 225°C. In the thicker test samples more segments are damaged, indicating that the critical product decreases with increasing film thickness.

This is also shown in Fig. 4.31 where the critical products are plotted as a function of film thickness. The circular data point for the 200nm thick sample is the measurement from the previous section. The error bar of ±100A/cm in the critical products is due to the uncertainty of ±1μm in the critical length. There is also considerable scatter in the measurements at a given film thickness. The values of the critical product for each film thickness were averaged and are plotted in Fig. 4.32. The error bars represent the standard deviation. The average critical product decreases almost linearly from 1540 A/cm to 1000 A/cm with increasing film thickness from 100 to 800nm.

All data points for a given film thickness were obtained from test samples on the same chip. Therefore, the test samples had been annealed for different

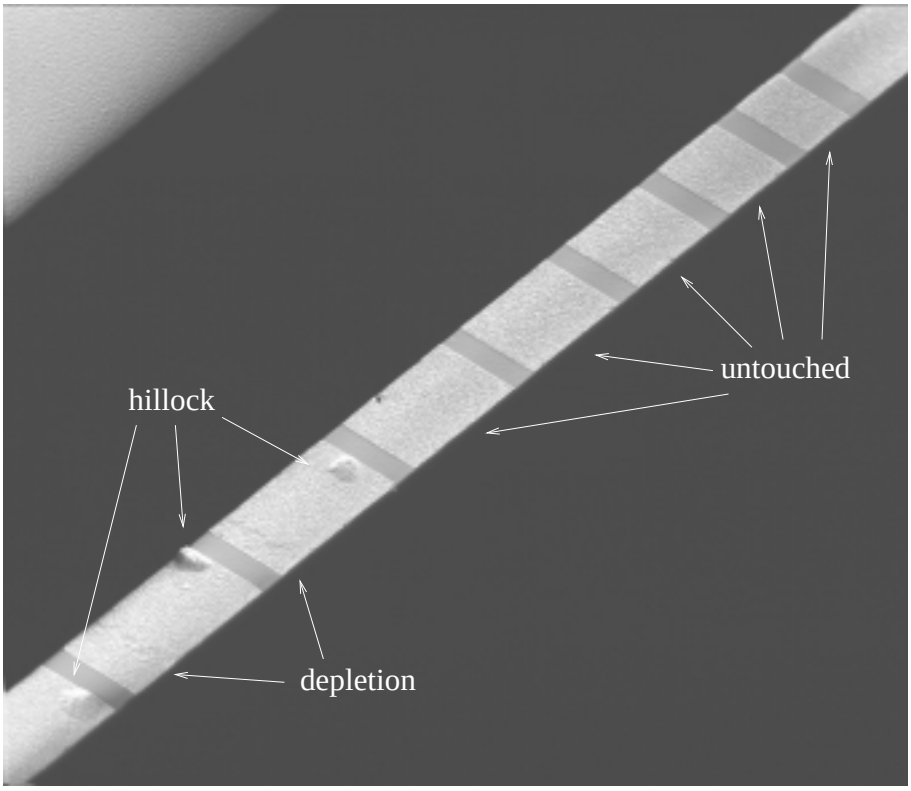

Figure 4.28: FIB picture of a typical electromigration test sample showing the critical product for 100nm thick and 10μm wide Al segments on a TiN stripe tested at a current density of 1MA/cm^2 at 225°C.

times at the testing temperature of 225°C before the were actually tested. The measured critical products were examined to see if the accumulated annealing time might influence the critical product, but no trend with annealing time was observed.

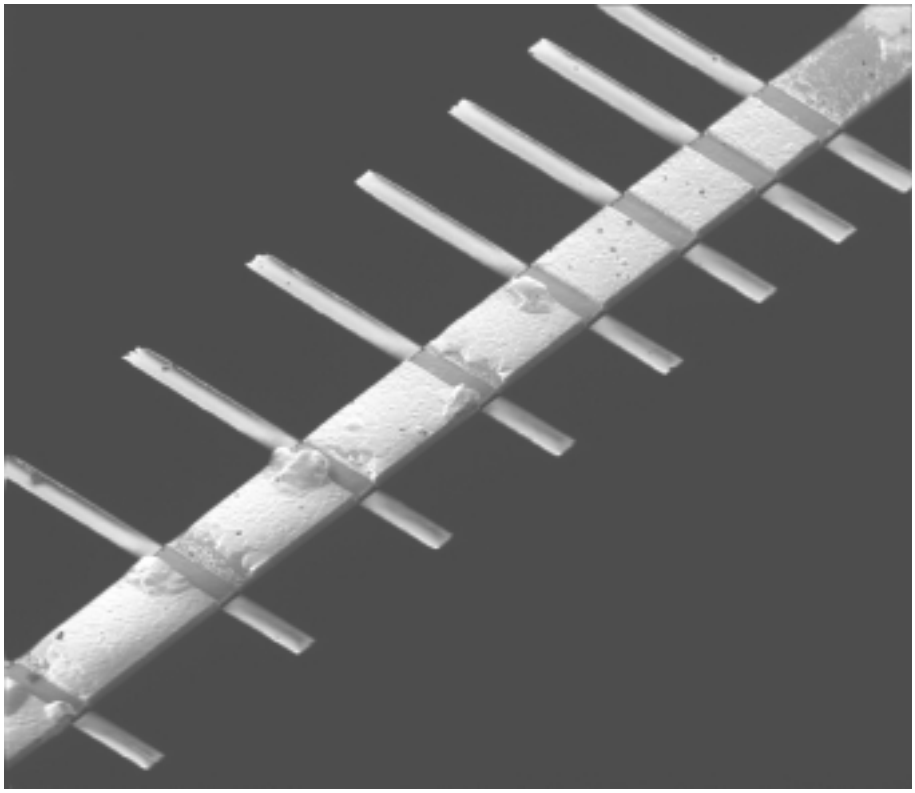

Figure 4.29: Same as in Fig. 4.28 for 600nm thick Al segments.

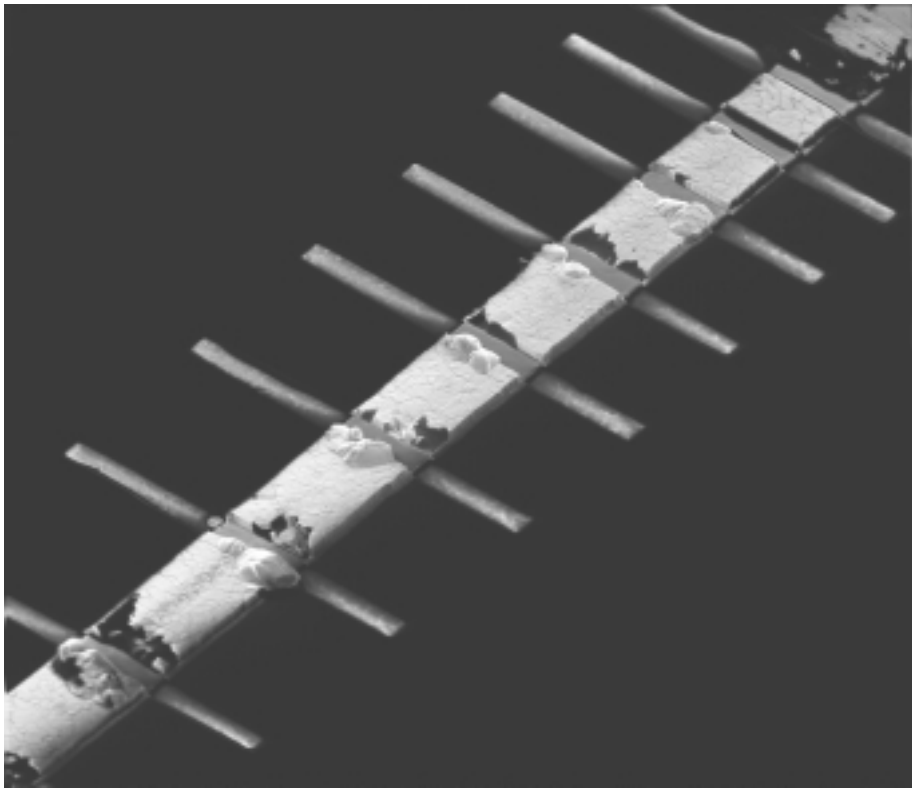

Figure 4.30: Same as in Fig. 4.28 for 800nm thick Al segments.

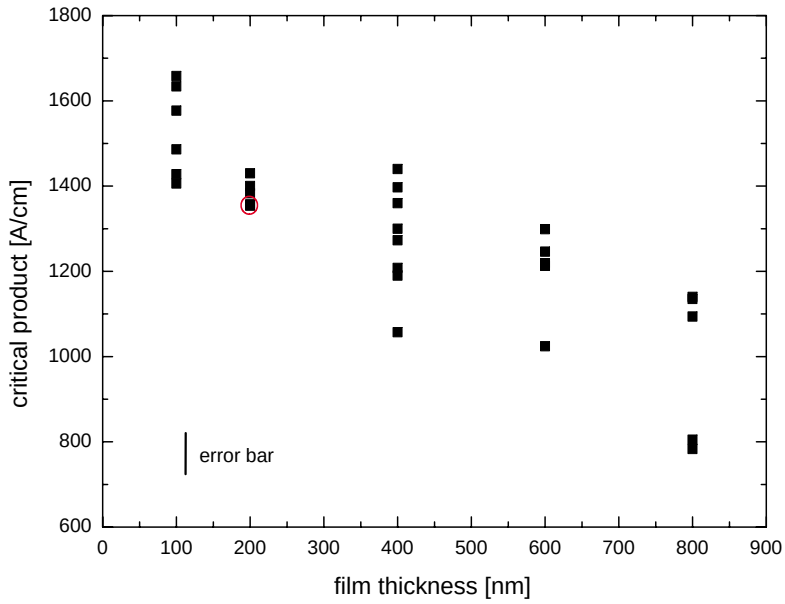

Figure 4.31: Critical products for different film thicknesses measured at a testing temperature of 225 °C and at a current density of 1 MA/cm^2.

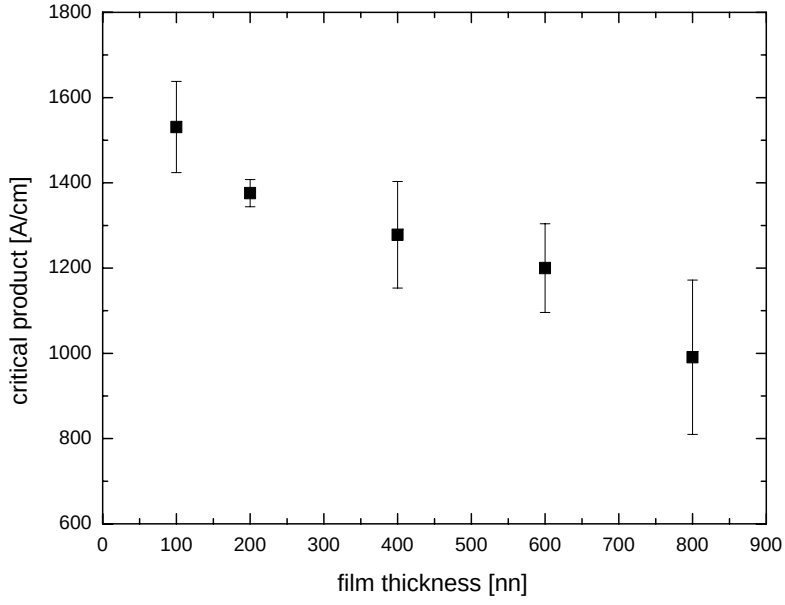

Figure 4.32: Averaged critical products for different film thicknesses measured at 225 °C and at a current density of 1 MA/cm^2.

4.3.3 Influence of Temperature

The temperature dependence of the critical product has been measured by several authors and led to different results ranging from a strong decrease with increasing temperature [12] to almost independent of temperature [55], [7]. However, an increase with temperature has never been observed. As explained in Chapter 2 , the temperature dependence of the critical product should essentially follow the temperature dependence of the threshold stress and therefore it can help to identify the physical mechanisms for the threshold stress and also help to estimate if Joule heating was important in the film thickness experiment reported in the last section.

The critical product was measured as a function of temperature for the 200, 400 and 600nm thick Al test sample at a current density of approximately $1MA/cm^2$. The experiment was performed with the ex-situ probe station and all samples were annealed at 400 °C in air for one hour before testing.

The measurement of the critical product as a function of temperature was performed using the following procedure: First, the critical product was determined at a temperature of 225 °C, then, the temperature was increased to 275 °C and the critical product was measured again with the same sample and at the same current density. If no shorter segment showed damage, it was concluded that critical product was the same or higher than at 225 °C (indicated by the arrows in Fig. 4.33). Then, the temperature was subsequently increased to 325 °C and to 375 °C and it was checked again if any shorter segments were damaged. Using this method avoids scattering from different test samples, because always the same segment with the same microstructure is considered.

Fig. 4.33 shows that the critical product of the 200nm thick film is constant or increases in the temperature range from 225 to 375 °C. For the 400 and 600nm thick films the critical product decreases by an amount of roughly 200 A/cm in the range from 225 to 375 °C. A value for the 600nm thick at 375°C could not be obtained because one of the probe needles slid off the pad and destroyed the sample. The temperature dependence in all of the films is quite weak although it may increase some with film thickness. However, considering the uncertainty of ±100A/cm in the critical product, no attempt is made to interpret the effect.

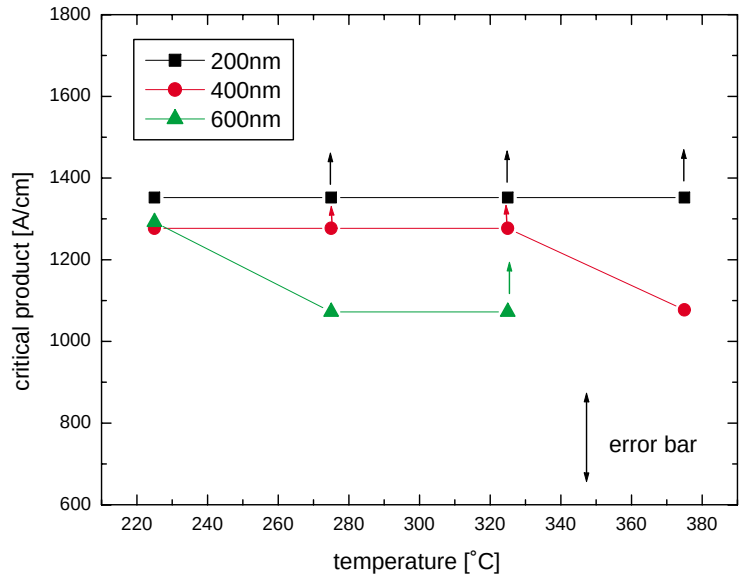

Figure 4.33: Critical product as a function of temperature for different film thicknesses at a current density of $1\mathrm{MA/cm^2}$.

4.3.4 Influence of Annealing Treatment

As reported in the section on film characterization, the annealing treatment changed the morphology of the Al/TiN interface and the thickness of the native oxide. To investigate whether these parameters influence the threshold stress, the critical product was measured for a 100 and 600nm thick Al film for three different heat treatments before testing.

Measurements of the critical product in samples in the as-deposited condition (deposition temperature $\approx$ 225°C), after annealing for 5 days at 225 °C, and after annealing for one hour at 400 °C were performed. Electromigration testing was performed at temperature of 225°C and at a current density of 1MA/cm^2 using the ex-situ probe station. The results are shown in Fig. 4.34. Annealing the

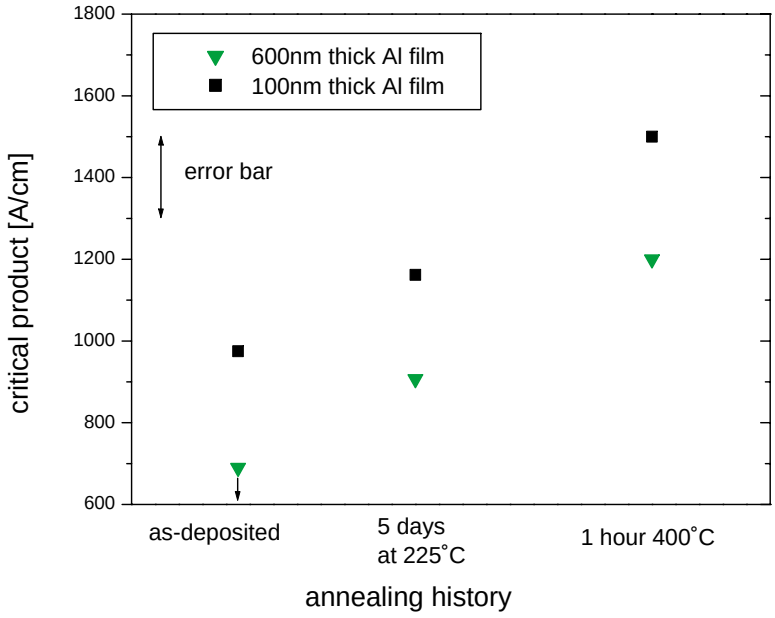

Figure 4.34: Critical product for 100 and 600nm thick Al film as a function of annealing history, tested at a temperature of 225°C and a current density of 1MA/cm^2.

samples for one hour at 400 °C in air leads to increase in critical product of 54

% for the 100nm thick film and an increase of at least 74 % for the 600nm thick film compared to the as-deposited values. In the case of the as-deposited 600nm thick Al film, all segments of the test sample were damaged at a current density of 1MA/cm^2. Therefore, it was only possible to determine an upper limit for the critical product of 690 A/cm (indicated by the arrow in Fig. 4.34).

To identify whether the increase in critical product after annealing is due to an increase in native oxide thickness or due to the morphology change of the Al/TiN interface, several attempts were made to vary these parameters independently. In one experiment, a 600nm thick Al sample was annealed for one hour at 400 °C in a vacuum system (total pressure of $9 * 10^{-7}$mbar), in an attempt to anneal the film without growing the oxide. However, a subsequent SIMS depth profile of oxygen (Fig. 4.35) showed almost no difference in oxide thickness between air and vacuum-annealed samples confirming that the native oxide forms even at very low oxygen partial pressures. The measured critical product was also the same for the vacuum and air annealed sample.

Since the vacuum annealing experiment did not lead to a controlled variation in native oxide thickness, a different approach was tried: A 600nm thick Al sample was first annealed in air (1 hour at 400°C) and subsequently tested at 225°C at a current density of 1MA/cm^2 to determine the critical product. The native oxide of this sample was then removed by reactive ion etching (RIE) for 1 min (using the Al etch parameters listed in the experimental chapter) which led to material removal of around 50nm, as measured by a profilometer. The etched sample was subsequently tested again (at 225°C at a current density of 1MA/cm^2) to see if any shorter segments showed damage. Since this was not the case, it was concluded that the critical product was not decreased by the RIE step.

The surface of the sample before and after etching was analyzed by taking a mass spectrum and SIMS depth profiles of oxygen and chlorine as shown in Figs. 4.36 and 4.37. The mass spectrum of the etched sample (Fig. 4.36) shows strong oxygen and chlorine peaks and a few other peaks due to surface contaminants which vanish as the surface is sputtered away. The mass spectrum of an unetched sample is identical except that no chlorine peaks are present. The chlorine on the etched sample surface is presumably due to the etch gas $SiCl_4$ used in the RIE process.

The SIMS depth profiles (Fig. 4.37) for the etched sample show that the chlorine signal decreases quickly with sputter time while the oxygen signal in-

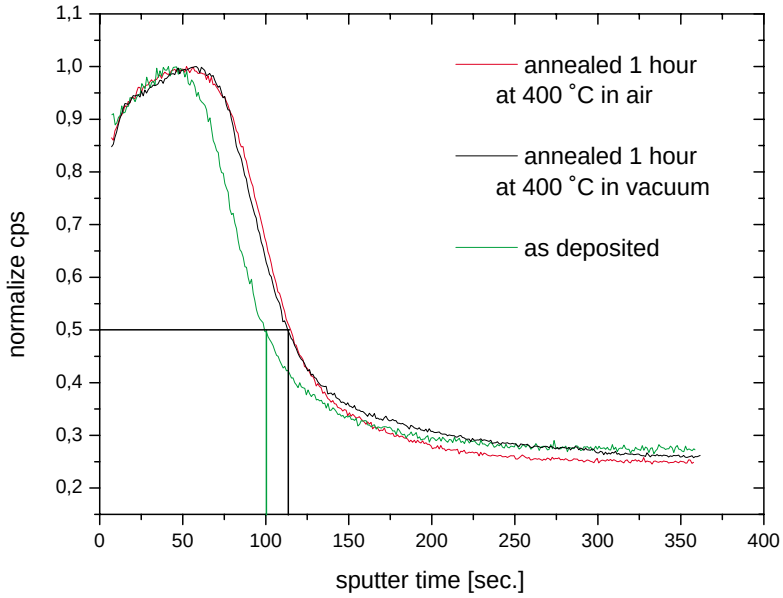

Figure 4.35: SIMS depth profile of oxygen for the as-deposited, air annealed and vacuum annealed sample.

creases strongly. This indicates that the chlorine is only near the surface of the etched sample. The width of the oxygen peak of the etched sample is smaller than for the annealed unetched sample, also shown in Fig. 4.37. However, both oxygen peaks extend to approximately the same depth into the sample. A simple interpretation of these results would be that the etched sample has a native oxide of comparable thickness to that of an unetched sample and that the near surface region contains chlorine which may interact with oxygen ions and reduce the oxygen count rate. However, this is not at all what is expected after an etch process that presumably removed 50nm of surface material, indicating that the etch process and possible subsequent oxide formation, are more complicated than expected. It is therefore not possible to determine from the SIMS data whether the native oxide of the etched sample is really thinner than for the unetched sample and a direct comparison between oxide thickness and critical product was also not possible by this method.

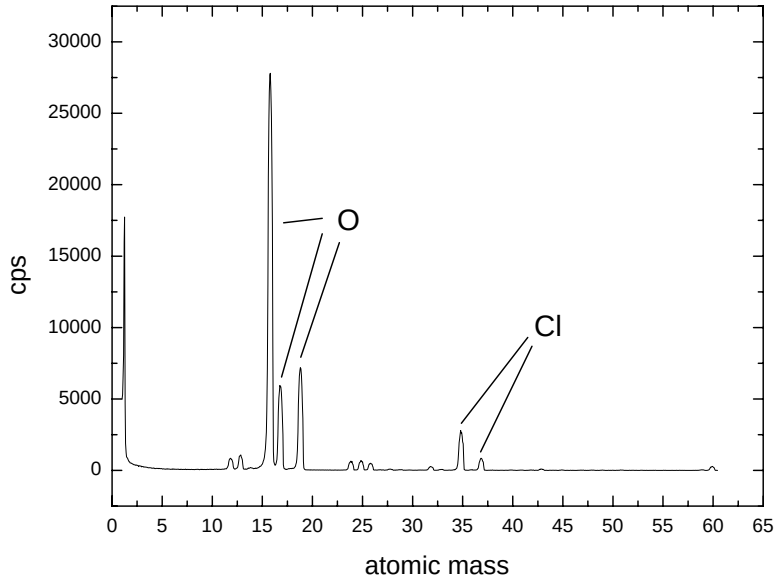

Figure 4.36: Mass spectrum of the etched Al surface.

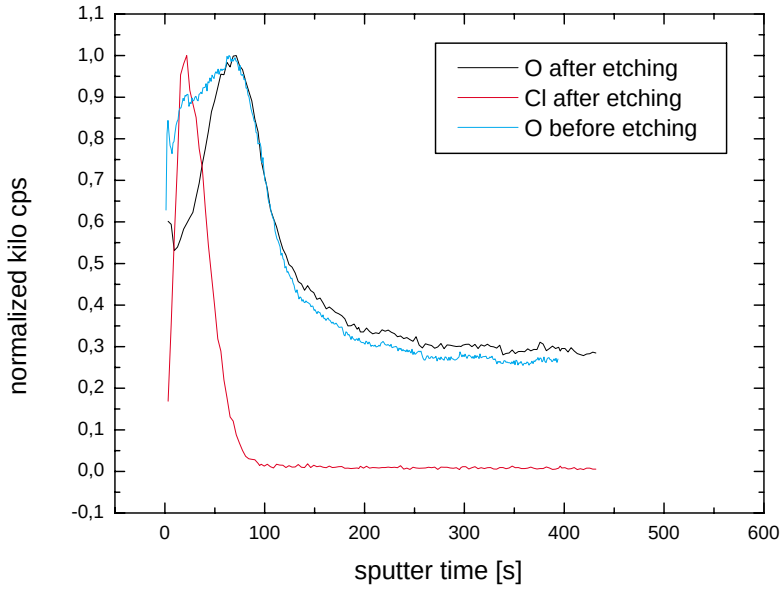

Figure 4.37: SIMS depth profile of oxygen and chlorine for the etched and unetched Al surface.

4.3.5 Influence of Externally Applied Stress

Since the critical product is associated with a certain threshold stress, it was investigated whether the addition of an externally applied stress influences the measured critical product.

In a first experiment, an external mechanical stress was applied to the test samples during electromigration testing using a four point bending apparatus as described in Chapter 3, resulting in approximately uniaxial stresses of 50 MPa tension or compression. Due to the design of the test samples (see Fig. 3.2) the stress was applied parallel to one arm and perpendicular to the other arm of the test structure at the same time. However, for all cases (tensile and compressive stresses, parallel and perpendicular to the stripes) the critical product as determined at 225 °C and 1MA/cm^2 remained the same within the scatter.

In a second experiment, tensile and compressive biaxial thermal stresses were applied to the test samples by thermal cycling as demonstrated by the wafer curvature stress measurement in Fig. 4.12. The sample was first heated up to 225 °C and the critical product was measured, then the sample was heated up to 400 °C and cooled down to 225 °C and the critical product was again measured. According to Fig. 4.12, this thermal treatment should lead to a stress difference in a film of around 150 MPa at 225 °C on heating and cooling. The structures used for electromigration testing consisted of 10 μm wide polycrystalline Al segments and were therefore assumed to behave similar to a film. However, both measurements yielded the same critical product indicating that it is not influenced by an initial biaxial stress difference of around 150 MPa.

4.4 Observations of Damage Formation

Important insights into the damage formation process during electromigration, and therefore the mechanism for the threshold stress, can be obtained from post-mortem studies of electromigration-induced damage morphology. For investigating the damage morphology the FIB microscope is particular useful, because the quality of the images at corners and edges of a sample is much better than in a SEM where the contrast is usually too strong to get a good picture. In addition, with the FIB is was possible to determine the grain structure of the damage sites (due to the channeling contrast of the ions) by either cross-sectioning or just scanning and imaging the sample. The damage formation was investigated for different film thicknesses from 100 to 800nm. Larger hillocks are observed in the thicker films and more uniform depletion in thinner films. Otherwise no obvious trends with film thickness were found.

Fig. 4.38 shows typical electromigration damage of an Al segment after testing. Material has been depleted fairly uniformly from the cathode end and has accumulated at the anode end of the segment in a single hillock. The hillock surface shows often small steps (indicated by the arrow in Fig. 4.39) which might be caused by local plastic deformation. The depletion of the cathode end is often "terraced", suggesting that thinning takes not place homogeneously at the whole cathode end but locally at different grains. Fig. 4.40 shows a FIB cross section of the cathode end of a segment, where this "terraced" depletion seems to correlate with the grain structure.

Figs. 4.41 and 4.42 show FIB images of an electromigration-induced hillock at the anode end of a 600nm thick Al segment, tilted at an angle of 45 ° for two different magnifications. The sample had been tested at a constant current density of 1 MA/cm^2 at successive testing temperatures of 225, 275 and 325°C. The original Al film material is visible on top of the hillock as a curved dark layer (indicated by the arrow) which has been pushed up by the accumulation of material under the original Al film. The dark contrast is due to polymer sidewalls [1] which usually form at the edges of the Al segments if photoresist is used as a mask during reactive ion etching. Below the dark layer, three areas of different contrast are visible, separated by two inclined straight lines, which correspond to the material added at the three different testing temperatures (samples which

[1] These polymer sidewalls are insulating and therefore they lead to a dark contrast in the FIB picture.

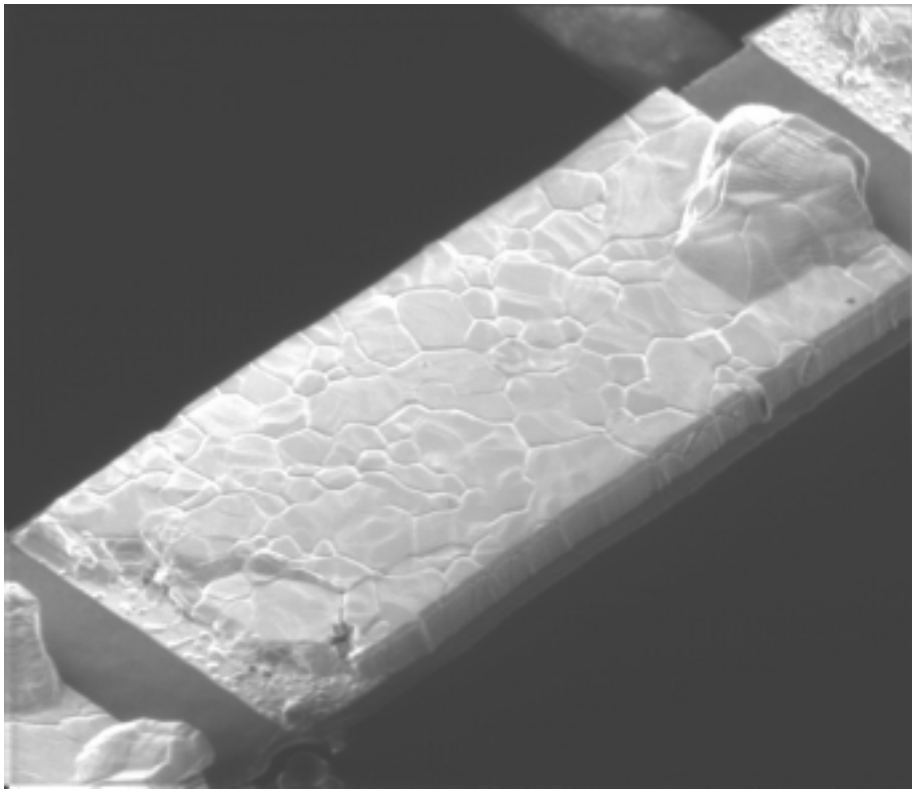

Figure 4.38: FIB picture of a electromigration damage of an 800nm thick Al segment.

were tested at a single temperature do not show this contrast). The fact that the lines are straight indicates that Al atoms were added to the hillock at the Al/TiN interface and not at the original interface, which has now moved up, because in this case the lines would be curved. The idea that hillock growth occurs by the addition of material at the Al/TiN interface is supported by FIB cross sections which often reveal small particles, which have formed at the original Al/TiN interface (as also observed by cross-sectional TEM in Fig. 4.7) and have now been lifted up due to material accumulation at the interface. This is shown in Fig. 4.43. The first and last precipitate at the border of the hillock are still located at the interface whereas the precipitates in the hillock have been lifted up. They are arranged in a straight line which is inclined to the TiN layer (similar to the straight line observed in Figs. 4.41 and 4.42) showing how the hillock has grown during electromigration (further example Fig. 4.46). Similar particles have

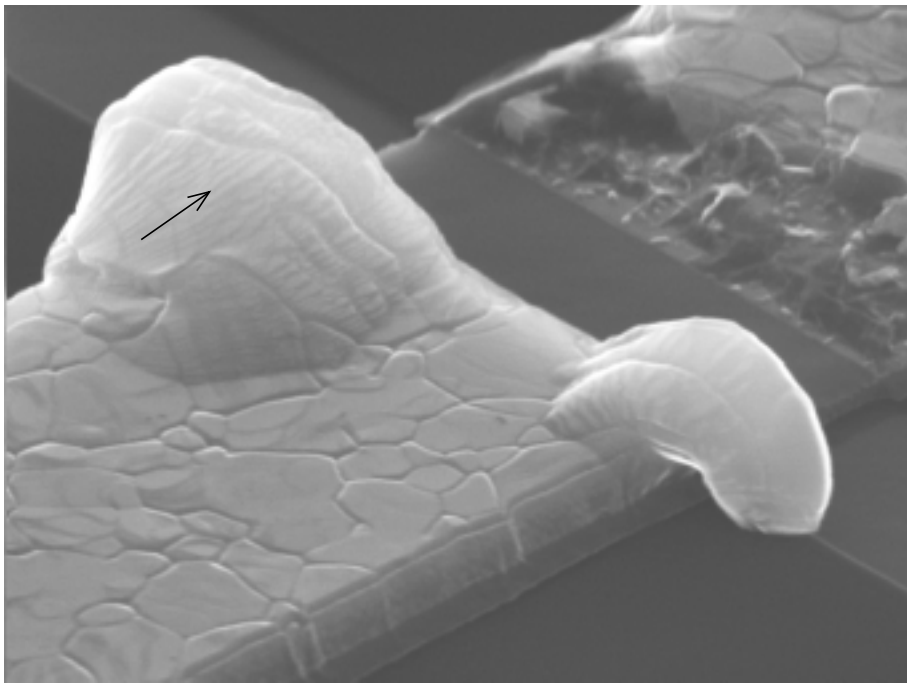

Figure 4.39: FIB picture showing small steps in the surface of a hillock.

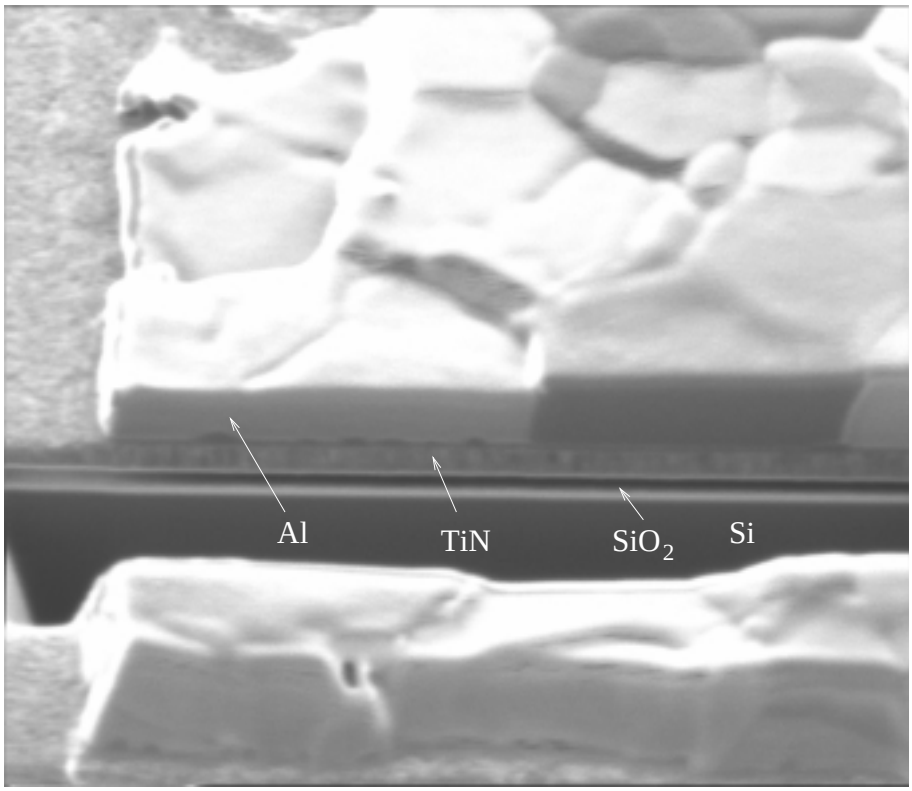

Figure 4.40: FIB cross section of the cathode end of a segment showing depletion.

also been found by other authors in hillocks of passivated pure Al lines and were identified to be $TiAl_3$ precipitates by a TEM diffraction pattern [45]. FIB cross sections of hillocks show also that the grain structure is columnar (Fig. 4.44). Thus the FIB observation of hillocks provide persuasive evidence that hillock growth proceeds by epitaxial growth from the Al/TiN interface.

FIB cross sections of small hillocks suggest that the atoms are initially added to a single grain, as shown in Figs. 4.45 and 4.46. For the subsequent growth of the hillock two cases were observed. First, the hillock extends to the neighboring grains and forms a multi-grain hillock such as shown in Fig. 4.44. Second, the hillock grows laterally with simultaneous grain boundary migration resulting in a hillock composed of a single grain, such as shown in Figs. 4.47 and 4.48. Fig. 4.47 shows a hillock where the location of the original grain boundary before testing is identified by the surface groove on top of the hillock. A cross section of this hillock in Fig. 4.48 reveals that the grain boundary has moved away from the groove to the border of the hillock. A similar example is shown in Figs. 4.49 and 4.50. The surface grooves on top of the hillock (Fig. 4.49) suggest a multi grain structure of the hillock but a cross section of this hillock reveals only a single grain (Fig. 4.50). It is likely that some grain growth occurs during the formation of multi grain hillocks since the typical grain size is often larger than the median grain size. For instance, the grain in the hillock in Fig. 4.44 is ten times larger than the median grain size in the film. For all of the investigated hillocks the border of the hillock coincided with grain boundaries. This is an important observation suggesting that the process of hillock growth is tightly connected with grain boundary migration.

In addition, EBSD investigations of tested structures revealed that hillocks grow preferred in non-(111) grains. An example is shown in Fig. 4.51 where the orientation of the grains that compose the hillocks are non-(111) whereas all other grains are (111). Due to the small grain size and the roughness of the surface clear backscattered patterns could not always be obtained from the sample which accounts for the many points that could not be assigned to a grain. Nonetheless, sufficient information was obtained to show that the majority of hillocks consist of grains with non-(111) texture whereas the majority of the grains in other regions of the segment are (111) oriented.

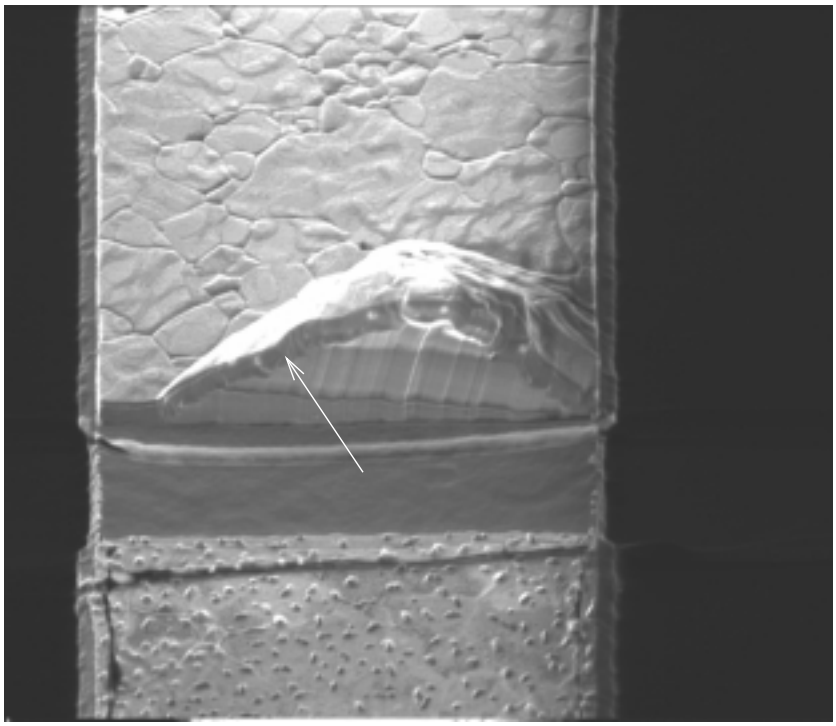

Figure 4.41: Hillock at the anode end of a 10 μm wide and 600nm thick Al segment. The original Al film has been pushed up due to material accumulation the Al/TiN interface and is visible on top of the hillock as a curved dark layer (indicated by the arrow).

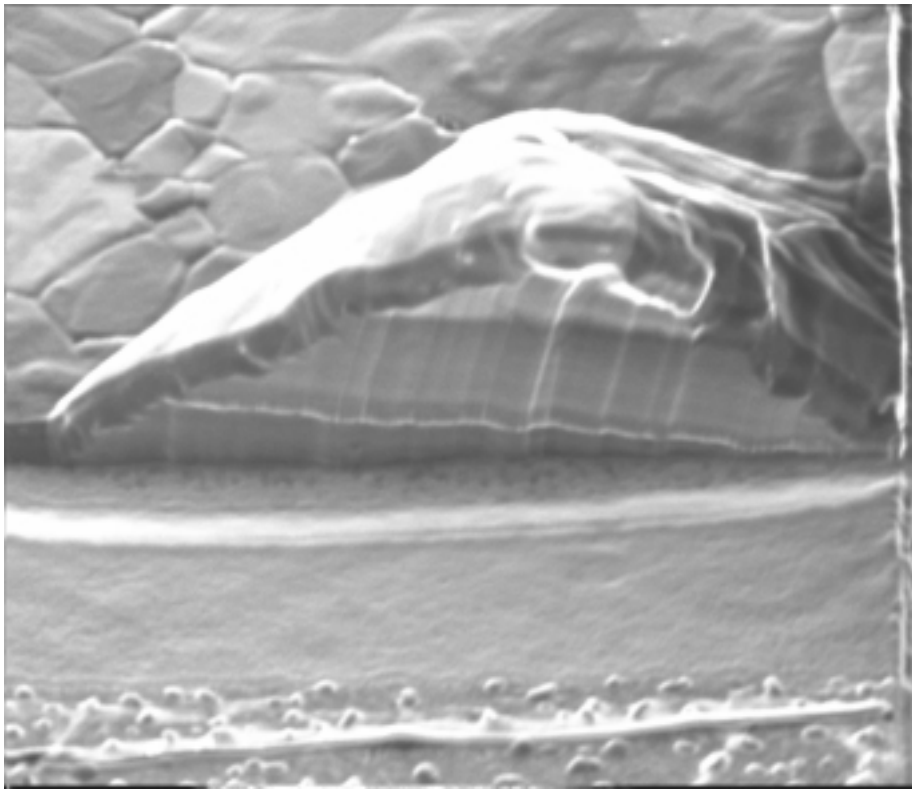

Figure 4.42: The same hillock as in Fig. 4.41 at a higher magnification.

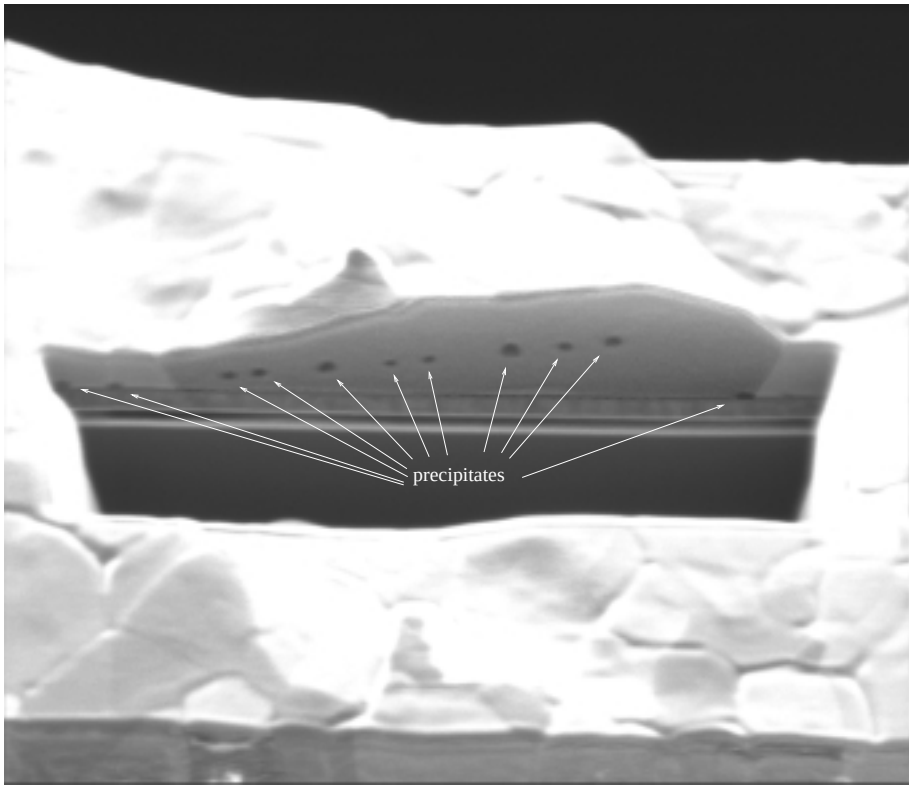

Figure 4.43: FIB cross section through a hillock showing precipitates which have originally formed at the interface and moved up due to material accumulation at the TiN/Al interface.

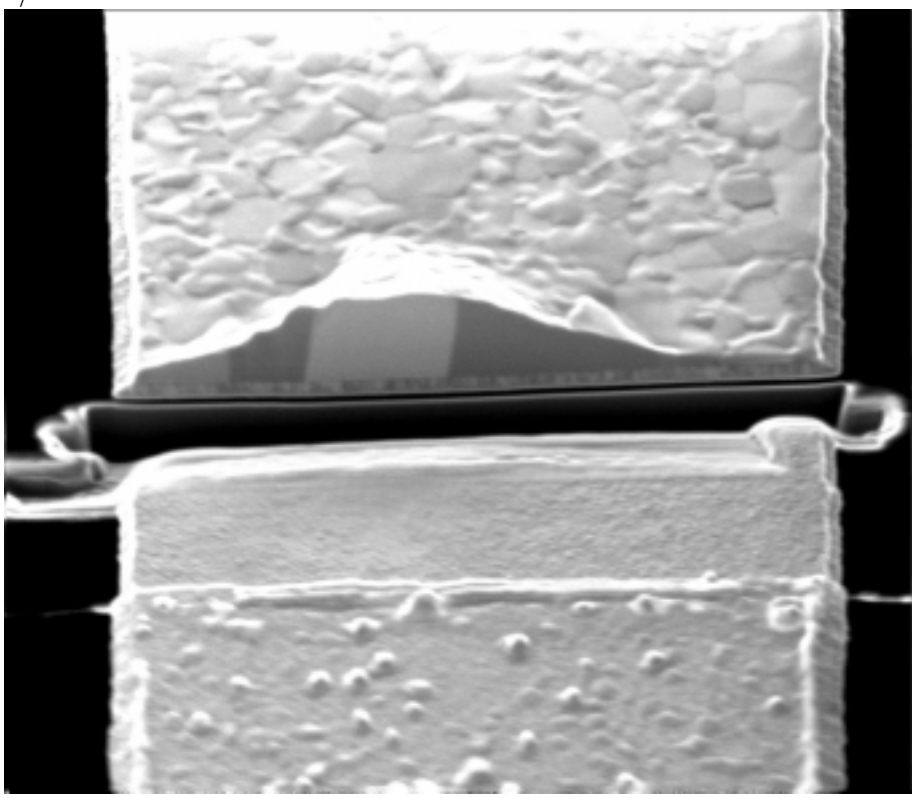

Figure 4.44: FIB cross section through a hillock showing columnar grains.

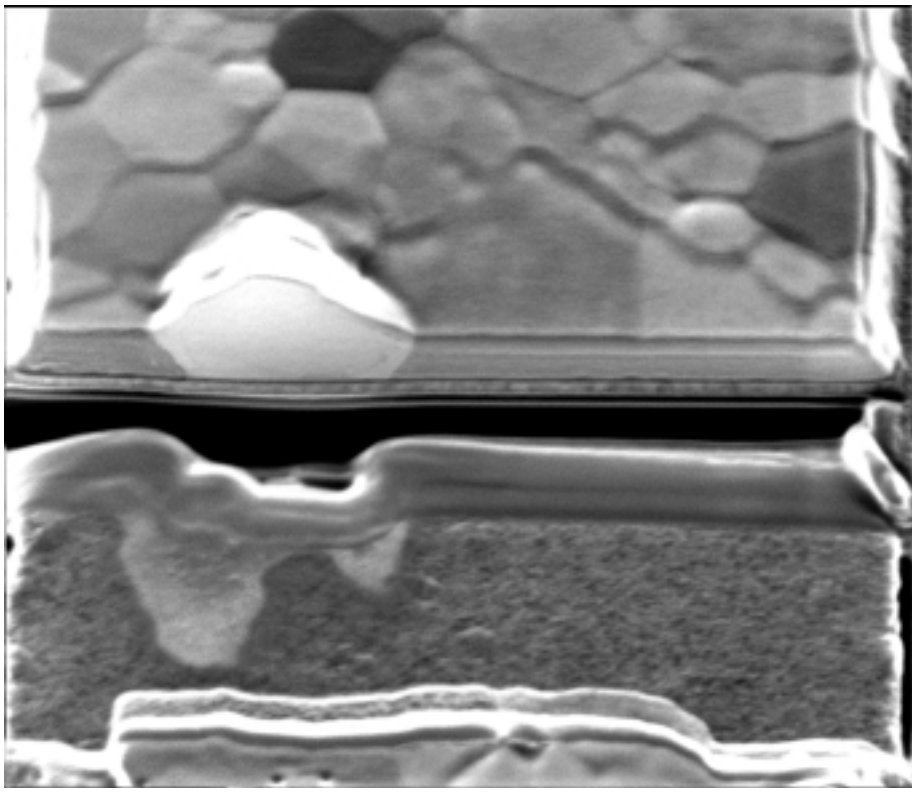

Figure 4.45: FIB observation of a single grain hillock.

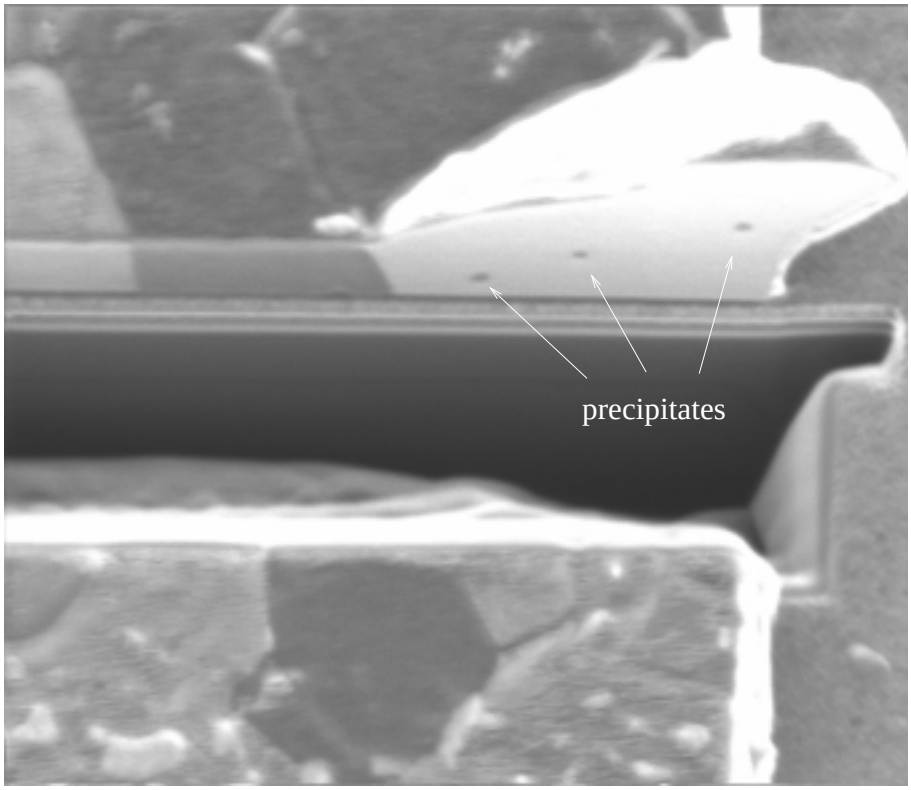

Figure 4.46: same as in Fig. 4.45.

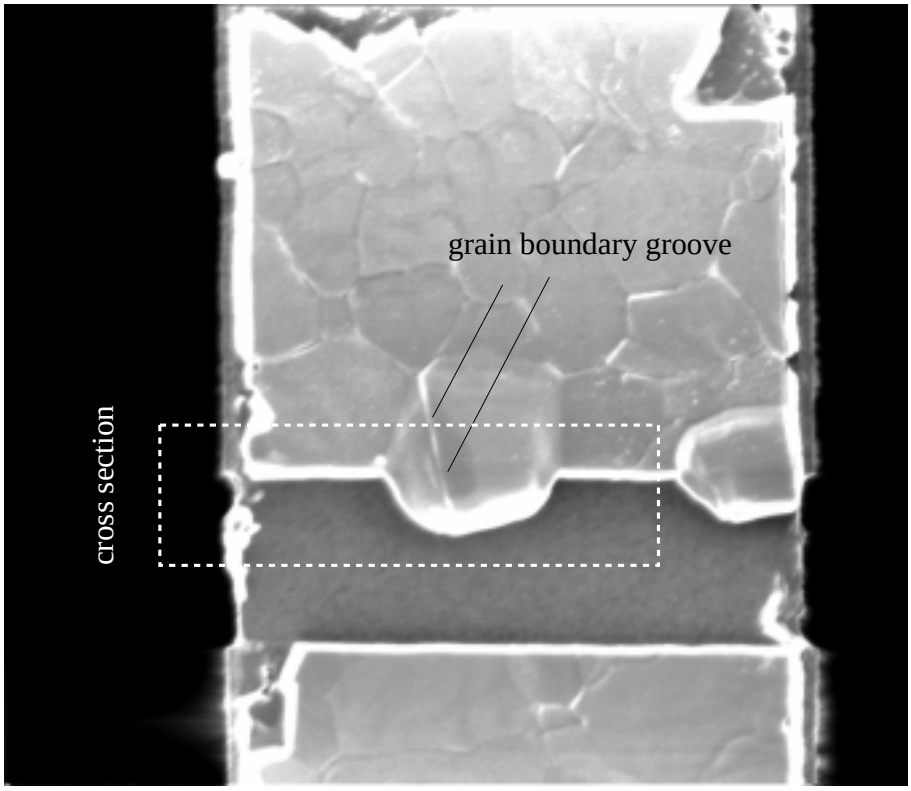

Figure 4.47: Hillock with surface grooves showing the original grain structure of the film.

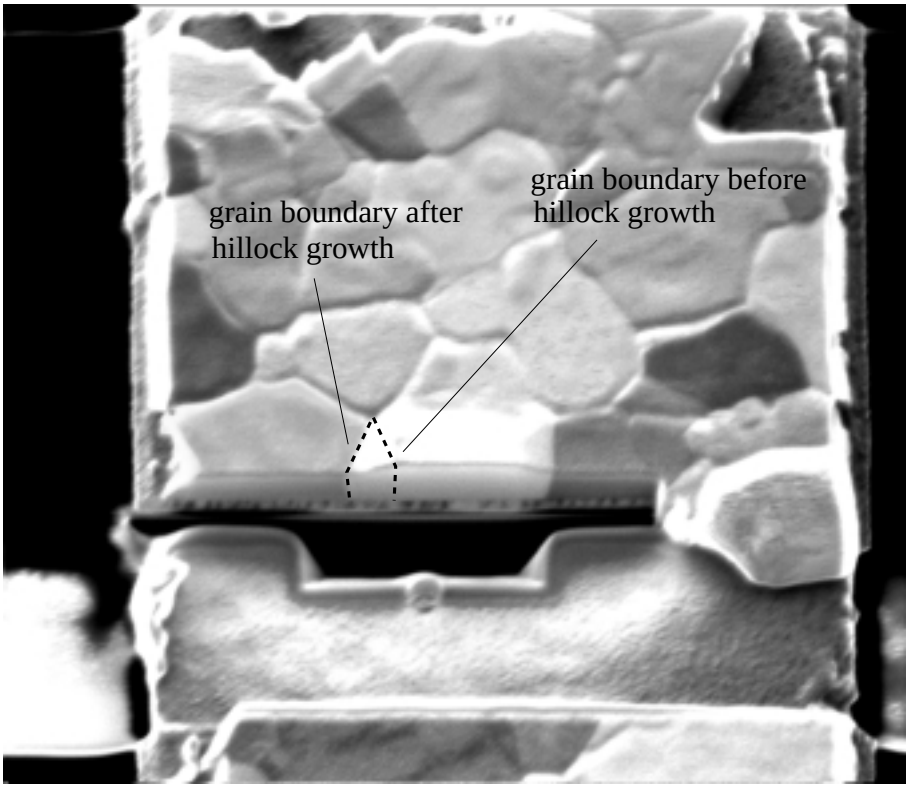

Figure 4.48: Cross section of the hillock from Fig. 4.47 showing that the grain structure in the hillock does not coincide with the surface grooves.

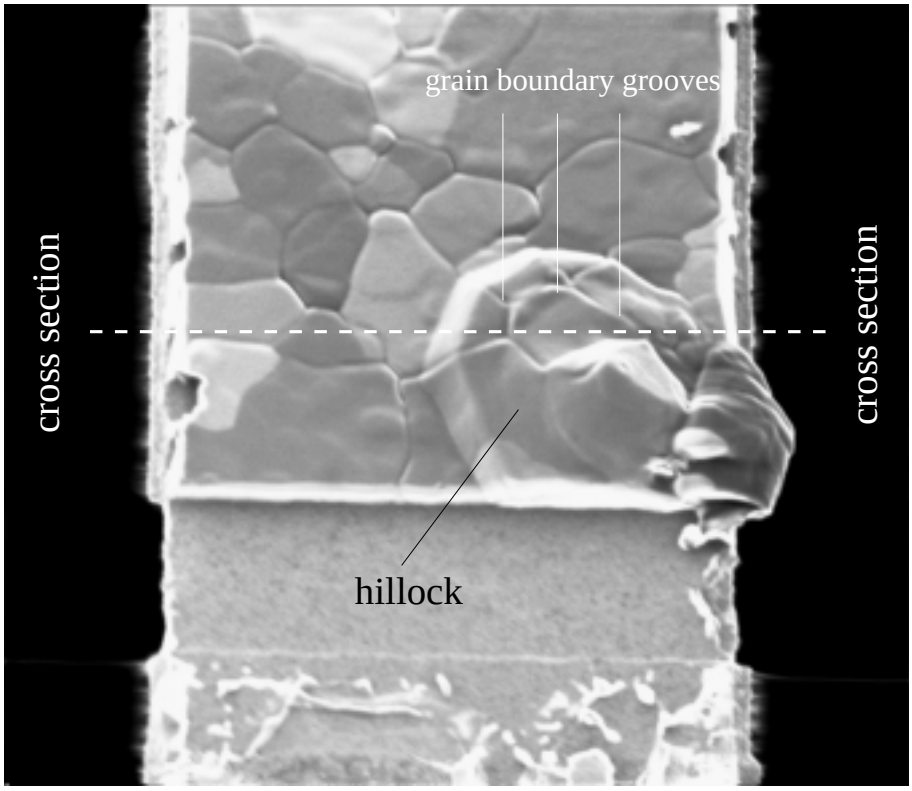

Figure 4.49: Hillock with surface grooves showing original grain structure of the film.

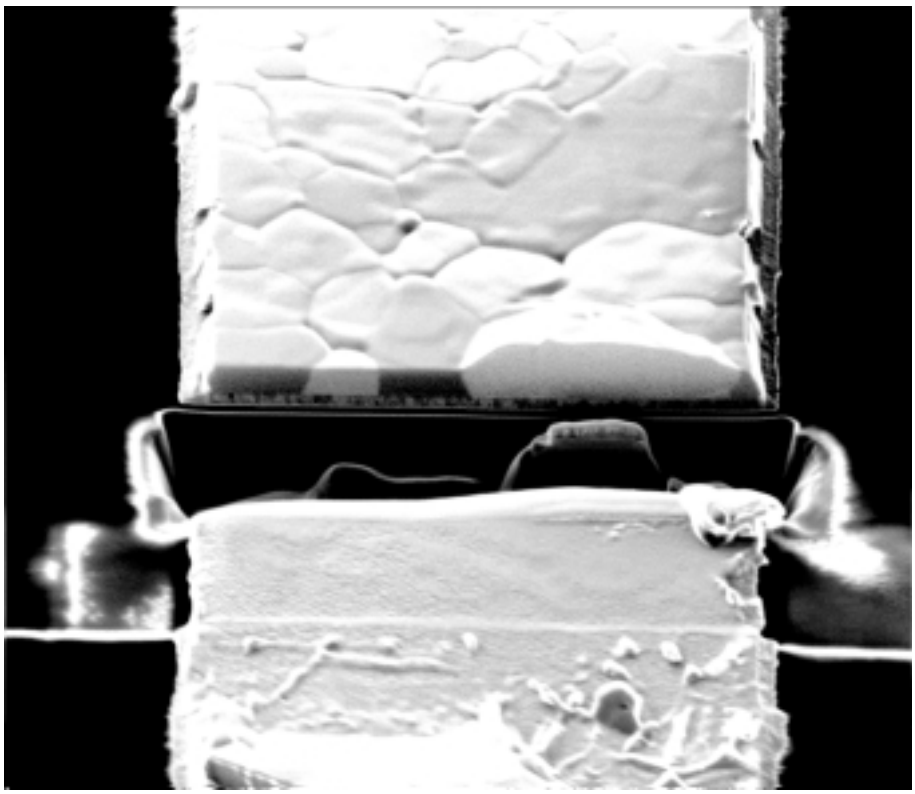

Figure 4.50: Cross section of the hillock from Fig. 4.49 showing that the grain structure in the hillock does not coincide with the surface grooves.

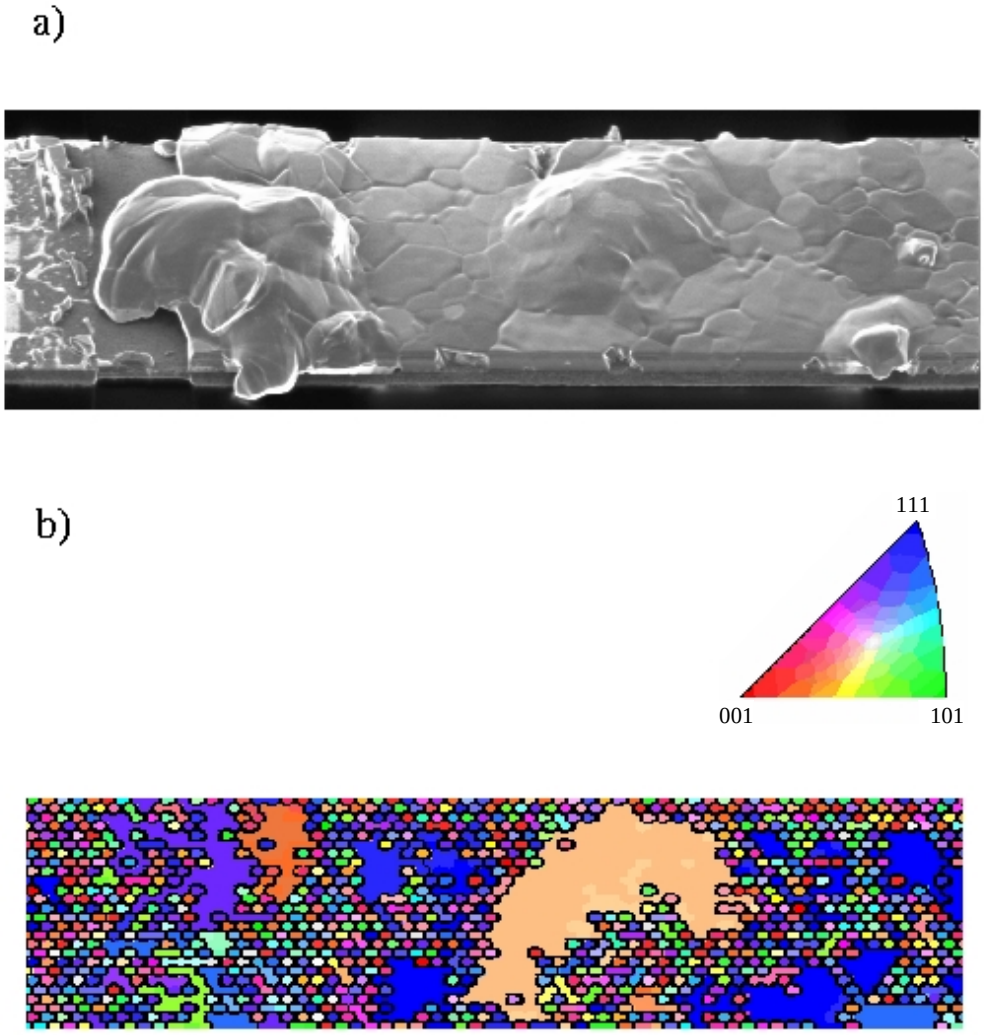

Figure 4.51: a) FIB image showing hillocks at the anode end of a 10 μm wide segment (tilted at 45 °). b) EBSD image of the same segment showing a non-(111) orientation of the hillocks (tilted at 70.5 °).

4.5 Summary of Results

The results of the film characterization and electromigration measurements are shortly summarized here and discussed in the next chapter.

4.5.1 Characterization Results

- The grain size was found to be on the order of the film thickness, except for the 800nm thick film where it was roughly twice the film thickness. The films did not show any grain growth during annealing at 400 °C for one hour in air, except the 800nm thick film.

- The films showed a (111) texture with a full width at half maximum (FWHM) of 5°. The texture did not change during annealing.

- The Al/TiN interface showed an increased roughness and $TiAl_3$ precipitates after annealing.

- The thickness of the native oxide increased after annealing from approximately 1.3nm to 1.8nm.

- The difference $\Delta\sigma_f$ of flow stress in tension and compression for the films showed values between 150 and 250 MPa. There was no trend with film thickness.

- The thermomechanical properties of the films did not change from the first to the second wafer curvature cycle.

4.5.2 Electromigration Results

- The temperature increase due to Joule heating was calculated to be 50 °C for the 800nm thick sample.

- The critical product decreases almost linearly from 1540 A/cm to 1000 A/cm with increasing film thickness from 100 to 800nm.

- The critical product is only very weakly temperature dependent in the range from 225 to 375°C. Therefore, Joule heating is not considered in the discussion of the electromigration results.
- Annealing of the films, either at 225 or 400°C increases the critical product strongly compared to the as-deposited condition.
- Externally applied uniaxial stresses of $\pm$ 50 MPa and thermal biaxial stresses of 150 MPa did not influence the critical product.
- Hillock growth proceeds by epitaxial addition of atoms to the Al/TiN interface, preferentially at non-(111) grains, and by grain boundary migration at the same time. Also, small steps are often observed on the hillock surface.

Chapter 5

Discussion

As a first approximation it is reasonable to assume that the electromigration threshold stress $\Delta\sigma_{th}$ is the same as the difference in compressive and tensile flow stress $\Delta\sigma_f$ of the film. However, a careful comparison of these two stresses in this chapter will show that they do not agree. Possible reasons for the disagreement are discussed such as the difference in the total plastic strain during electromigration testing and thermal cycling, the volume of material that is involved in determining the stresses, the average stress state, and the local stress distribution. Then, based on the studies of hillock morphology, a detailed mechanism for hillock formation is proposed, which is then used to motivate the observed behavior of the threshold stress $\Delta\sigma_{th}$ and its difference with the flow stress $\Delta\sigma_f$.

5.1 Comparison of $\Delta\sigma_{th}$ with $\Delta\sigma_f$ Determined by Wafer Curvature

During thermal cycling of a film on a substrate, elastic strains are generated which are approximately biaxial. If the film material is isotropic in-plane, these lead to a biaxial stress state. Similarly, the electromigration-induced accumulation of atoms at grain boundaries generates an approximate biaxial stress state where the average stress in the grain is only slightly different from the grain boundary normal stress. Therefore, assuming that the deformation mechanisms during electromigration at the cathode and anode end of a segment are similar to the deformation mechanisms during thermal cycling, then the electromigra-

tion threshold stress $\Delta\sigma_{th}$ should agree with $\Delta\sigma_f$. In the following, $\Delta\sigma_{th}$ is first compared with literature values obtained from the electromigration critical product and then with the measured flow stresses $\Delta\sigma_f$ for different film thicknesses, temperatures and annealing treatments.

5.1.1 Comparison with Literature Values

Values for the electromigration threshold stress $\Delta\sigma_{th}$ can be calculated from the critical product (equation 2.10) by assuming an appropriate value for Z^* (e.g. between -4 and -8, as suggested by Tu [10]). Fig. 5.1 shows an overview of electromigration threshold stresses $\Delta\sigma_{th}$ for unpassivated polycrystalline Al lines calculated from the critical products plotted in Fig. 2.3 using $Z^* = -6$, $\Omega = 1.66 * 10^{-29}\mathrm{m}^3$, $\mathrm{e} = 1.6 * 10^{-19}\mathrm{C}$, $\rho = 28 * 10^{-9}\Omega\mathrm{m}$. The data obtained here

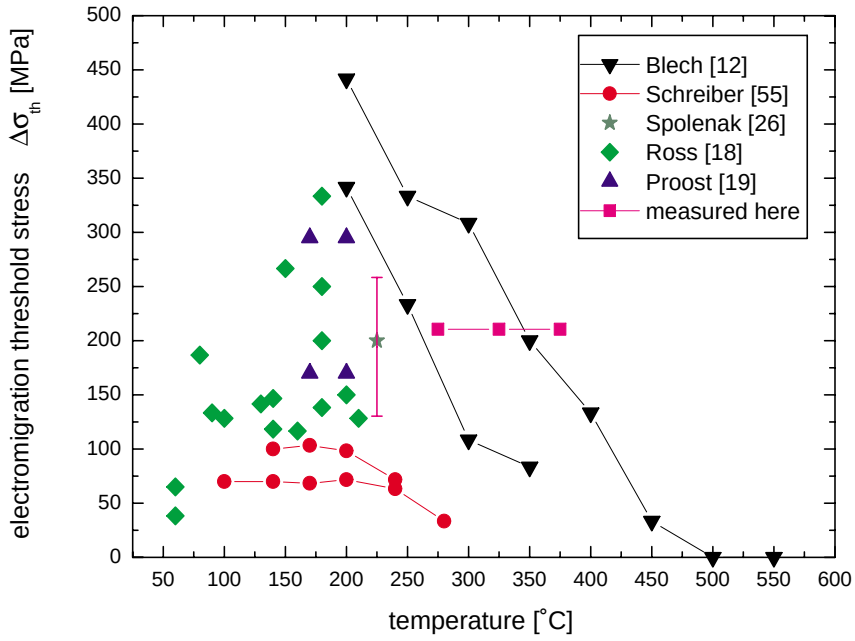

Figure 5.1: Electromigration threshold stresses $\Delta\sigma_{th}$ calculated from measured critical products as reported in the literature ($Z^* = 6$).

fall within the range of values quoted from the literature.

5.1.2 Comparison with Measured Flow Stresses $\Delta\sigma_f$

Values for the electromigration threshold stress $\Delta\sigma_{th}$ were calculated from the measured critical product for different values of Z^* and are plotted in Fig. 5.2 as a function of film thickness. The flow stresses $\Delta\sigma_f$ of the films, as determined by

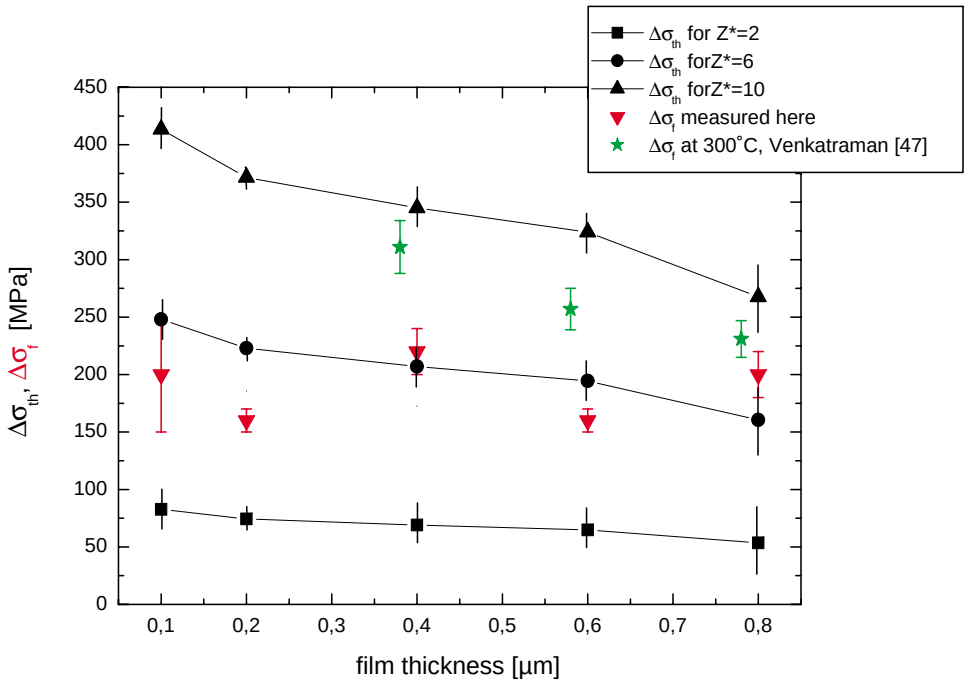

Figure 5.2: Electromigration threshold stress $\Delta\sigma_{th}$ (calculated from the measured critical product) and $\Delta\sigma_f$ (measured by wafer curvature) as a function of film thickness. For comparison, $\Delta\sigma_f$ determined by Venkatraman is also shown.

wafer curvature measurements (Fig. 4.12-4.16), are also shown in the figure. For the 100 and 200nm thick films there was no clear distinction between the elastic and plastic regime in the stress versus temperature cycle and the plotted values likely underestimate the actual flow stresses of the films. A value of $Z^* = -6$ gives reasonable agreement between the electromigration threshold stresses $\Delta\sigma_{th}$

and the measured flow stresses $\Delta\sigma_f$ for the thicker films. As a comparison, flow stresses measured by Venkatraman [47] for 0.38 to 1 μm thick pure Al films with a fixed grain size of 0.9 μm on SiO_2 at 300°C are also plotted in Fig. 5.2. They are somewhat larger than the values measured here.

Fig. 5.3 shows the temperature dependence of $\Delta\sigma_{th}$ and $\Delta\sigma_f$ for the 200, 400 and 600nm thick films. The flow stress $\Delta\sigma_f$ as a function of temperature is directly obtained from the wafer curvature cycles shown in Figs. 4.12, 4.14, and 4.15. The slope of $\Delta\sigma_f$ for the 400 and 600nm thick film is roughly 0.6 and 0.9 MPa/°C which is in reasonable agreement with the values obtained by Venkatraman (0.7 and 0.8 MPa/°C) [47]. In general, the temperature dependence of $\Delta\sigma_f$ is somewhat stronger than the temperature dependence of $\Delta\sigma_{th}$.

In Fig. 5.4 the stresses $\Delta\sigma_f$ and $\Delta\sigma_{th}$ are compared for the 600nm thick film as a function of annealing history. The flow stresses $\Delta\sigma_f$ in the as-deposited condition and after an anneal at 400 °C are obtained from the first and second wafer curvature cycle shown in Fig. 4.12 and are the same. In contrast $\Delta\sigma_{th}$ changes by roughly a factor of 2. This difference is substantial and is believed to indicate a difference in mechanisms for deformation during thermal cycling and during electromigration.

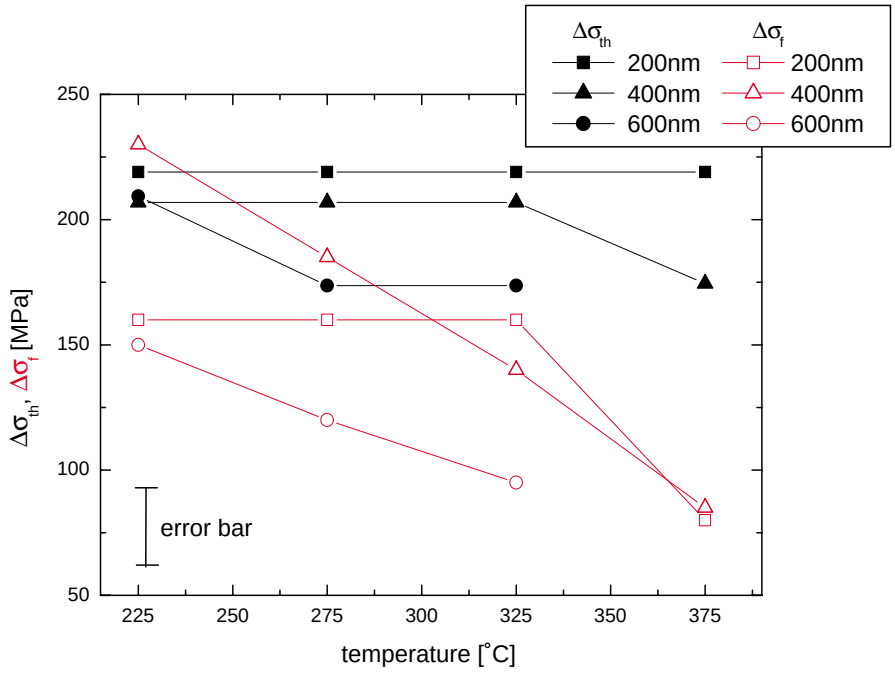

Figure 5.3: Comparison between $\Delta\sigma_{th}$ and $\Delta\sigma_f$ as a function of temperature for 200, 400 and 600nm thick Al films.

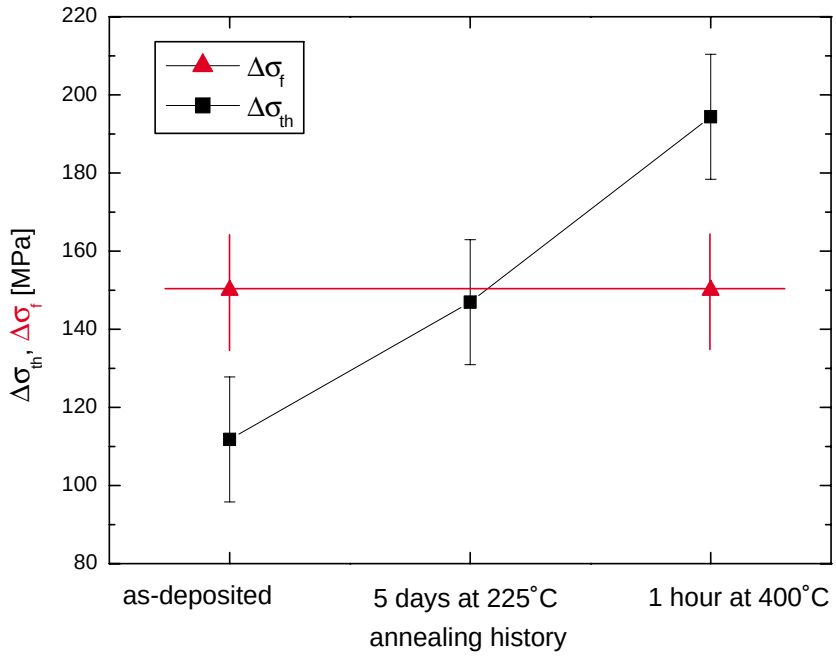

Figure 5.4: Comparison between $\Delta\sigma_f$ and $\Delta\sigma_{th}$ as a function of annealing history for a 600nm thick Al film.

5.2 Possible Reasons for the Disagreement between $\Delta\sigma_{th}$ and $\Delta\sigma_f$

In the previous section it has been shown that there are some significant differences between $\Delta\sigma_{th}$ generated during electromigration and $\Delta\sigma_f$ generated during thermal cycling. In this section possible explanations for this difference are presented.

5.2.1 Plastic Strain and Strain Rate

For the comparison of $\Delta\sigma_{th}$ with $\Delta\sigma_f$ it is important to consider the total plastic strain and the strain rate at which the two stresses are measured. In the case of the wafer curvature measurement, the total strain and the strain rate can easily be determined from the difference in thermal expansion coefficients and the heating rate. The total strain during the heating part of a wafer curvature cycle is

$$\epsilon = \Delta\alpha \cdot \Delta\mathrm{T} = 20.5 \cdot 10^{-6}/^{\circ}\mathrm{C} \cdot 400^{\circ}\mathrm{C} = 0.82\% \tag{5.1}$$

the majority of which is plastic, and the corresponding strain rate is roughly $-7 \cdot 10^{-6} s^{-1}$, for a heating rate of 20 °C/min.

For electromigration, the total elastic and plastic strain and strain-rate need to be carefully considered. The strain during electromigration is introduced locally due to material accumulation at the grain boundaries. As a first approximation the strain is assumed completely elastic below the electromigration threshold stress. Therefore, the plastic strain at the threshold stress can be estimated as the strain required for detectable damage formation in the SEM which is roughly 5 % strain. The average strain rate to reach the threshold stress can be roughly estimated from the time when damage formation is first visible in the SEM. For pure Al segments stressed at 1 MA/cm^2 at 225 °C damage formation was visible in the SEM after roughly 10-60 minutes leading to an average strain rate between 10^{-5} and $10^{-4} s^{-1}$.

The factor 10 or so difference in strain rate is usually not sufficient to result in large differences in the stress. However, the difference in total strain during electromigration and during thermal cycling is significant and may contribute to

differences in $\Delta\sigma_{th}$ and $\Delta\sigma_f$. For instance, if the larger strain developed during electromigration leads to work hardening or to the transition from primary to secondary creep, then a difference in the stress is expected.

5.2.2 Volume of Material Involved in Determining Stress

An important difference between $\Delta\sigma_f$ and $\Delta\sigma_{th}$ is the volume of material that is involved in determining the stresses. The flow stress $\Delta\sigma_f$ is a measure of the mechanical behavior of a large number of grains since appreciable plasticity is only observed when a large fraction of the grains deform plastically. However, the electromigration threshold stress $\Delta\sigma_{th}$ is determined when the first grain ("weakest grain") at the anode or cathode end of the 10 μm wide segment deforms plastically.

The implications of this difference are particularly apparent for the case of a film with a minority texture component. The films used for the electromigration samples have a strong (111) texture and a minority population of randomly oriented grains. The non-(111) grains will only make a small contribution (on the order of their area fraction) to the stress measured during wafer curvature. However, if one of the non-(111) grains is found near the anode or cathode end of a segment and if it forms electromigration damage more easily than the (111) grains, then it will determine the electromigration behavior and $\Delta\sigma_{th}$. Such a picture is strongly supported by the experimental observation that hillocks are preferentially composed of non-(111) grains.

A second example of the importance of the volume of material involved in deformation results when there are pre-existing voids present at the cathode end of the segments. Such tiny, nanometer-scaled voids, are often present in sputter-deposited films [56] and can provide efficient sinks for vacancies, particular at the grain boundaries. In this case material depletion from the cathode end due to electromigration will not lead to high tensile stresses in the grain boundaries. This is supported by stress measurements of Blech [1] where the cathode end of a segment was found to be in a state of zero stress rather than being in tension. In contrast, thermal stresses are created due to different thermal expansion of the substrate and the film. The adhesion to the substrate leads to tensile stresses in

the grain interiors even if the stress at the grain boundaries is relaxed by the small pre-existing voids. Therefore, the average tensile stress in the film during thermal cycling can be much higher than in the grain boundaries during electromigration which may also contribute to the difference between $\Delta\sigma_f$ and $\Delta\sigma_{th}$.

5.2.3 Average Stress State

The stress distribution that is generated during electromigration is different from that generated during thermal cycling. For an isotropic homogeneous film material, thermal cycling leads to a biaxial strain state whereas electromigration leads to the generation of an inhomogeneous stress state that is to first order approximately a biaxial stress state. For films which have different texture components the difference between biaxial stress and biaxial strain could be important. Under biaxial loading conditions, (111) grains have the largest elastic modulus and the smallest resolved shear stress (according to the Schmidt factor) [57]. During thermal cycling the elastic strain energy in the grains can be expressed as

$$E = \frac{1}{2} \cdot Y \cdot \epsilon^2 \ , \tag{5.2}$$

where ϵ is the strain and Y the Young‘s modulus of the grain. Therefore, non-(111) grains have a lower elastic strain energy ($Y_{non\ (111)} < Y_{(111)}$). During electromigration, however, differently textured grains are rather in a uniform stress state than in a uniform strain state and the elastic strain energy in the grains is given by

$$E = \frac{1}{2} \cdot \frac{\sigma^2}{Y} \ . \tag{5.3}$$

which means that non-(111) grains have a higher elastic strain energy.

Plastic deformation during both thermal cycling and electromigration is expected to occur in non-(111) grains at lower stresses than in (111) grains because (111) grains have the lowest possible Schmidt factor and the stress variations in different textured grains, due to the different Young‘s moduli, are expected to be smaller than variations in flow stress due to in the Schmidt factor. This is also supported by X-ray stress measurements during microtensile experiments which showed that (100) grains deform at lower stresses than (111) grains [58]. For the films used in making the electromigration test samples, which have a strong (111)

texture component plus some randomly oriented grains, one would expect dislocation glide to set in at lower stresses in the non-(111) grains than in the (111) grains. In addition, because the stress in these grains is lower, the elastic strain energy is lower and there is a driving force for atoms to diffuse to the non-(111) grains as well as for grain growth of the non-(111) grains.

5.2.4 Local Stress Distribution

A further important difference between the thermal and electromigration- induced stress distribution is the fact that the electromigration-induced stress distribution is inhomogeneous. The in-plane strains during electromigration are introduced locally at the grain boundaries while during thermal cycling in-plane strains are introduced at the film/substrate interface, assuming perfect adhesion. For an elastically homogeneous film, thermal cycling leads to a homogeneous biaxial strain state, whereas the material accumulation at the grain boundary during electromigration causes stress gradients and large stress concentrations.

To quantitatively compare the thermal and electromigration-induced stress distributions a finite element analysis using the commercial software ANSYS 5.4 was performed. The model used for the calculation is schematically shown in Fig. 5.5. The thickness and grain size of Al was 400nm, the thickness of the TiN 245nm and the thickness of the silicon 400nm. A uniform stress [1] of 200 MPa was applied on the grain boundary and the boundary conditions are indicated by triangles. Due to the symmetry only half of the grain is modelled. The material properties used for the Al, Al_2O_3, TiN, and Si are listed in the program source code in Appendix C.2. An elastic calculation was performed elastically for the case of plane strain.

Fig. 5.6 shows the stress distribution σ_y in the Al grain resulting from a grain boundary normal stress of 200 MPa. This stress results in a maximum displacement of the grain boundary of around 1nm. The stress distribution is non-uniform because the adhesion to the substrate and the native oxide act as constraints on the film deformation. The stress σ_y reaches its maximum value

[1] The normal stress on the grain boundary is assumed to be independent of position because matter is expected to be transported in the grain boundary until local equilibrium is reached.

at approximately half of the film thickness and decreases strongly towards the substrate and surface. The average stress in the grain $\bar{\sigma_y}$ was calculated to be 163 MPa, which is somewhat lower than the applied grain boundary normal stress of 200 MPa, as expected. The stress σ_y along path one to five from the surface to the substrate (drawn as dashed lines in Fig. 5.6) is plotted in Fig. 5.7 and shows the relatively unstressed bottom of the grain.

Fig. 5.8 shows the stress distribution of σ_z in the grain. As expected, the stress σ_z has low values in most of the grain area, because there is no average constraint in the z-direction and only results from non-uniformity of σ_y. At the corners of the grain, however, σ_z can have quite large values. Fig. 5.9 shows the stress distribution of σ_z in the area of the grain boundary intersection with the Al/TiN interface. High tensile normal stresses are developed in this area at the interface which can strongly enhance the sink activity.

Figs. 5.10 and 5.11 show the hydrostatic stress in the grain and at the area of the grain boundary intersection with the interface. There are clearly hydrostatic stress gradients from the grain boundary through the bulk of the grain to the Al/TiN interface which can provide a driving force for diffusion to the interface. Finally, Fig. 5.12 shows the von Mises stress in the grain, which can be regarded as an estimate of the resolved shear stress for dislocation glide. The average von Mises stress in the grain is roughly 170 MPa, which is a significant fraction of the grain boundary normal stress. Thus, to first order, it is expected that dislocation glide will be activated within a grain as soon as the normal stress reaches the critical resolved shear stress for dislocation glide.

Summarizing, even if in a first order it seems reasonable to compare $\Delta\sigma_f$ and $\Delta\sigma_{th}$, a carefully study in this section has shown that there are several differences between the stresses and strains generated during thermal cycling end electromigration which may account for the disagreement between $\Delta\sigma_f$ and $\Delta\sigma_{th}$.

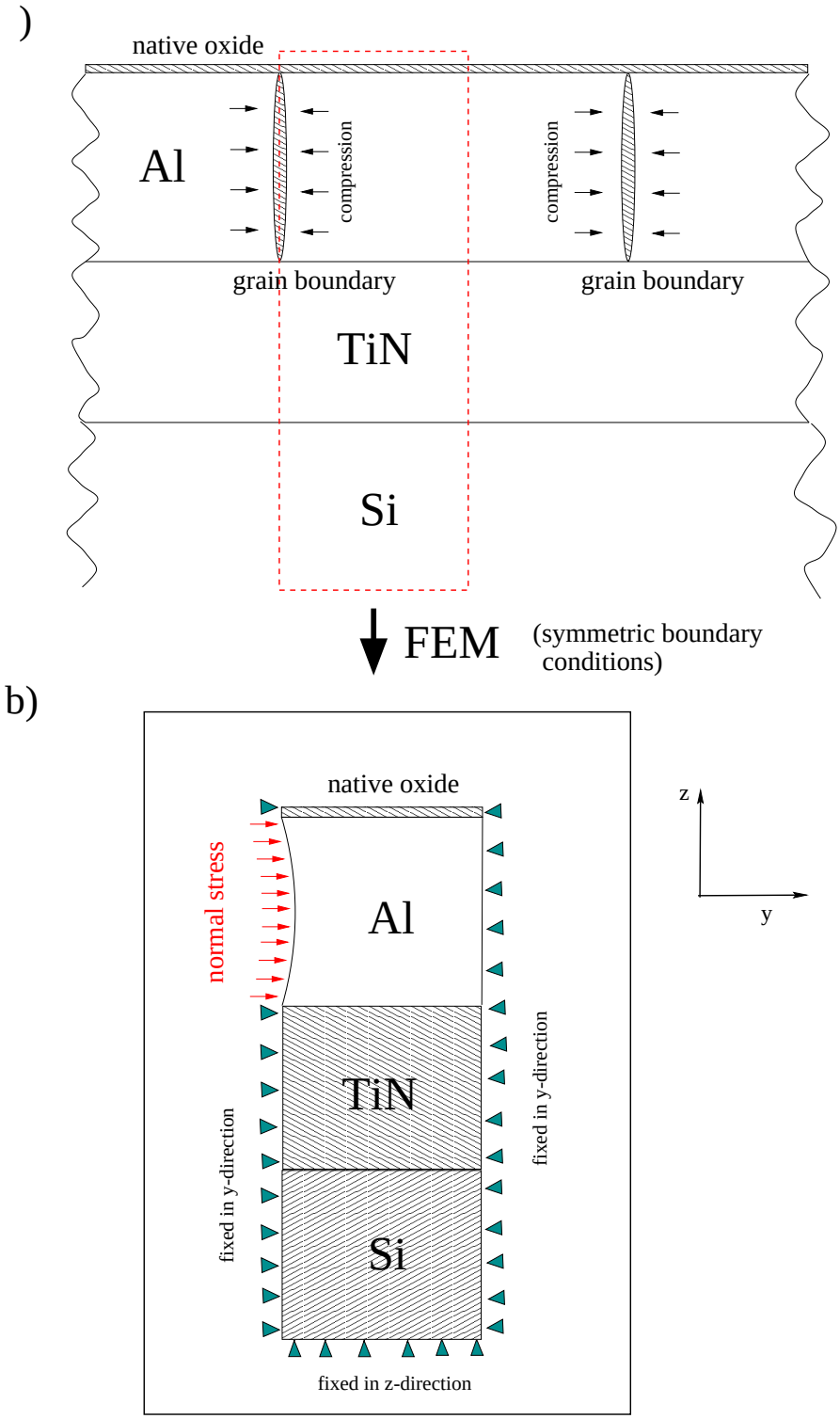

Figure 5.5: (a) Cross-sectional view of a polycrystalline Al segment on TiN/Si showing electromigration-induced mass deposition at grain boundaries and resulting normal stresses. (b) Schematic view of the finite element model used to calculate the electromigration-induced stress distribution in the grain (not to scale, displacement of grain boundary is greatly exaggerated).

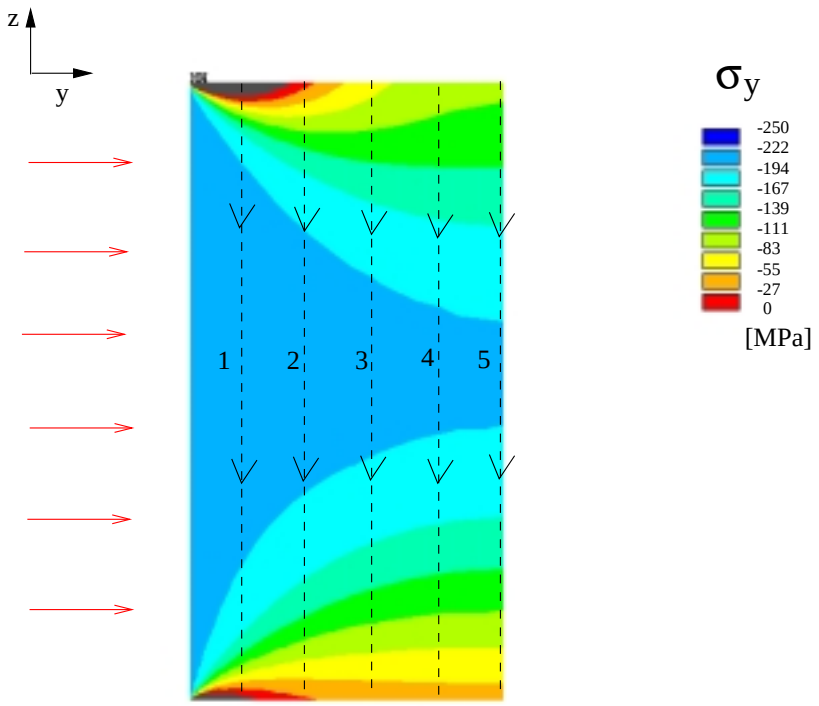

Figure 5.6: Electromigration-induced stress distribution σ_y in a 400nm thick and 400nm wide Al grain on TiN/Si resulting from a grain boundary normal stress of 200 MPa (because of the symmetry only half of the grain is shown).

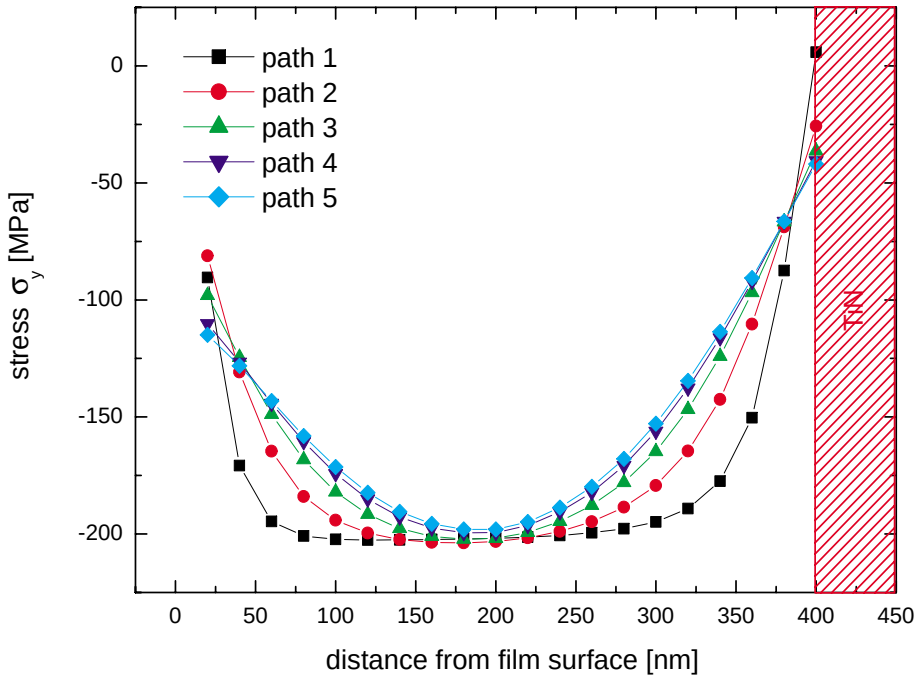

Figure 5.7: Stress σ_y along different paths in the grain.

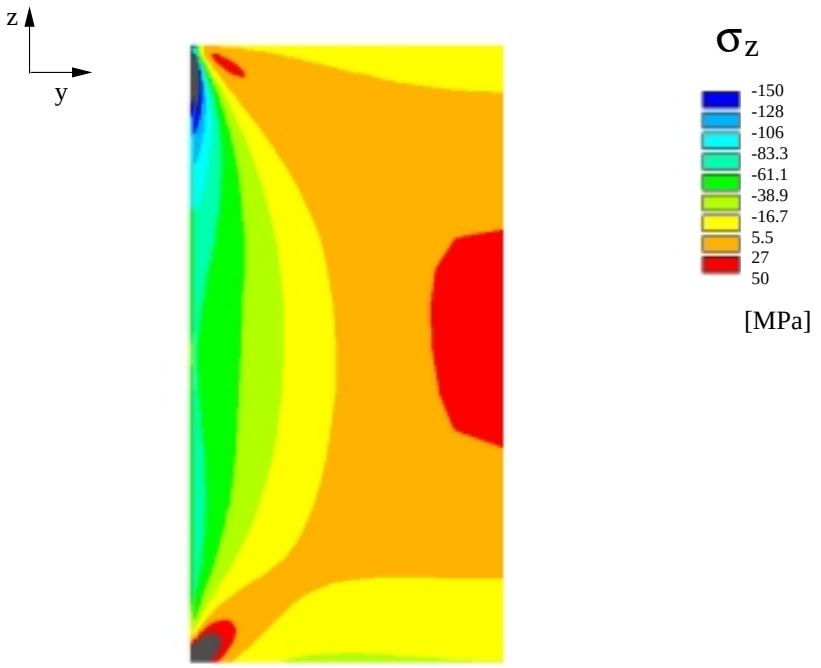

Figure 5.8: same as in Fig. 5.6 for the stress component σ_z.

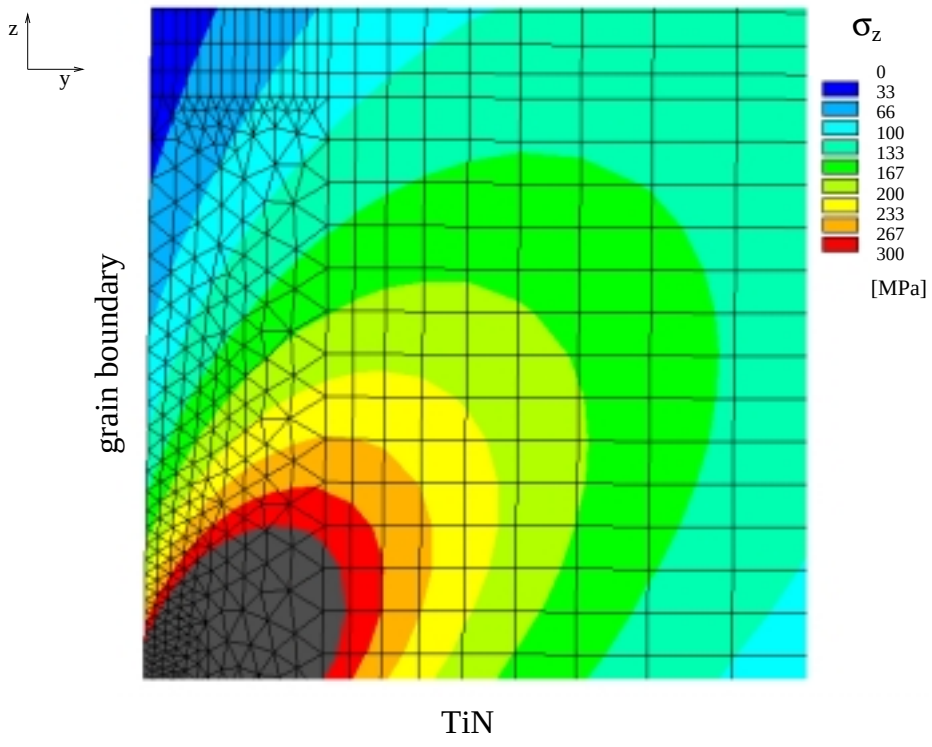

Figure 5.9: Stress distribution of σ_z in the area of the grain boundary intersection with the Al/TiN interface.

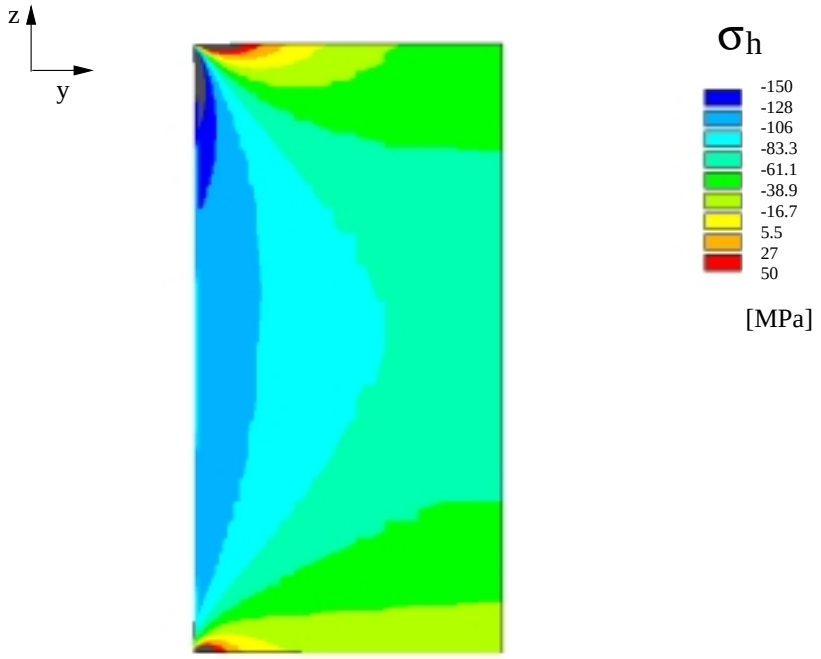

Figure 5.10: same as in Fig. 5.6 for the hydrostatic stress σ_h.

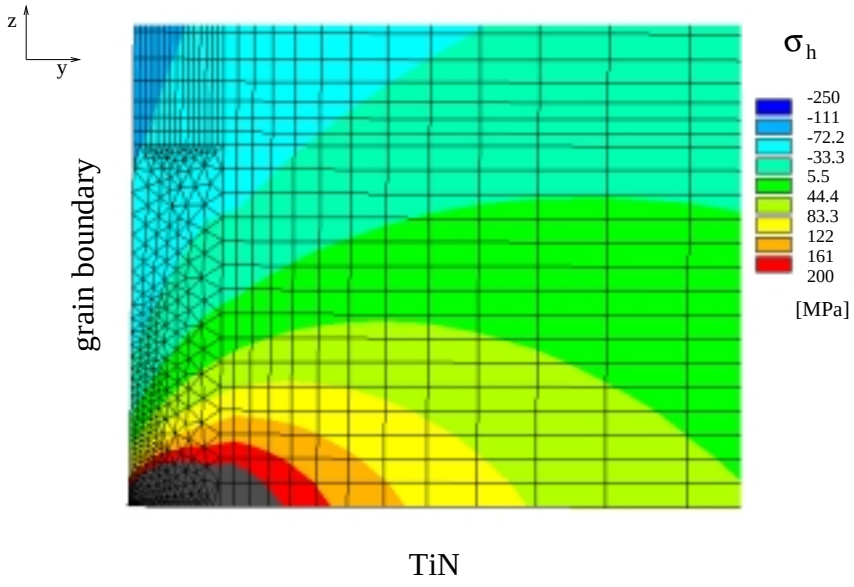

Figure 5.11: Stress distribution of σ_h in the area of the grain boundary intersection with the Al/TiN interface.

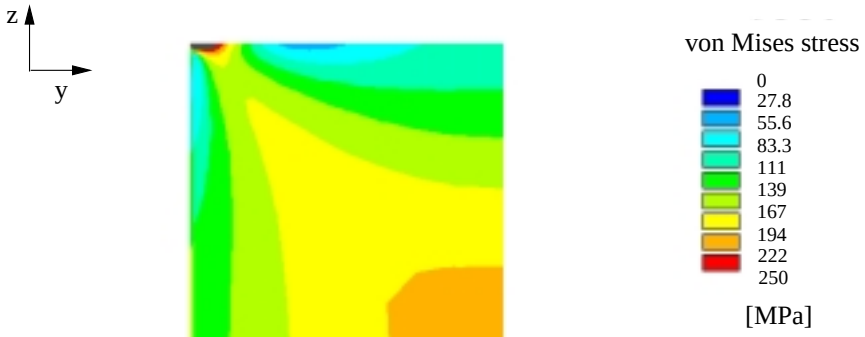

Figure 5.12: same as in Fig. 5.6 for the von Mises stress.

5.3 A Possible Mechanism for Hillock Growth

In this section, a possible mechanism for electromigration-induced hillock formation is proposed. This model is based on the observations of hillock morphology which indicate that growth occurs by epitaxial addition of atoms at the Al/TiN interface, occurs predominately in non-(111) grains, and is often accompanied by grain growth.

Given these considerations a possible mechanism for hillock formation is proposed which is schematically illustrated in Fig. 5.13. Deposition of material at the grain boundaries due to electromigration creates compressive stresses up to a certain threshold stress (a). Once the threshold stress is reached deformation occurs by diffusion of the atoms along the grain boundary to the Al/TiN interface as well as by plastic deformation in the grain by dislocation glide (b). It is not clear which mechanism is rate limiting but they need to be coupled because the grain maintains a homogeneous orientation even when material is incorporated non-uniformly at the bottom interface.

Diffusion of the atoms from the grain boundary to the interface is driven by the compressive normal stress at the grain boundary and tensile normal stress at the interface (that is initially due to the grain boundary normal stress (see Fig. 5.9)). The energy required to add atoms at the Al/TiN interface likely depends on the texture of the grain [59] and on the misorientation angle to the TiN diffusion barrier layer (which is (111) textured). This might also account for preferred growth of hillocks in non-(111) grains. In any case, although atoms will probably initially diffuse to the interface region near the grain boundary, where the tensile stress is largest, once atoms are incorporated there, the region of high tensile stress will move along the interface into the grain center, promoting atom incorporation uniformly at the interface.

Dislocation glide will happen first in non-(111) grains due to a higher Schmidt factor. If it occurs non-uniformly then it will lead to a shape change of the top surface of the grain and thus to strain of the native oxide. If the dislocation glide is highly localized [2], and occurs in glide bands, this can lead to small steps in the surface of the hillock, as has often been experimentally observed (see for

[2] e.g. due to fracture of the native oxide

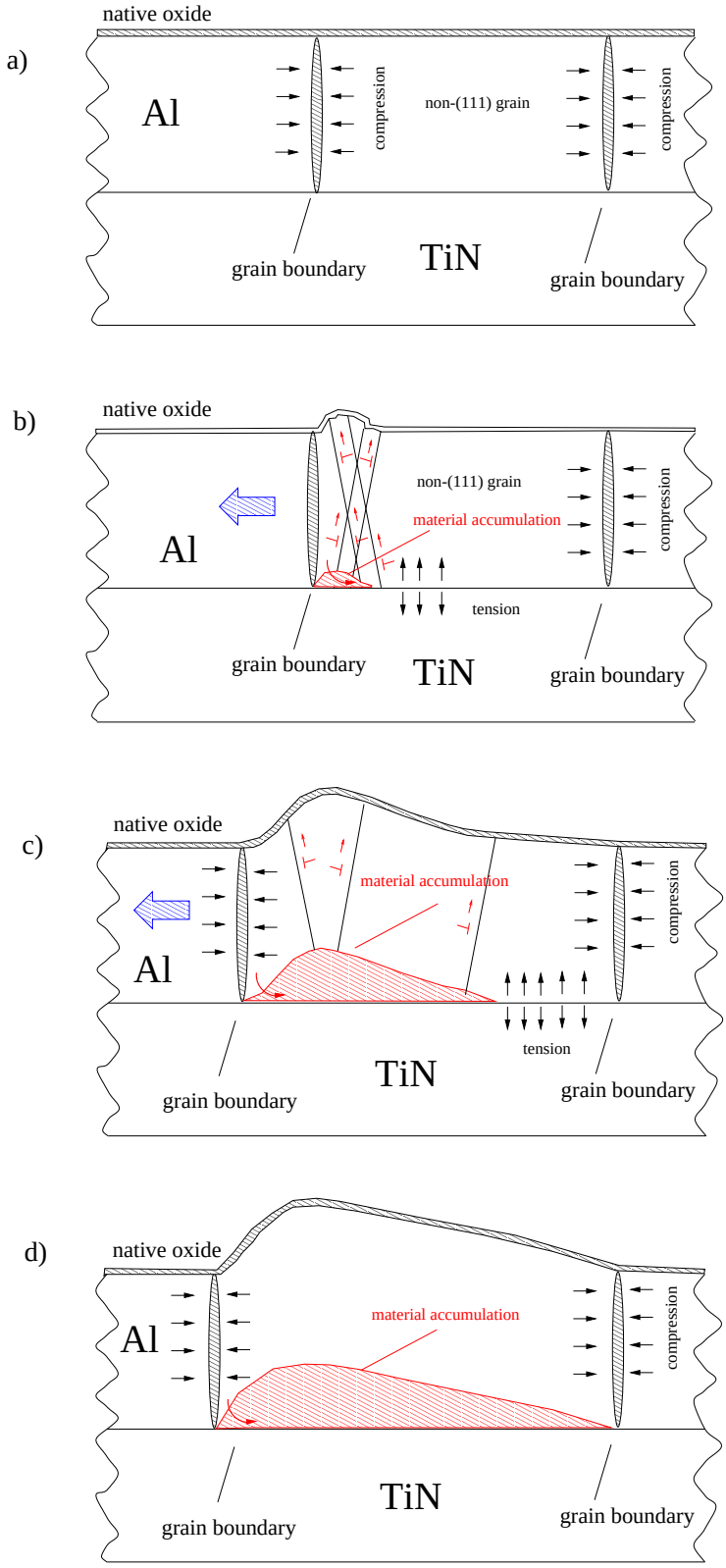

Figure 5.13: Possible mechanism for electromigration-induced hillock formation.

example Fig. 4.39). However, whether the observed steps have the appropriate crystallographic orientation has not been investigated. To continue this process new dislocations must be nucleated at the interface which might be aided by the diffusion of atoms to this interface.

The observed grain boundary migration during hillock growth (c) may by caused by preferred diffusion of atoms to the non-(111) grains due to lower strain energy. During grain boundary migration, material which is supplied by electromigration into the grain boundary, diffuses continuously to the Al/TiN interface and causes the hillock to grow in the entire grain. The resulting shape of the hillock (d) is consistent with the shape of the hillock shown in Fig. 4.42 and Fig. 4.43.

5.3.1 Possible Threshold Stresses

The proposed mechanism for hillock formation presents several possible threshold stresses which are discussed briefly below. These are the critical stress for dislocation glide, for incorporation of atoms at the interface, or for cracking of the native oxide.

The stress required for deformation of grains by dislocation glide is expected to increase with decreasing film thickness and grain size according to widely accepted models of dislocation motion in thin films [51], [52]. This is qualitatively in agreement with the measured critical product. The temperature dependence of this deformation mechanism is expected to be quite weak, again in agreement with the measured critical product. However, the increase of critical product after annealing can not be explained by plastic deformation.

The incorporation of material at the interface is associated with interface dislocation climb, which requires a certain threshold stress. When the interface dislocation tracks along the irregular shape of the interface, its overall length fluctuates and thereby also its self energy. As a result a threshold stress is required to make a interface dislocation act as a sink. This concept has been introduced by Arzt et al. [28] for grain boundary dislocation climb in order to explain the threshold stress for diffusional creep in pure metals which was found to be on the

order of

$$\sigma_{th.} = \frac{Gb}{d} , \tag{5.4}$$

where G is the shear modulus, b the dislocation Burgers vector and d the grain size. Assuming that the above expression for the threshold stress applies to interface dislocations, then one could expect that the critical product would increase with decreasing film thickness due to the decrease in grain size, as experimentally observed. The temperature dependence for the threshold stress would be expected to be quite weak, because the self energy of a dislocation is almost independent of temperature (any temperature dependence arises from the thermal dependence of the shear modulus), again in agreement with the experiments. An annealing treatment associated with increasing interface roughness and precipitates is expected to increase the critical product strongly because climbing of the interface dislocation will cause stronger fluctuations in length and self energy. In addition, interface precipitates can act as pinning points.

A further possibility for the origin of the threshold stress in the model for hillock growth might be cracking of the native oxide. This process is expected to be fairly insensitive to temperature, since the fracture toughness of Al_2O_3 is almost independent of temperature in the investigated range [34]. The increase in critical product after annealing might be explained by the increase in native oxide thickness. The effect of film thickness is hard to predict because it depends on exactly where and how the oxide fractures.

In summary, a mechanism for electromigration-induced hillock formation has been proposed which is based on the observations of hillock morphology. This model explains the observed difference in $\Delta\sigma_f$ and $\Delta\sigma_{th}$ and can account qualitatively for the influence of film thickness, testing temperature and annealing treatment on the critical product.

Chapter 6

Summary

Electromigration in interconnects is a complicated process dependent on diffusion, microstructure, and mechanical stresses. The existence of an electromigration threshold stress $\Delta\sigma_{th}$ below which no damage occurs was discovered 30 years ago, but the mechanism responsible for this threshold and its relation to film mechanical properties has remained an open question. Therefore, the goal of this thesis was to compare the electromigration threshold stress with the mechanical properties of the film material in order to identify the mechanisms which determine the threshold stress.

A comparison of the electromigration threshold stress $\Delta\sigma_{th}$ with the difference of flow stress $\Delta\sigma_f$ in compression and tension has led to the following results:

- The electromigration threshold stress $\Delta\sigma_{th}$ was found to increase almost linearly with film thickness whereas $\Delta\sigma_f$ did not show a systematic trend.
- The temperature dependence of $\Delta\sigma_{th}$ was observed to be weaker than for $\Delta\sigma_f$.
- Annealing of the samples before testing increased the electromigration threshold stress by more than 60 % but did not change $\Delta\sigma_f$.

To understand why these two stresses are different the electromigration-induced hillock morphology was investigated using FIB microscopy and Electron Back-Scatter Diffraction. The hillocks were typically composed of one or more non-(111) textured grains which grew by epitaxial addition of atoms at the Al/TiN

interface and by grain boundary migration. Based on these observations a model was proposed to account for the behavior of the electromigration threshold stress. In this model, the process of hillock formation was described by the combined glide of dislocations between the bottom and the top of the grain and by the diffusion of atoms from the grain boundary to the Al/TiN interface. The difference between the electromigration threshold stress and the flow stress was explained by the fact that the flow stress is determined by the average deformation behavior of many grains, which are mostly (111) textured, whereas the electromigration threshold stress is determined by the deformation behavior of non-(111) grains. The model also provides qualitative agreement with the observed dependence of the electromigration threshold stress on film thickness, testing temperature and annealing treatment.

Chapter 7

Bibliography

[1] I.A. Blech and K.L. Tai. Measurements of stress gradients generated by electromigration. *Appl. Phys. Lett*, 30:pp. 387–389, 1977.

[2] I.A. Blech. Diffusional back flows during electromigration. *Acta mater.*, 46(11):pp. 3717–3723, 1998.

[3] P.-C. Wang, G.S. Cargill, I.C. Noyan, and C.-K. Hu. Electromigration-induced stress in aluminum conductor lines measured by x-ray microdiffraction. *Appl. Phys. Lett.*, 72:pp. 1296–1298, 1998.

[4] R.S. Hemmert and M.Costa. Electromigration-induced compressive stresses in encapsulated thin-film conductors. *IEEE Proc. Int. Reliab. Phys. Symp.*, 64:pp. 64–69, 1991.

[5] I.A. Blech and E. Kinsbron. Electromigration in thin aluminum films on molybdenum surfaces. *Thin Solid Films*, 25:pp. 327–334, 1975.

[6] M.A. Korhonen, P. Borgesen, K.N. Tu, and Che-Yu Li. Stress evolution due to electromigration in confined metal lines. *J. Appl. Phys.*, 73:pp. 3790–3799, 1993.

[7] E. Glickman, N. Osipov, A. Ivanov, and M. Nathan. Diffusional creep as a stress relaxation mechanism in electromigration. *J. Appl. Phys*, 83:pp. 100–107, 1998.

[8] H.B. Huntington and A.R. Grone. Current induced marker motion in gold wires. *J. Phys. Chem. Solids.*, 20:pp. 76–87, 1961.

[9] H.B. Huntington. *Diffusion in Solids, Recent Developments*. Academic Press, New York, 1975.

[10] K.N. Tu. Electromigration in stressed thin films. *Physical Review B*, 45:pp. 1409–1413, 1992.

[11] T. Kwok and in P.S. Ho. *Diffusion Phenomena in Thin Films and Microelectronic Materials*. Noyes, Park Ridge, NJ, 1988.

[12] I.A. Blech. Electromigration in thin aluminum films on titanium nitride. *J. Appl. Phys*, 47:pp. 1203–1208, 1976.

[13] I.A. Blech and C. Herring. Stress generation by electromigration. *Appl. Phys. Lett*, 29:pp. 131–133, 1976.

[14] A. P. Sutton and R. W. Balluffi. *Interfaces in Crystalline Material*, chapter 10, page 620. Oxford University Press, 1995.

[15] C. Herring. Diffusional viscosity of a polycrystalline solid. *J. Appl. Phys.*, 21:pp. 437–445, 1950.

[16] N.G. Ainslie, F.M. D'Heurle, and O.C. Wells. Coating, mechanical constraints, and pressure effects on electromigration. *Appl. Phys. Lett.*, 20 (4):pp. 173–174, 1972.

[17] H.-U. Schreiber. Electromigration mechanisms in aluminum lines. *Solid States Electronics*, 28:pp. 1153–1163, 1984.

[18] C.A. Ross. PhD thesis, MIT, 1988.

[19] J. Proost. Electromigration-induced drift in damascene and plasma etched al(cu) films. *J. Appl. Phys.*, 87/1:pp. 99–109, 2000.

[20] Witt C. PhD thesis, MPI, not published yet.

[21] C.A. Ross, J.S. Drewery, R.E. Somekh, and J.E. Evetts. The effect of anodization on the electromigration drift velocity in aluminum films. *J. Appl. Phys.*, 66:pp. 2349–2355, 1989.

[22] L. Kisselgof and J.R. Lloyd. Electromigration induced failure as a function of via interface. In *Materials Reliability in Microelectronics VII*, volume 473, pages 401–406. MRS Symp. Proc., 1997.

[23] T. Yamaoka and T. Yamauchi. Void-free metallization by controlling sputtering conditions of tin barrier films. In *Materials Reliability in Microelectronics VI*, volume 428, pages 487–492, Pittsburgh, PA, USA, 1996. MRS Symp. Proc.

[24] C. A. Ross. Stress and electromigration in thin film metallisation. In *Materials Reliability Issues in Microelectronics*, volume 225, pages 35–46. Mat. Res. Soc. Symp. Proc., 1991.

[25] C.A. Ross, J.S. Drewery, R.E. Somekh, and J.E. Evetts. Electromigration and mechanical stress in aluminum conductor tracks passivated by anodisation. *Journal of Electronic Materials*, 19:pp. 911–918, 1990.

[26] Ralph Spolenak. *Alloying Effects in Electromigration.* PhD thesis, MPI Stuttgart, 1999.

[27] J. Cadek. *Creep in metallic materials*, page 217. Elsevier, Amsterdam, 1988.

[28] E. Arzt, M.F. Ashby, and R.A. Verrall. Interface controlled diffusional creep. *Acta metall.*, 31:pp. 1977–1988, 1983.

[29] H. J. Frost and M. F. Ashby. *Deformation Mechanism Maps*, chapter 4. Pergamon, Oxford, 1982.

[30] W.D. Nix and E. Arzt. On void nucleation and growth in metal interconnect lines under electromigration conditions. *Metall. Trans.*, 23A:pp. 2007–2013, 1992.

[31] R. J. Gleixner and W. D. Nix. An analysis of void nucleation in passivated interconnect lines due to vacancy condensation and interface contamination. In *Thin Films: Stresses and Mechanical Properties VI*, volume 418, pages 405–410. Symposium Mater. Res. Soc., 1997.

[32] J. E. Harris and B. C. Masters. *Phil. Mag.*, 17:217, 1968.

[33] P. D. Dobson, S. Kritzinger, and R. E. Smallman. *Phil. Mag.*, 17:769, 1968.

[34] N. Claussen, R. Pabst, and C. P. Lahmann. Influence of microstructure of Al_2O_3 and ZrO_2 on K_{IC}. In *Mechanical Properties of Ceramics*, volume 25, pages 139–150. Proc. Brit. Ceram. Soc., 1975.

[35] Harold Kahn. *Electromigration behavior and reliability of aluminium-based multilevel interconnects for integrated circuits.* PhD thesis, MIT, 1992.

[36] William A. Nash. *Strenght of Materials.* Mc Graw Hill, Singapore, 1987.

[37] J. J. Wortman and R. A. Evans. Young‘s modulus, shear modulus, and poisson‘s ratio in silicon and germanium. *J. Appl. Phys.*, 36(1):pp. 153–156, 1965.

[38] C.A. Volkert. Stress and plastic flow in silicon during amorphization by ion bombardment. *J. Appl. Phys.*, 70:pp. 3521–3527, 1991.

[39] G.G. Stoney. The tension of metallic films deposited by electrolysis. *Proc. R. Soc.*, A82:pp. 172–175, 1909.

[40] D. L. Barr and W.L. Brown. Contrast formation in focussed ion beam images of polycrystalline aluminum. *J. Vac. Sci. Technol. B*, pages 2580–2583, 1995.

[41] B.D. Cullity. *Elements of X-Ray Diffraction.* Addison-Wesley Publishing Company, Inc, 1978.

[42] W. W. Mullins. The effect of thermal grooving on grain boundary motion. *Acta Met.*, 6:pp. 414–427, 1958.

[43] T. Wöhner, G. Ecke, and H. Rösler and S. Hofmann. Sputter-induced surface roughness of polycrystalline al films and its influence on aes depth profiles. *Surface and Interface Analysis*, 26:pp. 1–8, 1998.

[44] A. Strecker, U. Salzberger, and J. Mayer. *Prakt. Metallogr.*, 30:482, 1993.

[45] T. Kouno, M. Hosaka, h. Niwa, and M. Yamada. Effect of Al_3Ti intermetallic compound on electromigration lifetime of al alloy interconnections. *J. Appl. Phys*, 84 (2):pp. 742–750, 1998.

[46] I. Olefjord, P. Marcus, H. J. Mathieu, and S. Hofmann. Aes sputter depth profiling of thin aluminium oxide. In *ECASIA 95*, pages 188–191.

[47] R. Venkatraman. *Plasticity and flow stresses in aluminum thin films on silicon*. PhD thesis, Stanford, 1992.

[48] A. K. Sinha and T. T. Sheng. The temperature dependence of stresses in aluminum films on oxidized silicon substrates. *Thin Solid Films*, 48:pp. 117–126, 1978.

[49] D. S. Gardner and P. A. Flinn. Mechanical stress as a function of temperature in aluminum films. *IEEE Transactions on Electron Devices*, 35:pp. 2160–2169, 1988.

[50] Paul A. Flinn, Donald S. Gardner, and William D. Nix. Measurement and interpretation of stress in aluminum-based metallization as a function of thermal history. *IEEE Transactions on electron devices*, ED-34(3):689–699, 1987.

[51] W.D. Nix. Mechanical properties of thin films. *Metall. Trans. A*, 20A:pp. 2217–2245, 1989.

[52] J. J. Clement and C.V. Thompson. Modeling electromigration-induced stress evolution in confined metal lines. *J. Appl. Phys*, 78:pp. 900–904, 1995.

[53] H. Wever. *Elektro- und Thermotransport in Metallen*, chapter 1. Johann Ambrosius Barth Leipzig, 1973.

[54] C.V Thompson. The yield stress of polycrystalline thin films. *J. Mater. Res.*, 8:pp. 237–238, 1993.

[55] H.-U. Schreiber. Electromigration threshold in aluminum films. *Solid States Electronics*, 28:pp. 617–626, 1985.

[56] J. R. Llyod and S. Nakahara. *J. Vac. Sci. Technol.*, 14:655, 1977.

[57] W. F. Hosford. *The Mechanics of Crystals and Textured Polycrystals*, chapter 2. Oxford University Press, 1993.

[58] M. Hommel. PhD thesis, MPI, 2000.

[59] George H. Gilmer, Hanchen Huang, Tomas Diaz de la Rubia, Jacques Dalla Torre, and Frieder Baumann. Lattice monte carlo models of thin film deposition. *Thin Solid Film*, 365/2:pp. 189–200, 1968.

[60] R.K. Watts. *VLSI Technology S.M. Sze*, chapter 4, pages 155–170. McGraw-Hill Book Company, 1988.

[61] Mark A. McCord. Introduction to electron-beam lithography. In *Microlithography 1999: SPIE's International Symposium on Microlithography*, Santa Clara, Mar-1999.

[62] Mark A. McCord and Michael J. Rooks. *Handbook of Microlithography, Micromachining and Microfabrication*, chapter 2. SPIE, 1997.

[63] J.W. Coburn. *Plasma Etching and Reactive Ion Etching*. American Vacuum Society Monograpph Series, IBM Research Laboratory San Jose, California 95193.

[64] R.J. Schutz. *VLSI Technology S.M. Sze*, chapter 5, pages 184–232. McGraw-Hill Book Company, 1988.

[65] M. Sato and H. Nakamura. Reactive ion etching using $SiCl_4$. *J. Vac. Sci. Technol.*, 20 (2):pp. 186–190, 1982.

Chapter 8

Table of Symbols and Abbreviations

EBSD	electron back-scattered diffraction
FIB	focused ion beam
SEM	scanning electron microscope
SIMS	secondary ion mass spectrometry
TEM	transmission electron microscope
d	grain size
D	diffusivity
E	electric field
F	driving force
h	film thickness
J	atomic flux
J_{EM}	electromigration flux
J_{σ}	stress-driven backflux
j	current density
j_{th}	threshold current density
l	segment length
m	mobility
N	atomic concentration

T	absolute temperature
v	drift velocity
Y	Young‘s modulus
w	segment width
Z^*	effective valence number (here $Z^* = 6$)
$\Delta\sigma_{th}$	electromigration threshold stress
$\Delta\sigma_f$	difference of flow stress in compression and tension
μ_a	chemical potential of an atom
μ_v	chemical potential of a vacancy
Ω	atomic volume
ρ	resistivity
σ_n	grain boundary normal stress

Appendix A

Fabrication Process

For producing appropriate test samples of different film thicknesses up to 800nm Al on 200nm TiN on 45nm Ti on 200nm SiO_2 on a (100) Si substrate the conventional used lift off process was not suitable any more and a new process had to be developed consisting of a combination of e-beam lithography and reactive ion etching (RIE). The process involves two steps as shown in Fig. A.1. In the first step continuous lines of TiN and Al are etched from the metal layer and in the second step segments are made in the Al.

This process has many advantages in comparison to the conventional lift-off process with a subsequent wet etch. With the RIE process it is possible to produce test samples with vertical walls, even for high aspect ratios. Therefore geometrical dimensions such as length and width of a segment are well defined and can be measured easily. In case of a lift-off process with a subsequent wet etch the walls of the structures are quite oblique and therefore the width and the length of the segments are hard to determine. This becomes worse with increasing thickness of the structures. The wet etch process is also not very reproducible, because etching rates are often different even on the same chip. This results in some structures being significantly overetched and some structures being not etched completely. To measure the critical product as accurately as possible it is necessary to produce test samples with well defined geometrical dimensions and therefore the RIE process has to be used. A second advantage of the RIE process is that it is not necessary to pre-pattern a resist before film deposition. This enables one to have all films made with one deposition process and making all the

test samples from the same films. This is particular useful if one wants to check the obtained results for reproducibility or wants to use a new test sample design, because then always the same films can be used. The subsequent structuring steps and also important details that were used to develop the optimized process are described below and recorded for the use of others.

A.1 E-beam Lithography and Development

A.1.1 Theoretical Backround

In this paragraph a brief introduction to e-beam lithography will be given, as can be found for example in S.M. Sze VLSI Technology [60] or in [61], [62]. E-beam lithography is an important technique in fabricating integrated circuits where the pattern of a mask is transmitted to a metal layer. The mask usually consists of a thin resist layer which is deposited on the metal layer, exposed by an electron beam and subsequently developed. The pattern of the resist is then transmitted to the metal layer by reactive ion etching as described in the next section. In principle there are two different kinds of e-beam resists: Negative and positive resists. In the negative resist the exposure to the electron beam leads to formation of bonds between the polymer chains making it less soluble in a developer solution. The larger the molecules the fewer crosslinks per unit volume are required for insolubility. Therefore, the sensitivity of the resist increases with increasing molecular weight. The polymer molecules in a resist usually have a distribution of lengths and therefore a distribution of sensitivities. The narrower this distribution the higher is the contrast of the resist. A high contrast is important for achieving vertical walls in the structured resist. In a positive resist, the e-beam causes bond scission and therefore greater solubility. As for the negative resist, it is desirable to have a resist with high molecular weight and a narrow distribution.

When the electrons enter the resist they are scattered both elastically and inelastically. The inelastic scattering can lead to different processes such as secondary electrons, Auger-electrons and X-rays. The elastic scattering leads to a change in the electron direction and therefore causes broadening of the beam pro-

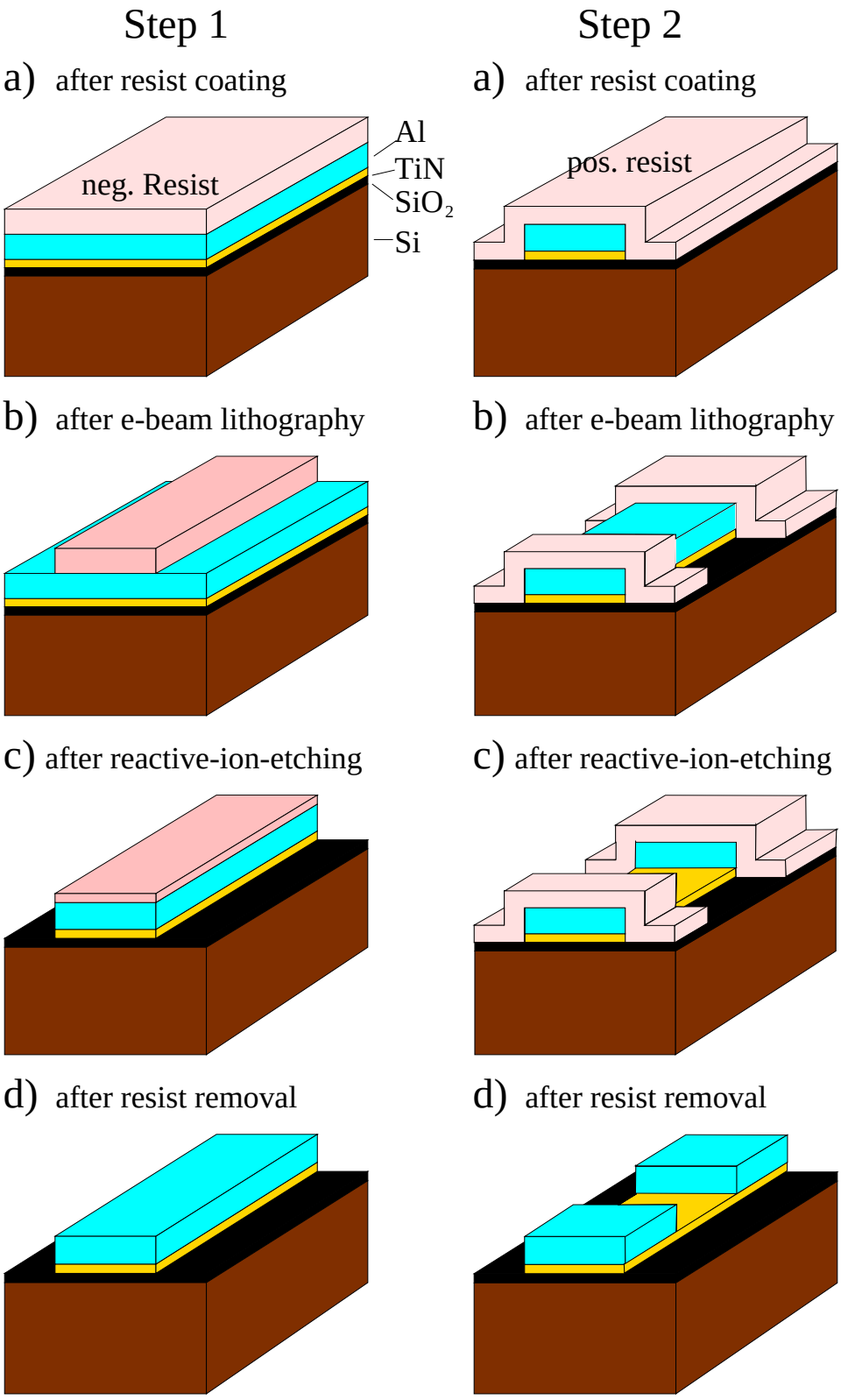

Figure A.1: Schematic illustration of the fabrication process

file. The increase in effective beam diameter due to forward scattering is given empirically by the formula $d_f[nm] = 0.9\ (R_t[nm]/V_b[kV])^{1.5}$, where R_t is the resist thickness and V_b is the beam voltage. Therefore, in order to optimize resolution one should use the highest available accelerating voltage and the thinnest possible resist. Important is also the backscattering of the electrons from the substrate to the resist, which depends on both the energy of the primary electrons and the density of the substrate. This causes the so-called proximity effect, where the dose that a pattern feature receives is affected by electrons scattering from other features nearby. The range d_b of backscattered electrons increases with increasing voltage according to $d_b \propto V^{1.75}$, but the fraction of electrons that are backscattered is roughly independent of beam energy. Therefore, the exposure due to backscattering is decreased with increasing accelerating voltage because the same amount of electrons are backscattered into a larger area. As the primary electrons slow down, much of their energy is dissipated in the form of secondary electrons with energies from 2 to 50 eV. These electrons are responsible for the actual resist exposure. Since their range in the resist is limited to a few nanometers the effective widening of the beam diameter can be neglected. But nevertheless this mechanism limits the resolution of the highest resolution electron beam systems to roughly 20nm. For the e-beam lithography a SEM conversion (Proxy-Writer) was used with a 16 bit digital-to-analog converter to drive the scan coils of the microscope.

A.1.2 Process and parameters

After a short introduction to e-beam lithography, the actual process used for fabricating the test samples is described here. To act as a mask during Al etching, the e-beam resist has to meet the following requirements:

- it should adhere to the Al surface (if possible without an adhesion promotor, because this can cause problems in removing the residual resist after the etching process)
- it should have a developer which does not attack the Al (non alkaline)
- it should have a good resistance to dry etching (Novolak based resists show

a good $SiCl_4$ dry etch resistance, but PMMA e-beam resists for example have a very poor $SiCl_4$ dry etch resistance), and

- it must be available in small amounts (a typical price is about 4000-6000DM/liter).

First process step

For the first etching process (Step 1 in Fig. A.1) a negative e-beam resist called Ar 7700/5 (consisting of Novolak, Naphthochinondiazid, and 1-Methoxy-2-propylacetat, produced by Allresist GmbH) was used which meets the previous mentioned requirements. The viscosity of the resist must be chosen appropriately to achieve the desired resist thickness at the chosen spinning velocity, because it is not possible to build-up thicker layers by spinning additional layers of resist as e.g. with PMMA resists. In the case of a Novolak based resists the upper layer dissolves the lower layer leading to the same resist thickness as before. The resist layer must be thick enough to remain during the etching process, but as thin as possible because the resolution of the resist decreases with increasing resist thickness. The necessary resist thickness therefore depends on the etching rate of the resist itself and on the etching rate and amount of the material (Aluminum and TiN) which has to be etched. For etching 800nm Al and 245nm TiN a resist thickness of one μm showed good results. This thickness can be achieved by a spinning velocity of 4000rpm for 30s. After spinning, the resist has to be annealed at 90 °C on a hot plate for 2min (Softbake).

It is desirable that the patterned resist has vertical walls because the topography of the resist is transmitted to the film after etching and it also easier to remove the resist after etching, because vertical walls are not so strongly polymerized as inclined walls. Vertical walls can be achieved by using high electron energies and a resist layer as thin as possible (for reducing the forward scattering), a small spot size and a resist with a high contrast. However, the smaller the spot size of the e-beam the lower the probe current and the higher the dwell times. Therefore, a compromise between writing time and spot size is required. A resist profile with vertical walls could be achieved with the following parameters: Accelerating voltage 40keV, spot size 5, probe current 100-140pA, aperture 100 μm, dwell time 4 μs.

After e-beam writing (exposure) the resist has to be annealed at 110 ° C for two minutes on a hot plate (Post-Exposure Bake). This step induces the crosslinks between the molecules in the exposed areas. The development of the resist (removal of the resist that is not crosslinked) is done in a mixture of Ar-300/26 (developer from Allresist) and deionised water (ratio 3:1). For increasing the etch resistance in the RIE a further annealing step after the development is carried out at 130 ° C for ten minutes. After this step the remaining resist is expected to be completely polymerized. A patterned test structure of e-beam resist after exposure and development is shown in Fig A.2. The profile of the sidewalls was examined by an FIB cross section (Fig. A.3) through a line of resist on Al/TiN/SiO_2/Si exposed and developed using this optimized process.

Second process step

Optimization of the second lithography step turned out to be complicated because for etching Al spaces in a continuous Al/TiN line an appropriate dry etch resistant positive e-beam resist has to be used which was difficult to find. For making the test samples the same sample has to be etched twice which is not a very common process and therefore required some process development. Different resists had to be tried and the advantages and disadvantages of each resist are described below for the benefit of other users.

- Ar 7400/8 from Allresist
  First a positive e-beam resist called Ar 7400/8 from Allresist GmbH was used. It is a Novoloak based resist with a high dry etch resistance against $SiCl_4$, which was used as the metal etchant in the dry etch process as will be described later. The resist is sensitive to room light and therefore yellow light equipment is required in the labs or at least a yellow filter in the light microscope for controlling the development process. Since a short exposure to room light on the order of a few seconds is not critical the resist can still be used in an conventional lab without yellow light if handeled quickly. Fig. A.4 shows a FIB cross section of the test structure covered with resist. As one can see on this picture the thickness of the resist on top of the Al-line is much less than above the silicon. As a first order approximation one can assume that after spinning the resist is everywhere planarized. So for

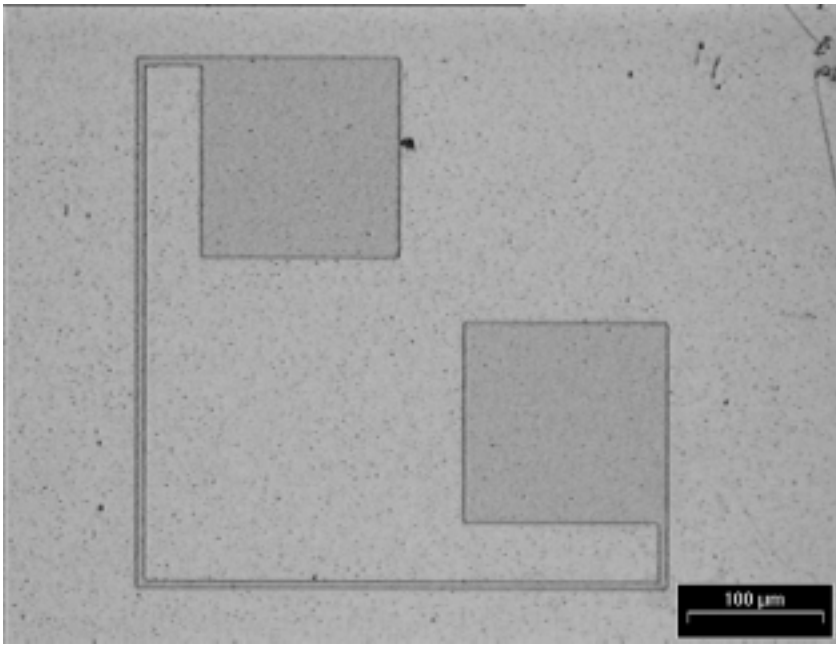

Figure A.2: Patterned test structure of e-beam resist on Al after exposure and development

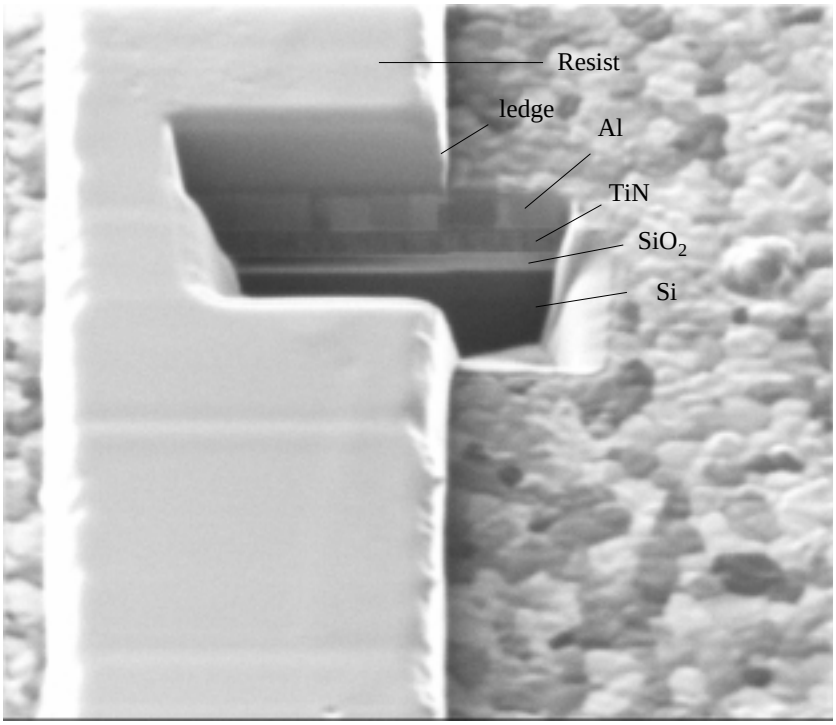

Figure A.3: FIB cross section of a patterned 5 μm wide resist line with Al/TiN/SiO_2 and Si underneath

example to get a 800nm thick resist layer on top of a one μm thick line one should choose the spinning velocity to get a 1.8 μm thick resist layer. For the later etching process it is important that the resist is removed after

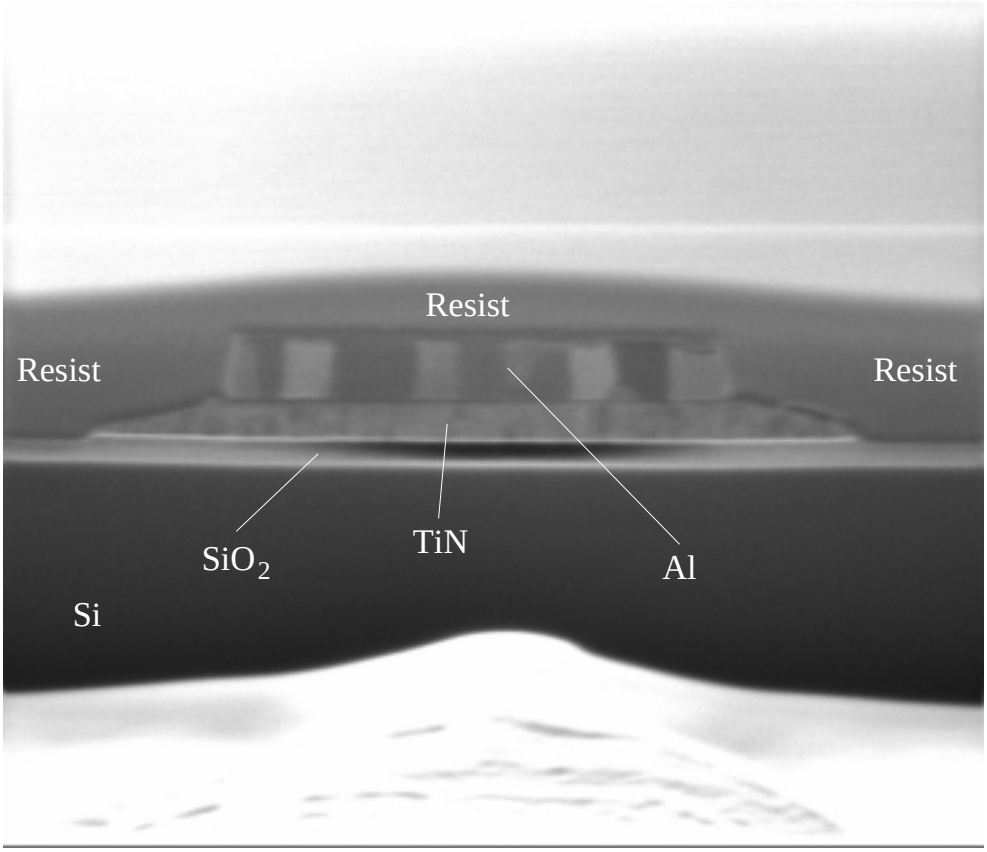

Figure A.4: FIB cross section of a continuous Al/TiN line on SiO_2/Si covered with e-beam resist

developing not only on top of the Al-line, but also at the side of the line because remaining resist at this place can lead to remaining material after etching which might act as a diffusion path for electromigration. Because of the different resist thickness the developing time for the resist on top of the line is much shorter compared to the resist on the silicon. Therefore the concentration of the developer must be as weak as possible in order to stop the developing process after having dissolved the exposed area on top of the line but at the same time continuing developing of the exposed areas on the silicon. A mixture of the developer Ar 300-26 and deionized water with

a ratio of 1:2.5 was found to meet this criterion best. The developing time is 40-50s. The e-beam exposure was done at 40keV with probe current of 160pA. Before the lithography the resist has to be prebaked for 3 minutes at 90 degrees.

The processing conditions during spin coating such as temperature and air moisture are quite important to get reproducible patterning results. Recommended values are 25 degrees room temperature and air moisture below 50 percent. Deviations of temperature and air moisture from this values can lead to adhesion problems, different resist thicknesses, different doses and developing times. Therefore, this resist is only suitable if the ambient variables can be controlled very accurately otherwise the fabrication process is not reproducible and the yield is quite low. Severe problems in controlling these ambient variables required a different resist for the patterning process.

- PMMA resist from Allresist GmbH

  As already mentioned PMMA resist is usually not suitable for dry etch processes with chlorine gases. Nevertheless, the pattering process was also tried with this resist, because it was already available at the MPI. But as expected the etch resistance is very poor and vertical walls can not be obtained. Fig. A.5 shows an etched space in the continuous Al/TiN line before removing the resist. At the edges of the two segments the resist is also etched horizontally which leads to damaged and inclined sidewalls of the Al segments as shown in Fig. A.6 after removing the resist.

- PMGI resist from MRT (Micro Resist Technology)

  The PMGI (polymethylglutarimid) resist is much easier to process than the Ar 7000 concerning ambient variables such as temperature and air moisture during spincoating and it is also not sensitive to room light. The etch resistance of the PMGI is better that the etch resistance of PMMA but not as good as the etch resistance of Ar 7000. In principle it is possible to perform the patterning process with this resist, however, extremely vertical sidewalls of the Al segments could also not be obtained with this resist. The process parameters for a one μm resist layers are: Spin coating at

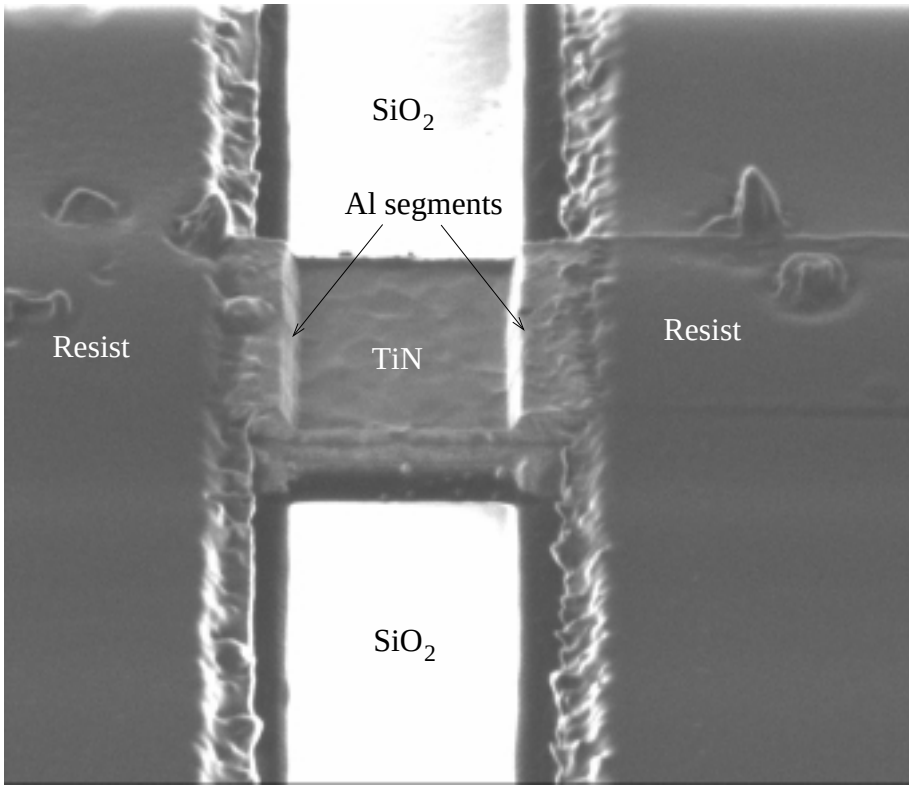

Figure A.5: Etched space in a continuous Al/TiN line before PMMA resist removal

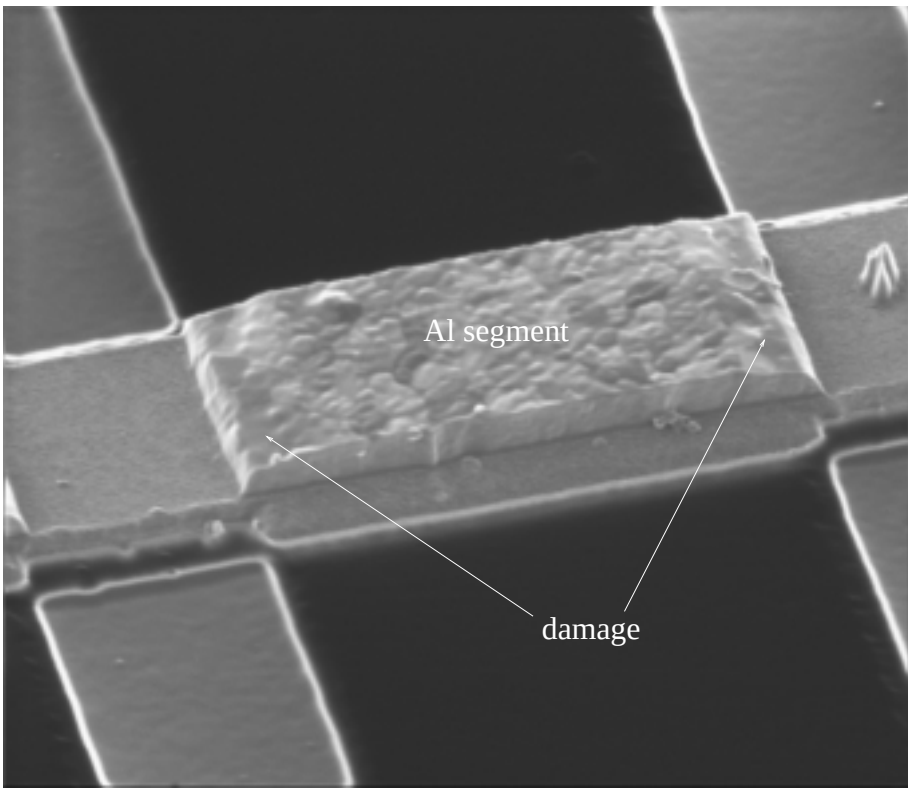

Figure A.6: Etched segment after PMMA resist removal

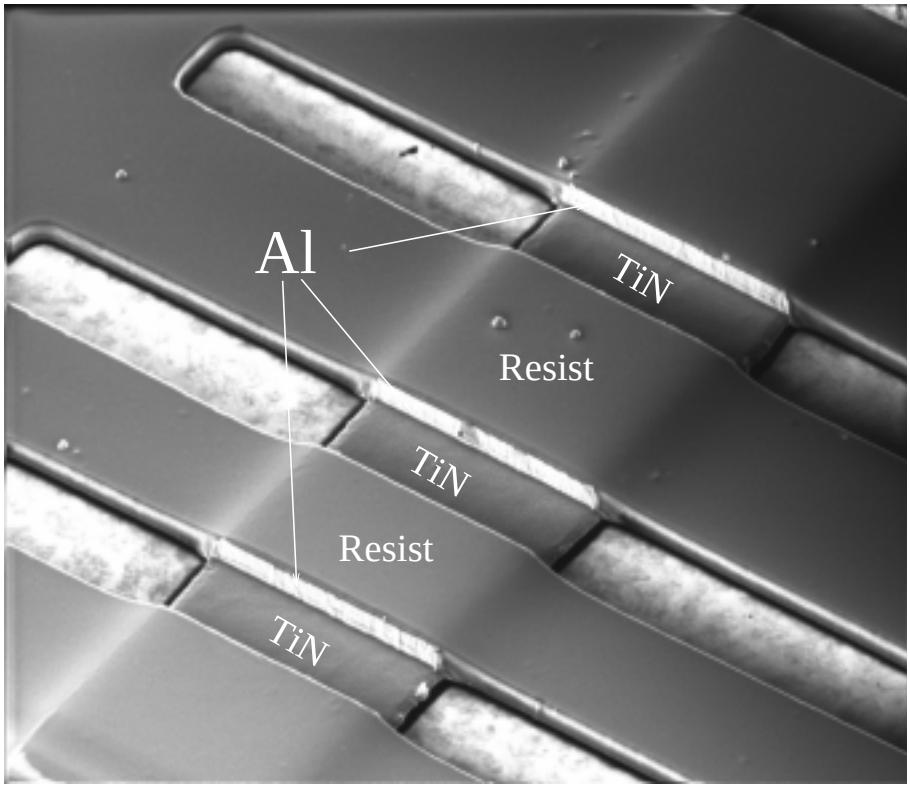

Figure A.7: Etched Al segments before UVIIHS resist removal

2000rpm for 30s, bake at 250 for 2 min, dwell time 80 μs, probe current 80 pA, developing time 1 to 1.15 min (developer: microposit MF321)

- Shipley UVIIHS 0.9

  This resist is a chemically amplified resist which is actually a positive deep UV resist but also sensitive to e-beam exposure. The contrast and etch resistance is extremely good. Fig. A.7 shows etched segments with vertical walls before removing the resist.The process parameters for a one μm resist layers are: Spin coating at 2000 rpm for 30s, softbake at 120 °C for 60s, dwell time 10 μs, probe current 50pA, post exposure bake at 130 °C for 90 s, developing time 30s, bake at 140 °C for 3min. All test samples were patterned using this resist and process parameters.

A.2 Reactive Ion Etching (RIE)

A.2.1 Theoretical Backround

In this paragraph a brief introduction to reactive ion etching (RIE) will be given, as can be found in [63] and [64] for example. Reactive ion etching involves a plasma discharge in which ionization and fragmentation of gases takes place and produces chemically active species. When the interaction of this plasma with a solid surface forms volatile products, so that the film material is removed from the surfaces where it is not masked by resist, then this technique can be used for patterning the film. The most important advantage of this process is that the etching process can be made extremely anisotropic, so that the patterns can be etched straight into the film with no lateral material removal under the mask. The interactions of the reactive plasma with the film surface consists of both physical and chemical components. The physical component refers to the bombardment of the surface by ion acceleration by an electric field. The extent of the material depletion by this process depends on the kinetic energy of the ions and therefore on the electric field. The chemical component of etching refers to the gas-surface chemistry, which contains the following steps:

- chemisorption, e.g. adsorption on the surface and forming of a chemical bond with the surface atoms
- product formation, e.g. surface atoms have to rearrange to form a product molecule
- desorption of product molecule from the surface.

In order to etch a surface every step has to occur. In situations where etching does not occur, a knowledge of which of the steps is the blocking step in the process it is often useful.

The extreme anisotropy of plasma etching is enabled due to the fact that the rate at which an active gas reacts with a surface can be increased dramatically by simultaneously irradiating the surface with energetic particles such as ions, but also with electrons or photons. The etch rate therefore is much larger than

can be accounted for by simply adding the sputtering component to the chemical component. This synergetic interaction can be caused by accelerating any or all of the three major steps absorption, product formation and product desorption.

The most important parameters that influence the actual etching process are the gas flow rate, the gas pressure and the power of the plasma, as described below.

Flow rate

During etching, feed gas is continuously introduced into the chamber and continuously pumped away. The flow rate r of the feed gas is an important process parameter which determines the residence time or the average time R a molecule spends in the chamber according to the following relation

$$R = \frac{PV}{r}, \tag{A.1}$$

where P and V the volume of the processing chamber.

Pressure

Pressure affects both the magnitude and anisotropy of the etch rate. A graph of etch rate versus pressure produces a bell shaped curve with a maximum etch rate at an intermediate pressure. The decrease in etch rate at lower pressures is due to a decreased supply of reactive gases. The decrease in the etch rate at high pressures is a result of having a high concentration of reactive species which recombine into non-reactive gas molecules. The pressure also affects the degree of anisotropy. The higher the pressure the more collisions occur causing the ions to deviate from the normal path to the target surface. The ions then strike the sidewalls causing a decrease in anisotropy.

Power

Increasing the rf power in the plasma increases both bias voltage and concentration of reactive neutrals and ions. The etch rate therefore increases almost linearly with increasing power.

A.2.2 Process and Parameters

Al and TiN can be patterned by reactive ion etching with $SiCl_4$. This process was first investigated by Sato [65] and was found to have many advantages compared

to etching with other gases such as CCl_4. The advantages are: high selectivity that means strongly different etch rates for Al, Resist, TiN and SiO_2, less contamination by carbon and chlorine, longer lifetime of the rotary pumps.

The etch rates of Al and its native oxide as a function of pressure and power density found by Sato are shown in Fig. A.8. The lateral etch rate was determined

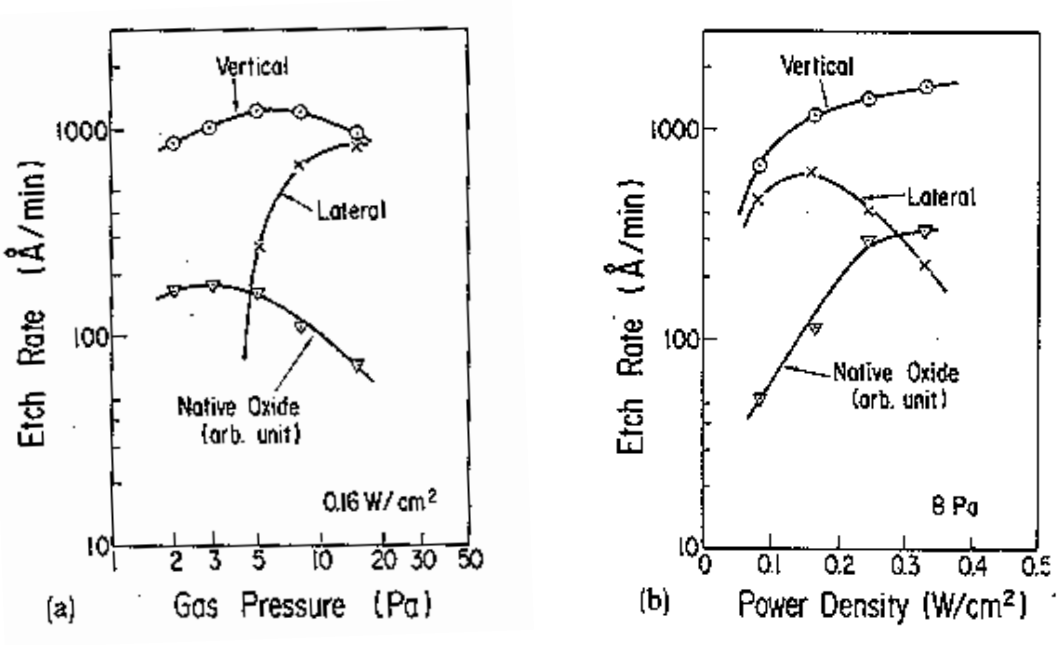

Figure A.8: Vertical and lateral etch rates of aluminum, as well as etch rates of native oxide, as a function of (a) gas pressure and (b) power density (taken from [65])

by measuring the amount of lateral material removal under a Si_3N_4 mask. As shown in Fig. A.8a the anisotropy can be controlled by the gas pressure. At 15 Pa the vertical and horizontal etch rate are approximately the same and therefore the etch process is isotropic whereas at lower pressures (< 5 Pa) the etch process is completely anisotropic. In Fig. A.8b the etch rate of the native oxide is shown as a function of power density. The steep increase of etch rate with higher power density is due to physical sputtering of the native oxide, which is hard to remove with chlorine chemistry only. The stable native oxide which is always present on air exposed aluminum is etched at a very low etch rate, because the heat of formation for the etch product $AlCl_3$ (-140kcal/mole) is much less than for Al_2O_3

(-400kcal/mole). Therefore, small deviations in oxide thickness from sample to sample or even on the same sample can lead to an irregular incubation period prior to the onset of aluminum etching, which makes it difficult to predict the endpoint of etching. A further consequence is that the etching surface can be extremely rough because of slight nonuniformities in the oxide thickness. Approaches to solve this problem are either a higher rf power for the initial portion of the etch process, because increasing rf power causes higher energetic ion bombardment and therefore enhances the physical sputter process which is the dominant etch process for Al_2O_3 or the use of other gases which chemically reduce the Al_2O_3 e.g. BCl_3 or CCl_4.

For the system available at the MPI (Plasmalab 80 Plus from Oxford Instruments) the following etching parameters were found to lead to good results: Base pressure 10^{-5}mbar, working pressure 40mTorr ($\approx$ 5.3 Pa), power 150 Watt, flow rate 20sccm SiCl4. The corresponding etch rates are approximately 100nm Al/min, 20nm TiN/min, 35nm resist (Ar 7700/5)/min.

The patterning process before and after RIE is illustrated by FIB cross sections in Fig. A.9 and Fig. A.10, respectively, which corresponds to Step 1b and 1c in Fig. A.1. The residual resist on top of the Al line in Fig. A.10 is clearly visible and has to be removed in a next step. When the etched Al pattern is removed from the chamber and exposed to air it starts immediately to corrode, because chlorinated residues on both Al and resist react with the water vapor and form HCl which attacks the aluminum. In Fig. A.11 a SEM picture of a corroded Al/TiN line after etching is shown. The "bubbles" at the edge of the line are typical for corrosion after RIE. To avoid this problem the patterns have to be rinsed in deionised water immediately after etching. The remaining resist should be removed very quickly after etching because it can still act as a chlorine source and cause corrosion. A complete removal of the resist can be achieved in ACT at 75 °C for a few minutes, as shown in Fig. A.12 (an oxygen plasma after the etching process does often not lead to complete removal). It is important that the resist is removed completely from the aluminum because the subsequent step 2 (making the intersections in the continuous Al/TiN line) works only well when there is no resist remaining. Little remainings of resist lead to very different etching rates in the second step so that some of the intersections are overetched whereas others

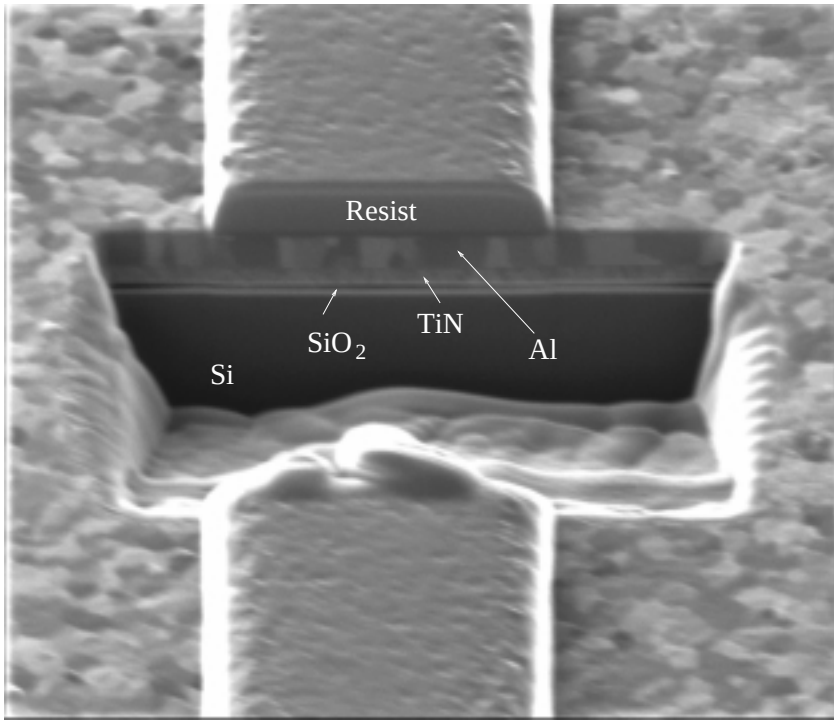

Figure A.9: FIB cross section of patterned 5 μm wide resist line on Al/TiN/SiO_2/Si before RIE.

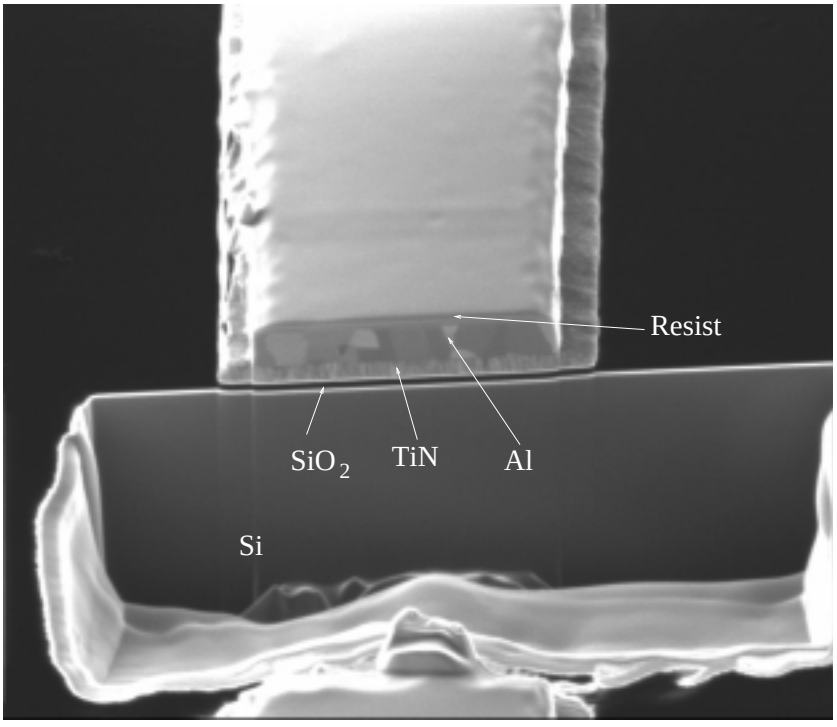

Figure A.10: FIB cross section of an etched 5 μm wide Al/TiN line on SiO_2/Si with resist residual on top

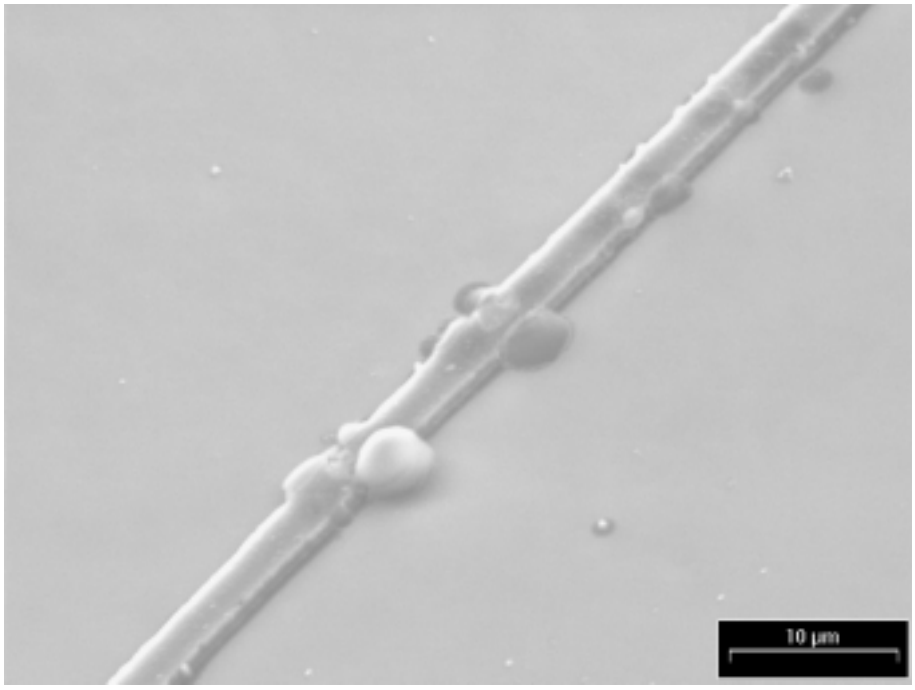

Figure A.11: SEM picture showing typical morphology of a corroded Al/TiN line after RIE. "Bubbles" at the edges of the line are often observed

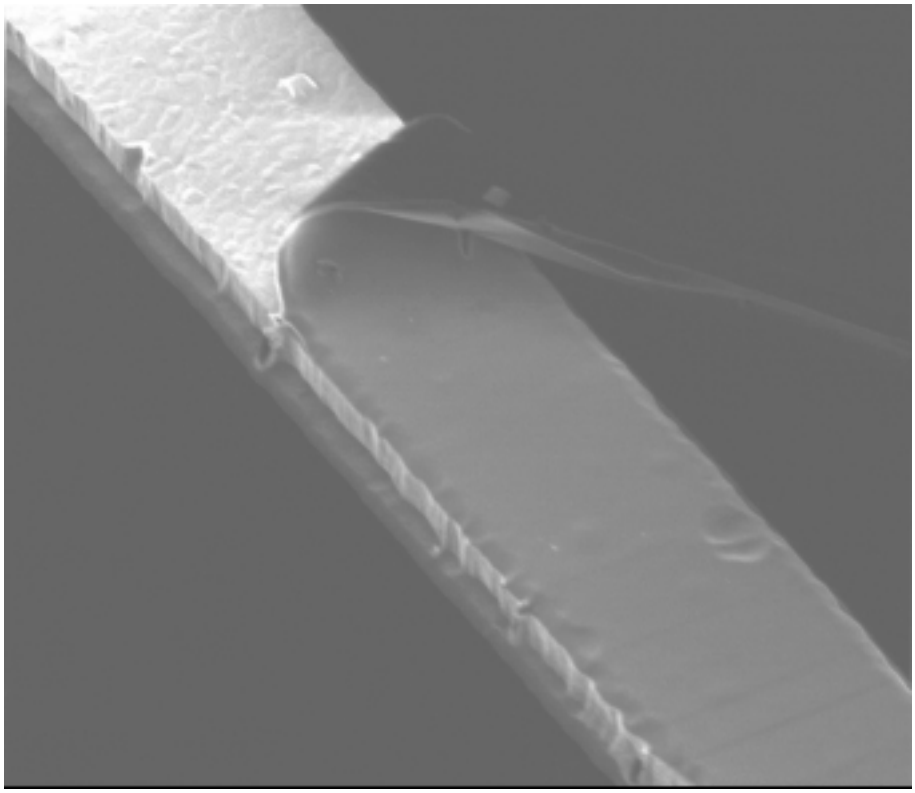

Figure A.12: FIB picture illustrating the process of resist removal with ACT. Below the residual resist the bare Al surface is clearly visible

are not completely etched. When an adhesion promoter (Diphenylsilandiol) was used in the first step, a complete removal could neither be achieved by ACT nor in an oxgene plasma. The test sample after the final process step of residual resist removal in ACT is shown in Fig. A.13 and Fig. A.14.

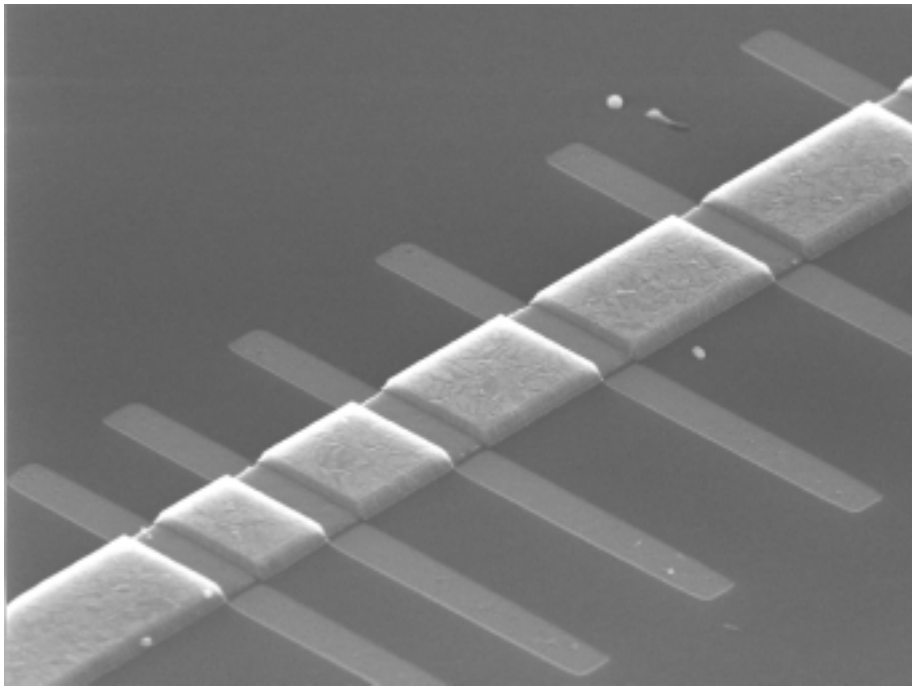

Figure A.13: SEM picture of a typical test samples (10 μm wide) after the final process step

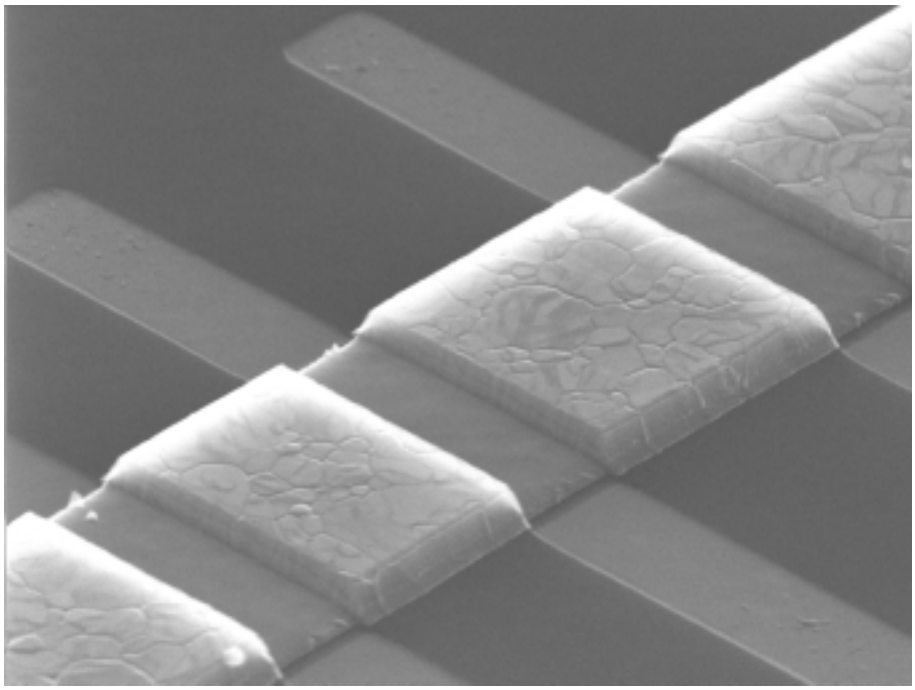

Figure A.14: Same test sample as above at a higher magnification. The grain structure of Al and vertical sidewalls of the segments are clearly visible.

Appendix B

Calculation of Critical Products

film thickness [μm]	**width** [μm]	**current density** [MA/cm^2]	**crit. length** [μm]	**crit. product** [A/cm]
0.1	9.32	0.94	17.38	1634
0.1	9.44	0.93	16.97	1577
0.1	8.82	0.99	14.43	1428
0.1	8.76	1.00	16.58	1658
0.1	8.56	1.02	14.57	1486
0.1	8.75	1.00	14.06	1406
0.2	9.1	1.03	13.88	1430
0.2	9.2	1.02	13.62	1383
0.2	8.4	1.11	12.2	1354
0.2	8.35	1.12	12.5	1400
0.2	8.6	1.09	12.45	1357
0.4	8.7	1.11	12.25	1360
0.4	8.8	1.01	9.7	1057
0.4	8.8	1.09	11.68	1273
0.4	8.6	1.12	11.61	1300
0.4	8.66	1.11	10.72	1190
0.4	8.6	1.12	10.8	1208
0.4	8.76	1.1	12.73	1397
0.4	8.6	1.12	12.88	1440

film thickness [μm]	**width** [μm]	**current density** [MA/cm^2]	**crit. length** [μm]	**crit. product** [A/cm]
0.6	9.32	1.05	9.75	1024
0.6	9.24	1.06	11.5	1219
0.6	8.7	1.13	11.03	1246
0.6	8.7	1.13	11.5	1299
0.6	8.9	1.1	11.03	1212
0.8	8.67	1.15	7.06	805
0.8	8.65	1.16	6.75	783
0.8	7.6	1.29	8.8	1135
0.8	8.04	1.22	9.35	1140
0.8	8.0	1.23	8.93	1094

Appendix C

Finite Element Source Code (ANSYS 5.4)

C.1 Joule heating

/prep7

! Geometrical dimensions; l=length, b=width, h=thickness ! Sio2=thickness of Sio2 , Tin= thickness of TiN

l=3.5
b=4.3
h=0.8
sio2=0.2
tin=0.245

bsi=2000 ! width of substrate
hsi=670 ! thickness of substrates

!Element type

et,1,solid69

```
! Material properties

! Aluminium

mp,ex,1,72e-3 ! Youngs modulus
mp,nuxy,1,0.36 ! Poisson‘s ratio
mp,alpx,1,24e-6 ! expansion coefficient
mp,rsvx,1,3.4e4 ! resistivity
mp,c,1,0.9e9 ! heat capacity
mp,dens,1,2.7e-15 ! density
mp,kxx,1,237 ! thermal conductivity


! TiN

mp,ex,2,110e-3
mp,nuxy,2,0.34
mp,alpx,2,8.8e-6
mp,rsvx,2,50e4
! mp,perx,2,1
mp,dens,2,4.5e-15
mp,c,2,0.5e9
mp,kxx,2,200


! SiO2 mp,ex,3,60e-3
mp,nuxy,3,0.18
mp,alpx,3,0.5e-6
mp,c,3,0.7e9
mp,dens,3,2.3e-15
mp,kxx,3,1.3
mp,rsvx,3,150e10


! Si mp,ex,4,120e-3
mp,nuxy,4,0.2
mp,alpx,4,3e-6
mp,c,4,0.7e9
```

```
mp,kxx,4,148
mp,dens,4,2.33e-15
mp,rsvx,4,10000e4

! bottom SiO2 layer mp,ex,5,60e-3
mp,nuxy,5,0.18
mp,alpx,5,0.5e-6
mp,c,5,0.7e9
mp,dens,5,2.3e-15
mp,kxx,5,0.68e-3
mp,rsvx,5,10000e4

! Geometry

! Silicon

k,1,0,0,0
k,2,l,0,0
k,3,2*l,0,0
k,4,l+1.5,0,0
k,5,l+1.5,0,b
k,6,l+1.5,0,2*b
k,7,l+1.5,0,bsi
k,8,2*l,0,bsi
k,9,l,0,bsi
k,10,0,0,bsi
k,11,0,0,2*b
k,12,0,0,b
kgen,3,1,12,1,0,hsi,0,12

! Silicon oxide

kgen,2,25,36,1,0,sio2,0,12
```

```
! TiN

k,49,l,2*hsi+sio2,b
k,50,2*l,2*hsi+sio2,b
k,51,0,2*hsi+sio2+tin,0
k,52,l,2*hsi+sio2+tin,0
k,53,2*l,2*hsi+sio2+tin,0
k,54,l+1.5,2*hsi+sio2+tin,0
k,55,l+1.5,2*hsi+sio2+tin,b
k,56,2*l,2*hsi+sio2+tin,b
k,57,l,2*hsi+sio2+tin,b
k,58,0,2*hsi+sio2+tin,b

! Al

k,59,0,2*hsi+sio2+tin+h,0
k,60,l,2*hsi+sio2+tin+h,0
k,61,l,2*hsi+sio2+tin+h,b
k,62,0,2*hsi+sio2+tin+h,b

! additional Keypoints
k,63,l,2*hsi,b
k,64,l,hsi,b
k,65,l,0,b

! bottom SiO

k,70,0,-sio2,0
k,71,l,-sio2,0
k,72,l+1.5,-sio2,0
k,73,0,-sio2,b
k,74,l,-sio2,b
k,75,l+1.5,-sio2,b
k,76,0,-sio2,bsi
k,77,l,-sio2,bsi
```

```
k,78,l+1.5,-sio2,bsi

! Volumes
/pnum,volu,1

! 1. Quadrant

! Al v,59,60,61,62,51,52,57,58

! TiN v,51,52,57,58,37,38,49,48

! SiO2
v,37,38,49,48,25,26,63,36
! Si
v, 25,26,63,36,13,14,64,24 v,13,14,64,24,1,2,65,12
! 2. Quadrant
! TiN
v,52,38,49,57,54,40,41,55
! Sio2
v,38,26,63,49,40,28,29,41
! Si
v,26,14,64,63,28,16,17,29
v,14,2,65,64,16,4,5,17

! 3. Quadrant
! sio2 and Si
v,49,41,29,63,45,43,31,33
! Si below
v,63,29,17,64,33,31,19,21
v,64,17,5,65,21,19,7,9
```

```
! 4. Quadrant

! Sio2 and Si
v,48,49,63,36,46,45,33,34
! Si below
v,36,63,64,24,34,33,21,22
v,24,64,65,12,22,21,9,10


! bottom Sio

v,1,2,65,12,70,71,74,73
v,9,10,76,77,65,12,73,74
v,77,74,75,78,9,65,5,7
v,2,65,74,71,4,5,75,72


alls
/pnum,line,1
/pnum,kp,1
/pnum,volu,1
/psymb,ldir,1


! Meshing

lsel,s,,,3
lsel,a,,,10
lsel,a,,,6
lsel,a,,,22
lsel,a,,,14
lsel,a,,,26
lsel,a,,,18
lsel,a,,,91
lsel,a,,,94
lsel,a,,,42
```

```
lsel,a,,,34
lsel,a,,,30
lsel,a,,,38
lsel,a,,,86
lsel,a,,,88
lsel,a,,,98
lsel,a,,,102
lesize,all,,,13,10

lsel,s,,,1
lsel,a,,,106
lesize,all,,,13,0.1

lsel,s,,,8
lsel,a,,,2
lsel,a,,,16
lsel,a,,,24
lsel,a,,,32
lsel,a,,,40
lsel,a,,,48
lsel,a,,,55
lsel,a,,,60
lsel,a,,,65
lsel,a,,,100
lesize,all,,,7,0.5

lsel,s,,,4
lsel,a,,,12
lsel,a,,,20
lsel,a,,,28
lsel,a,,,36
lsel,a,,,44
lsel,a,,,52
```

```
lsel,a,,,104
lsel,a,,,115
lesize,all,,,7,2

lsel,s,,,11
lsel,a,,,7
lsel,a,,,5
lsel,a,,,9

lesize,all,,,10

lsel,s,,,51
lsel,a,,,49
lsel,a,,,47
lsel,a,,,56
lsel,a,,,61
lsel,a,,,66
lsel,a,,,69
lsel,a,,,73
lsel,a,,,78
lsel,a,,,83
lsel,a,,,112
lsel,a,,,116
lesize,all,,,8,0.25

lsel,s,,,45
lsel,a,,,53
lsel,a,,,58
lsel,a,,,63
lsel,a,,,110

lesize,all,,,8,4
```

```
lsel,s,,,59
lsel,a,,,62
lsel,a,,,35
lsel,a,,,80
lsel,a,,,93
lsel,a,,,31
lsel,a,,,33
lsel,a,,,80
lesize,all,,,16,0.001

lsel,s,,,76
lsel,a,,,29
lesize,all,,,16,1000

lsel,s,,,96
lsel,a,,,85
lsel,a,,,43
lsel,a,,,39
lsel,a,,,41
lsel,a,,,67
lsel,a,,,64
lesize,all,,,3

lsel,s,,,81
lsel,a,,,37
lesize,all,,,3

lsel,s,,,70
lsel,a,,,74
lsel,a,,,79
lsel,a,,,84
```

```
lsel,a,,,87
lsel,a,,,89
lsel,a,,,95
lsel,a,,,92
lsel,a,,,72
lsel,a,,,77
lsel,a,,,82
lesize,all,,,25,0.0005

lsel,s,,,68
lsel,a,,,108
lsel,a,,,109
lsel,a,,,111
lesize,all,,,25,2000

alls
/pnum,line,1
/pnum,kp,1
/pnum,volu,1
/psymb,ldir,1

! Meshing
/pnum,mat,1
/number,1

mat,4
vmesh,14,15
vmesh,11,12
vmesh,4,5
vmesh,8,9

mat,3
```

```
vmesh,3
vmesh,7
vmesh,10
vmesh,13

mat,2
vmesh,2
vmesh,6

mat,1
vmesh,1

mat,5
vmesh,16
vmesh,17
vmesh,18
vmesh,19

save,db

! boundary conditions

! electric

nsel,s,loc,x,0
nsel,r,loc,y,2*hsi+sio2,2*hsi+sio2+tin+h
nsel,r,loc,z,0,b
d,all,volt,0

nsel,s,loc,x,l+1.5
nsel,r,loc,y,2*hsi+sio2,2*hsi+sio2+tin
```

```
nsel,r,loc,z,0,b
d,all,volt,2e6
cp,1,volt,all

nsel,s,loc,x,l+1.5
nsel,r,loc,y,2*hsi+sio2+tin,2*hsi+sio2+tin+0.000001
nsel,r,loc,z,0

f,all,amps,0.040

! thermal

nsel,s,loc,y,-sio2
d,all,temp,225

alls

! Solution
/solu

neqit,50
cnvtol,temp,,0.01
outpr,all,all
outres,all,all
solve

/post1
esel,s,mat,,1
```

C.2 Electromigration-induced stresses

```
/prep7

! Geometrical dimensions in μm; b=width, h=thickness

bk=0.0025 ! half of grain boundary width
bal=in*0.1*0.5 ! half of grain-width
h=0.4 ! thickness of grain
alo=0.0018 ! thickness of native oxide
tins=0.01
tin=0.245 ! thickness of TiN
dsi=0.4 ! thickness of Si


!Element type
et,1,plane82,,,0
et,2,plane2,,,0,,1


! Material Properties

! Aluminium

mp,ex,1,72e9 ! Youngs modulus
tb,bkin,1 ! Nonlinear material properties
tbdata,1,10e9,0 ! Yields stress 1GPa, no work hardening
mp,nuxy,1,0.36 ! Poisson‘s ratio


! TiN

mp,ex,2,200e9 ! Youngs modulus
mp,nuxy,2,0.34 ! Poisson‘s ratio


! Al2O3

mp,ex,3,470e9 ! Youngs modulus
mp,nuxy,3,0.23 ! Poisson‘s ratio
```

```
! Si

mp,ex,4,120e9 ! Youngs modulus
mp,nuxy,4,0.2 ! Poisson‘s ratio


! Grain boundary (same as Al)

mp,ex,1,72e9 ! Youngs modulus
tb,bkin,1 ! Nonlinear material properties
tbdata,1,10e9,0 ! Yields stress 1GPa, no work hardening
mp,nuxy,1,0.36 ! Poisson‘s ratio


! Geometry of grain

! Keypoints

k,1,0,0
k,2,0,dsi
k,3,0,dsi+tin-tins
k,4,0,dsi+tin
k,5,0,dsi+tin+tins
k,6,0,dsi+tin+h-alo
k,7,0,dsi+tin+h
k,8,0,dsi+tin+h+alo


k,9,bk,0
k,10,bk,dsi
k,11,bk,dsi+tin-tins
k,12,bk,dsi+tin
k,13,bk,dsi+tin+tins
k,14,bk,dsi+tin+h-alo
k,15,bk,dsi+tin+h
k,16,bk,dsi+tin+h+alo
```

```
k,17,bk+bal,0
k,18,bk+bal,dsi
k,19,bk+bal,dsi+tin-tins
k,20,bk+bal,dsi+tin
k,21,bk+bal,dsi+tin+tins
k,22,bk+bal,dsi+tin+h-alo
k,23,bk+bal,dsi+tin+h
k,24,bk+bal,dsi+tin+h+alo

! Areas

A,1,9,10,2
A,10,2,3,11
A,3,11,12,4
A,12,4,5,13
A,5,13,14,6
A,14,6,7,15
A,7,15,16,8

A,17,9,10,18
A,10,18,19,11
A,19,11,12,20
A,12,20,21,13
A,21,13,14,22
A,14,22,23,15
A,23,15,16,24

! Meshing

kscon,7,0.0001,1,8
kscon,4,0.0001,1,8
ez=15
```

```
lesize,9,,,ez
lesize,11,,,ez
lesize,12,,,ez
lesize,13,,,ez
lesize,6,,,ez
lesize,8,,,ez
lesize,10,,,ez


lesize,15,,,ez
lesize,17,,,ez
lesize,18,,,ez
lesize,19,,,ez
lesize,20,,,ez
lesize,21,,,ez
lesize,22,,,ez

! Element divisions in Al horizontal

lsel,s,,,24
lsel,a,,,28
lsel,a,,,32
lsel,a,,,36
lesize,all,,,28,20*in


lsel,s,,,23
lsel,a,,,27
lsel,a,,,31
lsel,a,,,35
lesize,all,,,28,0.05/in

! Element division in Al vertical

lsel,s,,,14
lesize,all,,,150*h,-80
```

```
lsel,s,,,16
lsel,a,,,33
lesize,all,,,150*h,-80

! Element divisions in TiN vertical

lsel,s,,,5
lsel,a,,,26
lesize,all,,,20,0.01
lsel,s,,,7
lesize,all,,,20,100

! Si vertical

lsel,s,,,2
lesize,all,,,10
lsel,s,,,4
lsel,a,,,25
lesize,all,,,10

type,2
mat,3
amesh,7
type,1
amap,14,15,16,23,24

type,2
mat,5
amesh,6
type,1
amap,5,6,14,5,13

type,1
```

```
mat,1
amap,13,22,23,14,15
amap,12,21,22,14,13

type,2
mat,5
amesh,4
mat,2
amesh,3
type,1
mat,1
amap,11,13,12,20,21
mat,2
amap,10,12,11,20,19
amap,2,3,11,10,2
amap,9,11,10,18,19

mat,4
amap,1,2,10,9,1
amap,8,10,9,17,18

/pnum,mat,1
/num,1

alls

/solu
/output

! Boundary conditions

dl,22,7,symm
```

```
dl,10,3,symm
dl,5,2,symm
dl,4,1,symm
sfl,17,pres,200e6
sfl,16,pres,200e6
sfl,11,pres,200e6


nsel,s,loc,x,bk+bal
d,all,ux


nsel,s,loc,y,0
d,all,uy
tref,0
alls
solve


/post1
/dscale,1,1


! Resolved shear stresses

/prep7
k,100,0.05,-0.14 !angle of 70.53 to neg. y-axis
k,101,0.05,0.14
cskp,11,0,1,100,101 !coord. system defined by kp: number, cartesian, origin, xaxis
,plane


/post1
! csys,11 ! active coordinate system
rsys,11 ! result coordinate system


! pfad
```

```
esel,s,mat,,1
esel,a,mat,,5
path,gleitebene,2,,50
ppath,1,,0,dsi+tin+0.1
ppath,2,,0.035,dsi+tin
pdef,shear,s,xy,noav
paget,shear2,table


*cfopen,gleitebene3

*do,i,1,51


inter1=shear2(i,4) ! coordinate
inter2=shear2(i,5) ! stress


*cfwrite,*enddo


! Stress gradients in the grain


yu=bal/5


*do,o,1,5


path,ppath,1,,yu*o,dsi+tin+h
ppath,2,,yu*o,dsi+tin
pdef,sx2,s,x,noav
paget,daten

*enddo


*cfopen,400ohne,dat,/home/straub/latex/diss
```

```
*do,i,1,21
var=daten1(i,4)
var1=daten1(i,5)
var2=daten2(i,5)
var3=daten3(i,5)
var4=daten4(i,5)
var5=daten5(i,5)

*cfwrite,*enddo

! average stress

esel,s,mat,,1
etable,sx,s,x ! stress component x
etable,a,volu
smult,fges,sx,a
ssum
get,ages,ssum,0,item,a
get,gkraft,ssum,0,item,fges
sxmittel=gkraft/ages

! stress gradient along the interface

esel,s,mat,,1
esel,a,mat,,5
path,interface,2,,50
ppath,1,,0,dsi+tin
ppath,2,,bk+bal,dsi+tin
pdef,sy2,s,y,noav
paget,inter,table

*cfopen,inter
```

```
*do,i,1,51


inter1=inter(i,4) ! coordinate
inter2=inter(i,5) ! stress
cfwrite,*enddo
```